

Gravitational wave detection with refined light

The implementation of an output mode cleaner at GEO 600

Von der Fakultät für Mathematik und Physik der
Gottfried Wilhelm Leibniz Universität Hannover
zur Erlangung des Grades

Doktor der Naturwissenschaften
Dr. rer. nat

genehmigte Dissertation
von

Dipl.-Phys. Mirko Prijatelj

geboren am 03. Dezember 1980 in Hannover

2012

Referent:	Prof. Dr. Karsten Danzmann
Koreferent:	Prof. Dr. Roman Schnabel
Tag der Promotion:	14.11.2012

Abstract

In 1916 Albert Einstein developed the general theory of relativity. A prediction of general relativity that has not yet been directly confirmed is the existence of gravitational waves. The German-British GEO 600 gravitational wave detector near Hannover, Germany is part of an international network of detectors created in an effort to make the first direct observation of gravitational waves. The centerpiece of GEO 600 is a Michelson interferometer consisting of two 600 m long arms which are folded once to give an effective length of 1200 m. In 2009 the GEO-HF upgrade program to GEO 600 started with the goal of improving GEO 600's sensitivity mainly at frequencies above 600 Hz.

An important part of the GEO-HF upgrade, and the core of this thesis, is the implementation of an output mode cleaner. It removes spurious components from the output beam of GEO 600's interferometer, thereby reducing the shot noise and improving the detector's sensitivity to gravitational waves at high frequencies. Apart from this immediate benefit the output mode cleaner also enables the implementation of squeezed vacuum injection. The presence of the spurious beam components would otherwise diminish the effectiveness of the reduction of shot noise by squeezed vacuum injection.

Chapter 1 introduces the concept of gravitational waves and presents the state of the international gravitational wave detection effort. Chapter 2 details the individual components of the GEO-HF program and its current state. The general working principle and properties of optical resonators such as the output mode cleaner are introduced in chapter 3. Chapter 4 presents the signal-recycling advanced interferometer technique. The same chapter also discusses the effects of changes in the signal-recycling configuration on the content of the interferometer's output beam components and on the shot noise limited sensitivity of GEO 600. Chapter 5 details the design of the output mode cleaner, the associated infrastructure, and its control systems. The effects of changes in the signal-recycling on the output mode cleaner are also detailed here. Chapter 6 describes the experiences we made operating GEO 600 with the output mode cleaner and present a use of GEO 600 for measurements not related to the detection of gravitational waves.

Keywords: Gravitational wave detector, Output mode cleaner, DC readout

Zusammenfassung

Albert Einstein entwickelte 1916 die Allgemeine Relativitätstheorie. Eine Vorhersage der Allgemeinen Relativitätstheorie, die noch nicht experimentell bestätigt werden konnte, ist die Existenz von Gravitationswellen. Der deutsch-britische Gravitationswellendetektor GEO 600 bei Hannover ist Teil eines internationalen Netzwerks von Gravitationswellendetektoren, welches geschaffen wurde um die erste direkte Beobachtung von Gravitationswellen zu ermöglichen. Das Kernstück von GEO 600 ist ein Michelson-Interferometer, bestehend aus zwei 600 m langen Armen, die einmal gefaltet sind um eine effektive Länge von 1200 m zu erreichen. Das GEO-HF Programm zur Verbesserung der Empfindlichkeit von GEO 600 bei Frequenzen über 600 Hz begann im Jahr 2009.

Ein wichtiger Aspekt des GEO-HF Programms, und Hauptthema dieser Arbeit, ist die Implementation eines Modenfilters (auf englisch *output mode cleaner* (OMC)) am Ausgang des Interferometers. Dieser entfernt unerwünschte Komponenten aus dem Ausgangsstrahl des Interferometers und reduziert dadurch das Schrotrauschen und verbessert so die Empfindlichkeit des Detektors für Gravitationswellen. Darüber hinaus ermöglicht die Entfernung unerwünschter Strahlkomponenten die effektive Nutzung eines Quetschlichtlasers zur weiteren Reduktion des Schrotrauschens.

In Kapitel 1 wird das Konzept der Gravitationswellen eingeführt und der aktuellen Stand der internationalen Bemühungen diese zu detektieren präsentiert. Kapitel 2 beschreibt die einzelnen Komponenten des GEO-HF Programms, und stellt den aktuellen Stand des Programms dar. In Kapitel 3 werden die grundlegenden Prinzipien und Eigenschaften von optischen Resonatoren, wie dem Modenfilter, erläutert. In Kapitel 4 wird eine fortgeschrittene Technik der Interferometrie, bekannt als Signal-recycling, beschrieben. Weiterhin werden die Effekte die Änderungen am Signal-recycling auf die schrotrauschbegrenzte Empfindlichkeit von GEO 600 und den Ausgangsstrahl des Interferometers haben diskutiert. Kapitel 5 beschreibt das Design des Modenfilters, der zugehörigen Infrastruktur und die Kontrollsysteme des Modenfilters. Weiterhin werden die Effekte die Änderungen der Signal-recycling Konfiguration auf das Modenfilter System haben beschrieben. In Kapitel 6 werden die Erfahrungen dargestellt, die wir mit dem Modenfilter System sammeln konnten. Darüber hinaus wird anhand eines Beispiels aufgezeigt, wie man GEO 600 für Messungen verwenden kann, welche keinen Bezug zur Detektion von Gravitationswellen haben.

Stichworte Gravitationswellendetektor, Output mode cleaner, DC readout

Contents

Abstract	i
Zusammenfassung	iii
List of Figures	vii
List of Tables	xi
Glossary	xiii
1 Introduction	1
2 The GEO-HF upgrade program of GEO 600	13
3 Optical resonators	25
3.1 A light beam as a superposition of optical modes	25
3.2 The M^2 beam quality parameter	27
3.3 Functional principle of an optical resonator	28
3.4 Parameters of optical resonators	28
3.4.1 Free spectral range	28
3.4.2 Finesse	29
3.4.3 G factor	29
3.4.4 Impedance matching	30
3.5 Mode-conversion when coupling into an optical resonator	33
4 GEO 600 signal-recycling configurations	35
4.1 Shot noise limited sensitivities for different signal-recycling configurations	35
4.2 Dependence of higher order optical mode generation on the signal-recycling configuration	36
4.2.1 Mode-healing due to signal-recycling	41
5 The output mode cleaner	45
5.1 Design of the output mode cleaner	47
5.2 Building the output mode cleaner	48
5.3 Control system requirements and schemes	51
5.3.1 Longitudinal control requirements	51

5.3.2	Longitudinal control scheme	52
5.3.3	Alignment control requirements	54
5.3.4	Alignment control scheme	56
5.4	Details of the implementation of the output mode cleaner	60
5.4.1	Vibration isolation	60
5.4.2	Optical configuration in the output mode cleaner's vacuum tank	61
5.4.3	Mode-matching	62
5.4.4	Control system infrastructure	65
5.4.5	Longitudinal control implementation	68
5.4.6	Alignment control implementation	69
5.4.7	BDO mirror suspension upgrade	75
5.5	Effect of signal-recycling configuration change on the output mode cleaner	82
5.5.1	Beacon alignment control	86
5.5.2	Optimal beacon alignment control	89
6	Experiences with the output mode cleaner	97
6.1	Noise projections	97
6.2	Imperfections of the output mode cleaner optics	103
6.3	Measured upper limit for the internal noise of a piezo-electric actuator	104
7	Summary and Outlook	107
A	Shapes of the mechanical modes of the output mode cleaner	109
B	Performance evaluation of the Control and Data System	115
C	The control model of the output mode cleaner in the Control and Data System	127
D	Output mode cleaner lock acquisition logic	131
E	The LabView component of the output mode cleaner's control system	139
	Acknowledgments	143
	Bibliography	145
	Curriculum vitae	157

List of Figures

1.1	Observation of the orbital decay of PSR B1913+1916.	3
1.2	Sensitivity comparison of the AURIGA resonant bar detector to early versions of the LIGO interferometric detectors.	4
1.3	Example pictures of two resonant mass GW detectors.	4
1.4	Effect of GWs on a Michelson interferometer.	5
1.5	Comparison of GW detector sensitivities.	7
1.6	Simplified GEO 600 layout.	10
1.7	Overview of the measurement bands of different GW detection efforts. . .	12
1.8	Comparison of the sensitivities of the NGO project and the LIGO detectors.	12
2.1	Planned evolution of GEO 600’s sensitivity over the course of the GEO-HF upgrade and important noise contributions.	14
2.2	Time line for earth-bound GW detectors.	15
2.3	Illustration of heterodyne and DC readout.	16
2.4	Noise projection for heterodyne readout.	17
2.5	Suspension of GEO 600’s main mirrors.	20
2.6	Shot noise, radiation pressure noise, and combined quantum noise in two configurations of a Michelson interferometer.	23
3.1	Power distribution of different optical modes.	27
3.2	G factors of different resonator configurations.	31
3.3	A resonant two-mirror cavity.	32
3.4	Reflectivity of a cavity in different impedance matching regimes.	32
4.1	Calculated shot noise limited sensitivities for different signal-recycling configurations.	36
4.2	Picture of the beam circulating in the interferometer.	38
4.3	Local mirror surface heights of some of GEO 600’s main optics. First order ROC removed.	39
4.4	Absolute amplitude distribution of the interferometer’s output beam for different mirror qualities and a signal-recycling mirror reflectivity of 98 %.	40
4.5	Simulated absolute amplitude distribution in the interferometer’s output beam for realistic mirrors and different signal-recycling configurations.	43
5.1	The interferometer’s output beam profile before and after the OMC.	46

5.2	The location of the OMC and surrounding optics.	46
5.3	Schematic view of the GEO 600 OMC.	49
5.4	Curing of the epoxy layer between the PZT mirror structure and the OMC baseplate.	50
5.5	Beam in transmission of the OMC for tilted and non-tilted PZT mirror.	50
5.6	PRC length fluctuations.	53
5.7	Illustration of the dither locking concept.	53
5.8	Noise in the power transmitted through the OMC induced by misalignments.	55
5.9	Separation angle between BDO1 and BDO3 for different BDO2 ROCs.	57
5.10	Calculated magnitude of the transfer function of a harmonic oscillator for different amounts of internal friction.	62
5.11	Schematic view of the OMC vacuum tank TCOc.	63
5.12	SM-30 seismic isolators by Minus-K Technology Inc.	63
5.13	Optical path inside TCOc.	64
5.14	Parameters of the laser pulses emitted towards the OMC by cavity-dumping of the dual-recycling cavities for a reflectivity of the signal-recycling mirror of 98 %.	66
5.15	Parameters of the laser pulses emitted towards the OMC by cavity-dumping of the dual-recycling cavities for a reflectivity of the signal-recycling mirror of 90 %.	67
5.16	Shape of the laser pulses emitted towards the OMC by cavity-dumping of the dual-recycling cavities for a reflectivity of the signal-recycling mirror of 90 %.	67
5.17	Transfer function of the PZT summation box.	68
5.18	Measured OLG of the OMC longitudinal control loop.	69
5.19	BDO mirror with attached coil-magnet actuators.	70
5.20	BDO coil-magnet actuator pathways.	71
5.21	OLG of the alignment control for the BDO mirrors.	72
5.22	Illustration of a dead-band control.	72
5.23	Shearing coordinate transformation.	73
5.24	Effect of a gain hierarchy on small actuator separation angle.	74
5.25	GEO 600 sensitivity with and without OMC.	77
5.26	Effect of acoustic white noise injection near TCOb onto GEO 600's sensitivity.	77
5.27	Effect of the signal-recycling mirror reflectivity on the sensitivity.	78
5.28	Optical lever measurement behind BDO3.	78
5.29	Measurement of vibrations on the original suspension in TCOb.	79
5.30	Model of the BDO2 suspension in the AEI cleanroom.	80
5.31	Original suspension of BDO1 and BDO3.	80
5.32	Upgraded suspension of BDO1 and BDO3, as built into TCOb.	81
5.33	Effect of the BDO suspension upgrade.	81
5.34	The interferometer's output beam profile.	83
5.35	OMC mode scan.	84

5.36	Illustration of the difference between maximizing the OMC transmitted power and optimizing GEO 600's strain sensitivity.	85
5.37	Detrimental effect of the original alignment control after the signal-recycling mirror change.	86
5.38	Spectral density of the beacon alignment's error signals.	90
5.39	OLG of the beacon alignment control.	91
5.40	Optical gain: Original vs. beacon alignment system	92
5.41	Spectral density of the optimal beacon alignment's error signals.	93
5.42	OMC mode scan with imperfect interferometer mirror ROC matching. . .	94
5.43	Optical gain: Optimal beacon vs. beacon alignment system	95
5.44	Optical gain: Optimal beacon vs. beacon alignment system in the presence of intentionally increased HOMs.	95
5.45	Drum mode of GEO 600's main mirrors as simulated with ANSYS.	96
6.1	Noise projection to GEO 600's strain measurement.	99
6.2	Effects of different levels of OMC longitudinal FB noise on GEO 600's strain sensitivity.	101
6.3	Projection of the noise due to OMC resonances to GEO 600's strain measurement.	102
6.4	Measured OMC finesse.	104
6.5	Power fluctuations in the OMC transmitted beam for different transmissions. .	105
6.6	Projection of obvious sources contributing to noise in OMC transmitted power, and upper limit for PZT internal displacement noise.	106
7.1	Improvement of the sensitivity of GEO 600 during the GEO-HF upgrade program so far. The improvement is in part due to the implementation of an OMC described in this thesis.	108
A.1	OMC mechanical modes	110
B.1	Measured transfer function of the AA / AI filters of the CDS	116
B.2	Intrinsic noise, or dark noise, of the CDS	117
B.3	Cross-talk between physically neighboring CDS channels.	118
B.4	Performance of the CDS's DACs	119
B.5	Software lock-in realized in CDS	120
B.6	Setup for the performance evaluation of different lock-ins	121
B.7	Input filter of the EG&G Princeton Applied Research model 5302 lock-in .	122
B.8	Comparison of the noise performance of CDS and a hardware lock-in . . .	123
B.9	Simulated contributions to the demodulated signal at DC for different demodulation techniques and different purities of the reference signal used for demodulation.	124
B.10	Comparison of demodulation with square and sinusoidal reference signals .	125
B.11	Round-trip delay of the CDS	126

C.1	The OMC control logic represented in Simulink.	128
C.2	The GAIN_Norm subsystem	129
C.3	The OAA subsystem, containing the alignment control elements.	130
D.1	Flow chart of the OMC lock acquisition algorithm	132
E.1	LabView GUI of the OMC control.	140
E.2	Partial display of the OMC-related LabView logic.	141

List of Tables

2.1	Time table of the GEO-HF upgrade to GEO 600.	22
4.1	Simulated effects of local mirror defects.	41
4.2	Simulated effects of different MSR reflectivities.	42
5.1	Optical design parameters of the OMC.	49
5.2	Number of pendulum seismic isolation stages of different GEO 600 mirrors.	55
5.3	Approximate relative distances between adjacent output optics components. Starting at the signal-recycling mirror. See fig. 1.6 for a depiction of the arrangement of these components.	57
5.4	Comparison of optical configurations of the output optics and resulting separation angles for the actuators BDO1 and BDO3.	58
5.5	Relative loss in the OMC transmitted power due to dithering of the BDO DOFs.	58
5.6	Shot noise limited sensitivity of different designs for the output mode cleaner automatic alignment system in terms of BDO1 and BDO3 misalignments.	59
5.7	Properties of the rubber vibration isolation stages of the OMC.	61
5.8	Alignment control error signal validity.	71
5.9	Alignment control loop gain hierarchy as employed during S6/VSR3.	71
5.10	Mode content of the interferometer's output beam as measured using the OMC as a beam analyzer.	87
5.11	Beacon alignment BDO dither parameters.	88
5.12	Beacon alignment loop characteristics.	89
5.13	Optimal beacon alignment BDO dither parameters.	91
5.14	Optimal beacon alignment loop characteristics. The shape of the OLG is identical to that of the beacon alignment control depicted in fig. 5.39.	91
6.1	Noise contributions in fig. 6.1.	100
6.2	OMC mechanical mode frequencies.	100

Glossary

- \hbar Planck constant, page 21
- c Speed of light, page 1
- M_{\odot} Mass of the sun, page 11
- AA Anti-aliasing, page 115
- AA Automatic alignment, page 54
- ADC Analog to digital converter, page 115
- AEI Albert-Einstein-Institute, page 48
- AR Anti-reflective, page 103
- BDO Beam director output mirror, page 10
- BH Black hole, page 13
- BS Beam splitter, page 19
- CCD Charge-coupled device, page 50
- CDS Control and Data System, page 65
- DAC Digital to analog converter, page 119
- DECIGO DECI-hertz Interferometer Gravitational Wave Observatory, page 11
- DFO Dark-fringe offset, page 16
- DOF Degree of freedom, page 45
- DR Dual-recycling, page 8
- eLISA/NGO evolved Laser Interferometer Space Antenna/New Gravitational Wave Observatory, page 11
- EOM Electro-optic modulator, page 15
- EPICS Experimental Physics and Industrial Control System, page 65

- ESD Electrostatic drive, page 88
- ET Einstein Telescope, page 9
- FB Control feedback, page 48
- FEM Finite element method, page 90
- FP Fabry-Perot, page 11
- FSR Free spectral range, page 28
- FWHM Full width at half maximum, page 29
- GUI Graphical user interface, page 65
- GW Gravitational wave, page 1
- GWIC Gravitational Wave International Committee, page 15
- HG Hermite-Gaussian, page 25
- HOM Higher order optical mode, page 25
- HWHM Half width at half maximum, page 35
- IMC Input mode cleaner, page 18
- IR infrared, page 50
- ITM Input test mass, page 19
- KAGRA GW detector project at Kamioka mine, Japan, page 8
- LCGT Large Scale Cryogenic Gravitational Wave Telescope, page 8
- LG Laguerre-Gaussian, page 25
- LIGO Laser Interferometer Gravitational-wave Observatory, page 6
- LiNb Lithium niobate, page 19
- LISA Laser Interferometer Space Antenna, page 11
- LSC LIGO Scientific Collaboration, page 6
- LV National Instruments LabView, page 65
- MCE Mirror in the east arm, close to the BS, page 51
- MCN Mirror in the north arm, close to the BS, page 51

MFE	Mirror in the east arm, 600 m away from the BS, page 54
MFN	Mirror in the north arm, 600 m away from the BS, page 54
MPR	Power-recycling mirror, page 10
MSR	Signal-recycling mirror, page 10
NS	Neutron star, page 13
OLG	Open loop gain, page 68
OMC	Output mode cleaner, page 14
PR	Power-recycling, page 6
PRC	Power-recycling cavity, page 18
PZT	Piezo-electric actuator, page 47
QPD	Quadrant photodiode, page 75
RCG	Real-time code generator, page 120
RMS	Root mean square, page 51
ROC	Radius of curvature, page 54
RPN	Radiation pressure noise, page 21
RSE	Resonant sideband extraction, page 8
RTP	Rubidium Titanyle Phosphate, page 19
SB	Sideband, page 15
SN	Shot noise, page 19
SNR	Signal to noise ratio, page 45
SQL	Standard quantum limit, page 21
TCOc	Vacuum tank containing the OMC and the GW detection photodiode, page 60
TCS	Thermal compensation system, page 19
TOBA	Torsion-bar antenna, page 8
UDP	User Datagram Protocol, page 65
UGF	Unity gain frequency, page 65
UV	ultraviolet, page 48

1 Introduction

In 1905 Albert Einstein showed that space and time are to be regarded as one entity, the space-time [Ein05]. Measurements of the space-time depend on the frame of reference in which the measurements are taken, a concept later known as special relativity. Einstein later found that the properties of space-time also depend on the presence of gravitation and therefore the presence of mass, extending special relativity to general relativity [Ein16]. For small gravitation values this effect can be expressed as a disturbance, the so-called strain $h_{\mu\nu}$, of the Minkowski metric $\eta_{\mu\nu}$ [Min10] of special relativity.

$$g_{\mu\nu} = \eta_{\mu\nu} + h_{\mu\nu}, \text{ with } \eta_{\mu\nu} = \begin{pmatrix} 1 & 0 & 0 & 0 \\ 0 & -1 & 0 & 0 \\ 0 & 0 & -1 & 0 \\ 0 & 0 & 0 & -1 \end{pmatrix} \quad (1.1)$$

Some of the most fundamental statements of the theory of relativity are that the speed of light (c) is constant for every inertial frame of reference and that information can not travel faster than the speed of light. One consequence of this is that the effects of changes in gravity onto the space-time can not propagate at infinite speed. In fact these effects propagate as *gravitational waves* (GWs) at the speed of light [Ein16, Ein18]. GWs change the gauge-invariant proper distance

$$\Delta l \equiv \int \sqrt{|\Delta s^2|} = \int \sqrt{|g_{\mu\nu} dx^\mu dx^\nu|} \quad (1.2)$$

between freely falling test masses. If we chose the inertial frame at the point of one of the test masses as our coordinate system the GWs take the form of forces that *do* accelerate the (other) test masses. As discussed below, GW detectors' principle of operation is either to measure the variations in the proper distances of test masses, or to measure the forces GWs exert.

Gravitational waves are quadrupole transversal waves in a superposition of + (plus) and x (cross) polarization.

$$\hat{h} = a\hat{h}_+ + b\hat{h}_x \quad (1.3)$$

$$\hat{h}_+ = \begin{pmatrix} 0 & 0 & 0 & 0 \\ 0 & 1 & 0 & 0 \\ 0 & 0 & -1 & 0 \\ 0 & 0 & 0 & 0 \end{pmatrix} \quad \hat{h}_x = \begin{pmatrix} 0 & 0 & 0 & 0 \\ 0 & 0 & 1 & 0 \\ 0 & 1 & 0 & 0 \\ 0 & 0 & 0 & 0 \end{pmatrix} \quad (1.4)$$

An introduction to general relativity and GWs can be found in [Sch09].

GW observations would provide new possibilities for astronomy. GW emissions are expected from systems such as supernovae, compact binary systems consisting of black holes and / or neutron stars, and spinning neutron stars [BM02]. Measurements of a stochastic background of GWs might offer insights into the first 360 thousand years of the universe, during which it was opaque to electro-magnetic radiation [Mag00].

GWs have been observed indirectly by observation of the orbital decay of the binary pulsar PSR B1913+1916 discovered in 1975 by Russel A. Hulse and Joseph H. Taylor, Jr [HT75]. This system is losing energy in a way that is in very good agreement with the predicted energy emission by GWs as presented in fig. 1.1 [WT05]. Hulse and Taylor were awarded the Nobel Prize in Physics in 1993 for their discovery.

The first efforts to directly detect GWs started in the 1960s with so-called resonant bar detectors [Web60]. These were to measure GWs by the inter-atomic forces GWs exert. These forces were to create measurable length changes in meter-long metallic bars. These length changes were strongly enhanced at certain frequencies to which the bars were resonant. Only due to these resonances the detectors were able to reach a good sensitivity to GWs. To veto spurious signals multiple detectors were operated at a distance of several kilometers and only coincident signals were regarded as possible GW signals. Statistically significant events were claimed in 1968 [Web68] but could not be reproduced. An overview of the resonant mass detectors can be found in [CM10], with details on the individual projects in the following papers: AURIGA [VT06, BBC⁺05], ALLEGRO [MJH⁺05], EXPLORER and NAUTILUS [ABB⁺08], Niobe [TLSH⁺00], MiniGRAIL [dWGvH⁺03], and Schenberg detector [Agu11]. While resonant mass detectors have the benefit of being omni-directional, when constructed in the form of a sphere rather than a bar their reliance on resonances to archive good sensitivities to GWs constrains their measurement frequency bands severely. Interferometric GW detectors have a much wider measurement band, as presented in fig. 1.2.

Interferometric GW detectors use light beams as rulers to measure the effects of GWs on the proper distances between test masses, which are typically mirrors. If we assume a Michelson interferometer with the arms of length L oriented for maximum response to a passing GW (as depicted in fig. 1.4) the relative phase difference of the light traveling

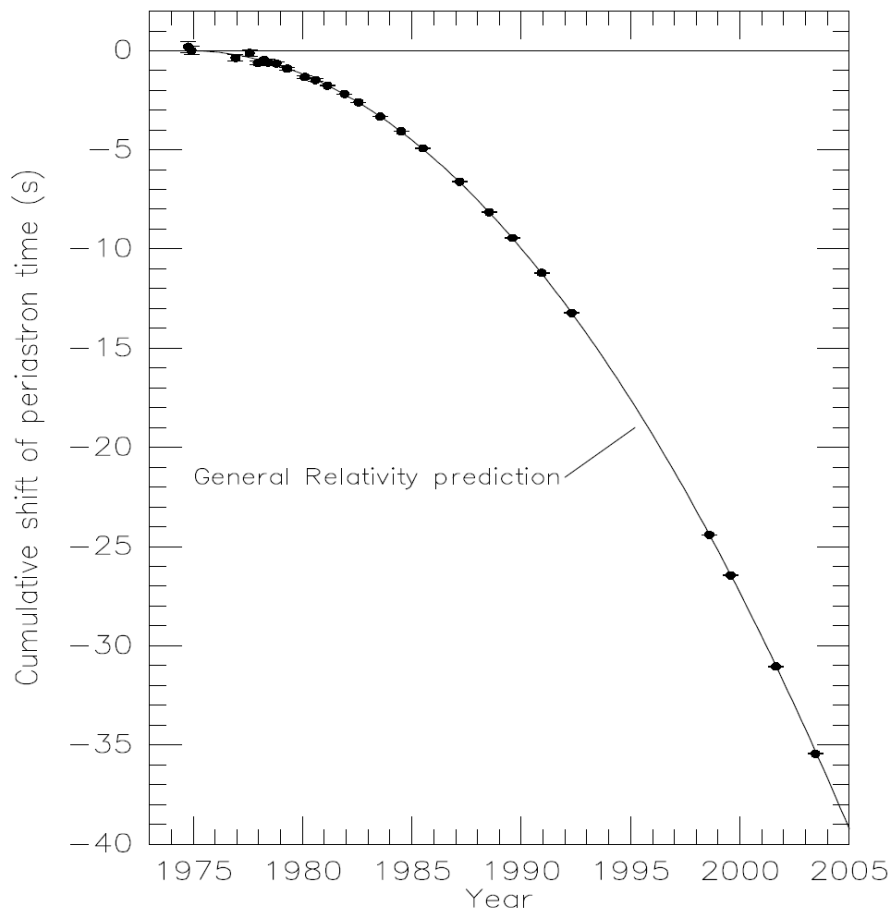


Figure 1.1: Observation of the orbital decay of PSR B1913+1916 from 1975 to 2004. Note the very good agreement between measurements and the decay predicted by general relativity due to the emission of GWs [WT05].

along the two arms is

$$\Delta\phi(t) = h(t) \frac{4L\pi}{\lambda_{\text{GW}}} \quad (1.5)$$

$$h(t) = \frac{\Delta l}{L} \quad (1.6)$$

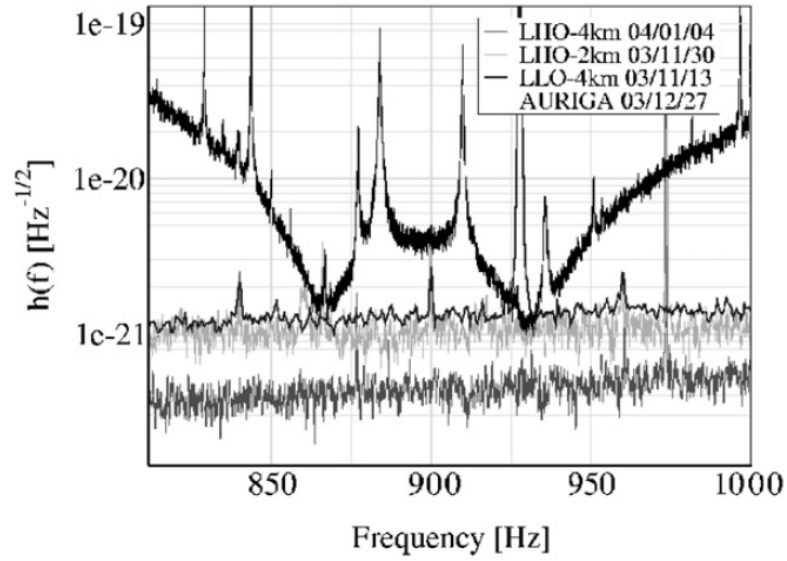
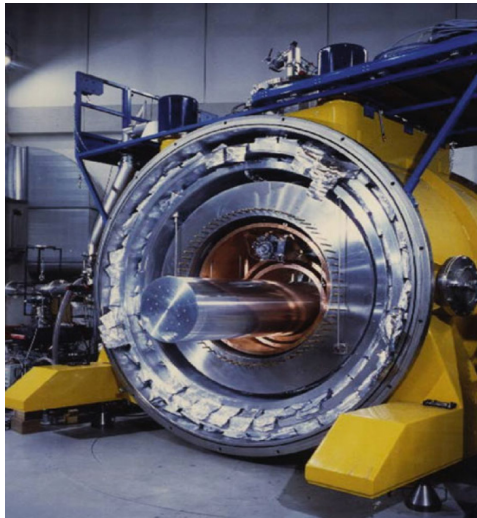


Figure 1.2: Sensitivity comparison of the AURIGA resonant bar detector to early versions of the LIGO interferometric detectors. Note that the LIGO measurement band extends from approximately 100 Hz to several kHz whereas the AURIGA measurement band is less than 200 Hz wide [TT08].



(a) The Auriga resonant bar detector at INFN Legnaro Laboratory [CM10].



(b) The MiniGRAIL resonant sphere detector at Leiden University (grayscale image) [dWGvH⁺03].

Figure 1.3: Example pictures of two resonant mass GW detectors.

with

$\Delta\phi(t)$ = Phase difference the light accumulates traveling along the two arms

Δl = Apparent arm length difference of the two arms

L = Length of the arms

λ_{GW} = Wavelength of the GW

for $L \ll \lambda_{\text{GW}}$. Note that for small GW effects the phase differential $\Delta\phi$ is linearly dependent on the length L of the interferometer's arms.

GW signals from astrophysical sources are far bigger than any GWs that could possibly be created in the lab. As an example we consider a dumbbell consisting of two masses weighing 1 tonne each separated by a rod of 2 m length. In rotations this assembly would create GWs at an amplitude h of

$$h = 2.6 \cdot 10^{-33} \text{ m} \frac{1}{R}, \text{ with } R \text{ being the distance between source and observer} \quad (1.7)$$

To be in the far field regime R should be bigger than 1 GW wavelength λ_{GW} . For a rotation frequency of 1 kHz this means $R > 300 \text{ km}$ resulting in $h \leq 1 \cdot 10^{-38}$ [Sau94]. This is many orders of magnitude below the expected astrophysical sources of approximately 10^{-21} [Gra12].

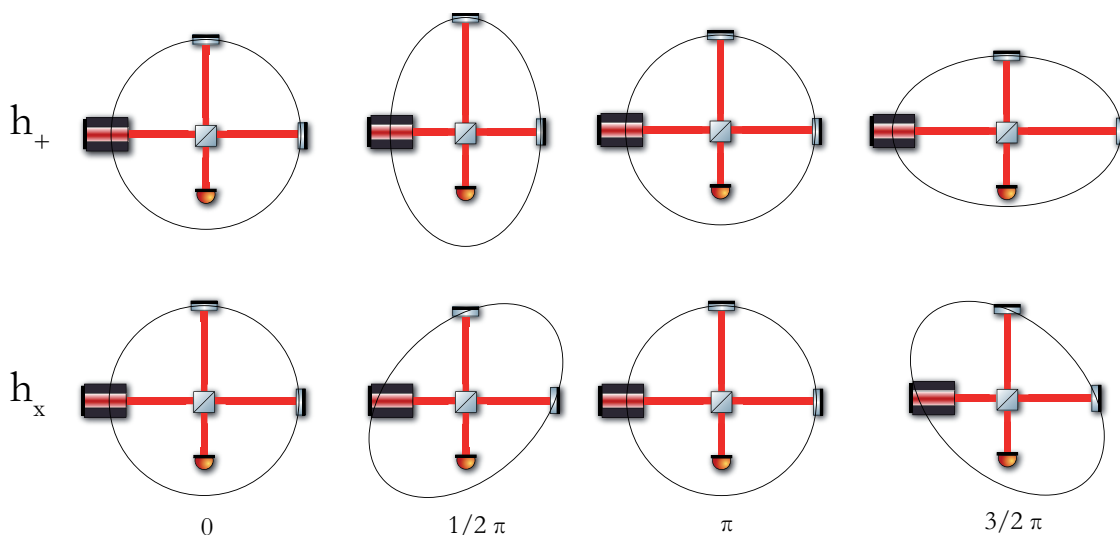


Figure 1.4: Effect of GWs of + and x polarization on a Michelson interferometer. The interferometer is optimally oriented for detection of + polarization.

Earth-bound gravitational-wave detector projects

The interferometric GW detectors built to date all employ advanced implementations of Michelson interferometers. To maximize the phase differential $\Delta\phi$ (see eq. 1.5), and therefore the signal a GW creates, the interferometer's arm lengths are as long as financially feasible. Typically the arm lengths are on the scale of kilometers. Five large-scale interferometric GW detectors have been built, with a sixth currently under construction. To minimize disturbances in the measurements the arms are under ultra-high vacuum conditions.

The strain sensitivities of the four most sensitive GW detectors are presented in fig. 1.5.

LIGO / Enhanced LIGO / Advanced LIGO

The US *Laser Interferometer Gravitational-wave Observatory* (LIGO) originally consisted of two Michelson interferometers with 4 km arm lengths and one interferometer with 2 km arm length. The 2 km interferometer was co-located with one of the other interferometers sharing a common vacuum system. This 2 km interferometer was dismantled in 2010. LIGO was founded in 1992 with the California Institute of Technology (Caltech) and the Massachusetts Institute of Technology (MIT) as main contributors under a grant by the US National Science Foundation (NSF). The detectors are located in Hanford, Washington and Livingston, Louisiana, USA.

LIGO detectors use Fabry-Perot cavities in the arms to increase the circulating power in the arms. As all interferometric GW detectors, the LIGO detectors are operated near the dark-fringe, meaning that the light impinging on the interferometer is reflected towards the laser light source. LIGO employs the *power-recycling* technique in which the light reflected by the interferometer is reflected again towards the interferometer by an additional mirror, the so-called power-recycling mirror. This technique increases the circulating light power and thereby improves the detectors' sensitivities greatly. LIGO's main mirrors are isolated from ground motion by single pendulums. After an upgrade to the interim configuration of Enhanced LIGO from 2007 to 2009 [S⁺09], the 4 km detectors are currently undergoing extensive upgrades towards the Advanced LIGO configuration. Advanced LIGO is expected to increase the detectors' range of sight tenfold with regard to the original configuration, resulting in an increase of the observable volume of space by a factor 1000 [H⁺10].

In 1997 the *LIGO Scientific Collaboration* (LSC) was founded and much of the effort to detect GWs have since been concentrated in it.

VIRGO / VIRGO+ / Advanced VIRGO

The French-Italian VIRGO detector is located in Cascina near Pisa, Italy. It is a Michelson interferometer with power-recycling and 3 km long Fabry-Perot arm cavities. A special

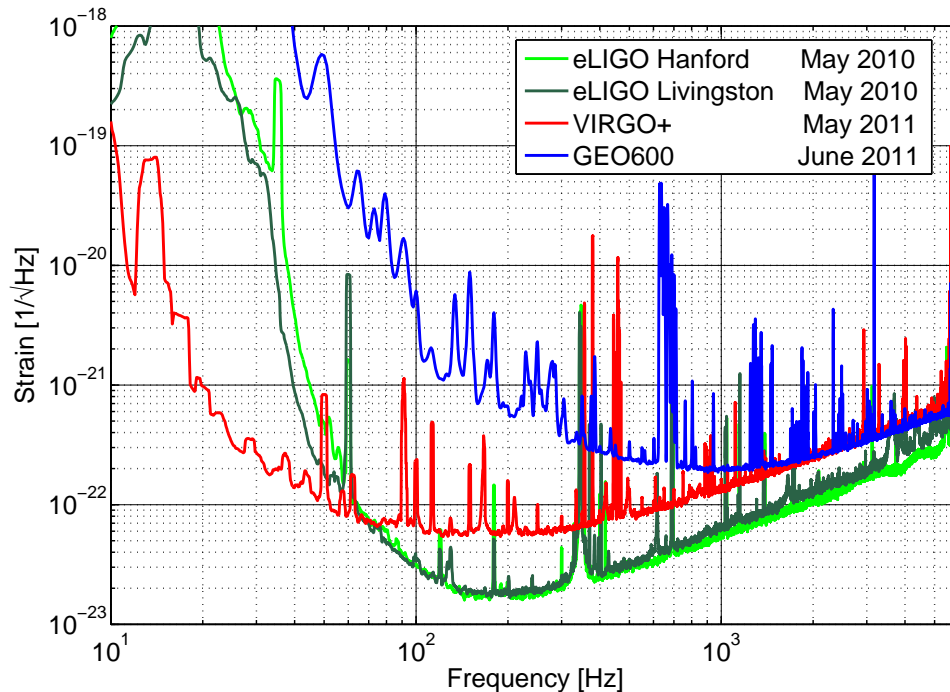


Figure 1.5: Comparison of recent GW detector sensitivities. The LIGO and VIRGO detectors were in their interim Enhanced LIGO / VIRGO+ configurations. GEO 600 had its GEO-HF upgrade program partially completed. The displayed sensitivities are among the best for the respective detectors.

feature of the VIRGO detector is the superattenuators used to isolate the main mirrors from ground motion. Their excellent performance extends VIRGO's measurement band down to approximately 10 Hz. After an upgrade to the interim configuration VIRGO+ from 2007 to 2009 [AAA⁺08], the detector is currently undergoing an extensive upgrade towards the Advanced VIRGO configuration which is expected to improve the detector's sensitivity in a fashion similar to the improvement of Advanced LIGO over original LIGO [AAA⁺11a, The09].

TAMA 300

The Japanese TAMA 300 detector is located at Mitaka campus of National Astronomical Observatory in Tokyo, Japan. It is a Michelson interferometer with power-recycling and 300 m long Fabry-Perot arm cavities [ATT⁺09]. TAMA was damaged by the major earthquake in March 2011.

KAGRA

The Japanese *Large Scale Cryogenic Gravitational Wave Telescope* (LCGT) was renamed KAGRA in January 2012. KA for its location at Kamioka mine and GRA for its connection to gravitation. KAGRA is planned as a Michelson interferometer with 3 km long Fabry-Perot arm cavities. KARGA is going to have several special features. Firstly it is to be constructed underground, reducing the seismic motion of the detector significantly. Secondly its main mirrors are to be set up cryogenically, a measure to reduce thermal noise [LZY⁺10]. Thirdly, it is not only going to employ power-recycling, but also *resonant side-band extraction* (RSE), a way to selectively extract the GW signal from the interferometer [MSN⁺93, K⁺10].

GEO 600

The German-British GW detector GEO 600 is located in Ruthe near Hannover, Germany. It is a *dual-recycled* Michelson interferometer with cavity-less 600 m long arms. These arms are folded once vertically, to give an effective length of 1200 m as depicted in fig. 1.6. The term dual-recycled describes the fact that GEO 600 employs both power-recycling and signal-recycling [SM91]. Signal-recycling reflects signals that were generated in the interferometer by differential arm length motion due to e.g. GWs back into the interferometer, making it resonant to GWs. Details of this technique are presented in section 5.5. Not only is GEO 600 the only GW detector employing signal-recycling, it is also the only one to use squeezed-vacuum injection to reduce quantum shot noise. These techniques are otherwise planned or considered only for second generation detectors like Advanced LIGO, Advanced VIRGO, and KARGA. This technological edge allowed us to improve GEO 600's sensitivity to levels close that of the much larger LIGO and VIRGO detectors [G⁺10, The11, BHJZ12].

The GEO-HF upgrade program of the GEO 600 detector aims to improve the detector's sensitivity at frequencies above 600 Hz where the sensitivity is limited by shot noise. The project began in 2008 and will be completed in 2012 or 2013 [LAD⁺10]. Its scope is detailed in the next chapter.

Torsion-bar antennas

The *torsion-bar antenna* (TOBA) is a new GW detector design that might be able to extend GW measurements on earth to below 1 Hz and close the gap in measurement bands between earth-bound detectors and the LISA space-based GW project described below (see also fig. 1.7). Interferometric earth-bound GW detectors are severely challenged to extend their measurement bands to below tens of Hertz. The reason for this is mainly mirror motion due to vibrations of the earth's surface, the so-called seismic noise. A related somewhat weaker noise source is the Newtonian or gravity gradient noise. It is caused by fluctuations in the mass distributions around the mirrors which couple to mirror motion via gravitational pull [BCD⁺11]. A TOBA consists of two metallic bars with lengths on meter

scales that are suspended from a common point. GWs then cause rotation of these bars with respect to one another. The common suspension point and spatial compactness of the setup reduces the TOBA's susceptibility to seismic and Newtonian noises greatly when compared to interferometric GW detectors [AIY⁺10, IAT⁺11]. Two prototype TOBAs have been build in Kyoto and Tokyo, Japan [Oka].

Einstein Telescope

The European *Einstein Telescope* (ET) project designs a third generation detector. The design work on ET studies advanced interferometric techniques such as combining multiple detectors with good sensitivities at different frequency ranges into one combined detector, known as the 'xylophone' approach, and subtraction of Newtonian noise. ET's design currently calls for an underground detector [PAA⁺10].

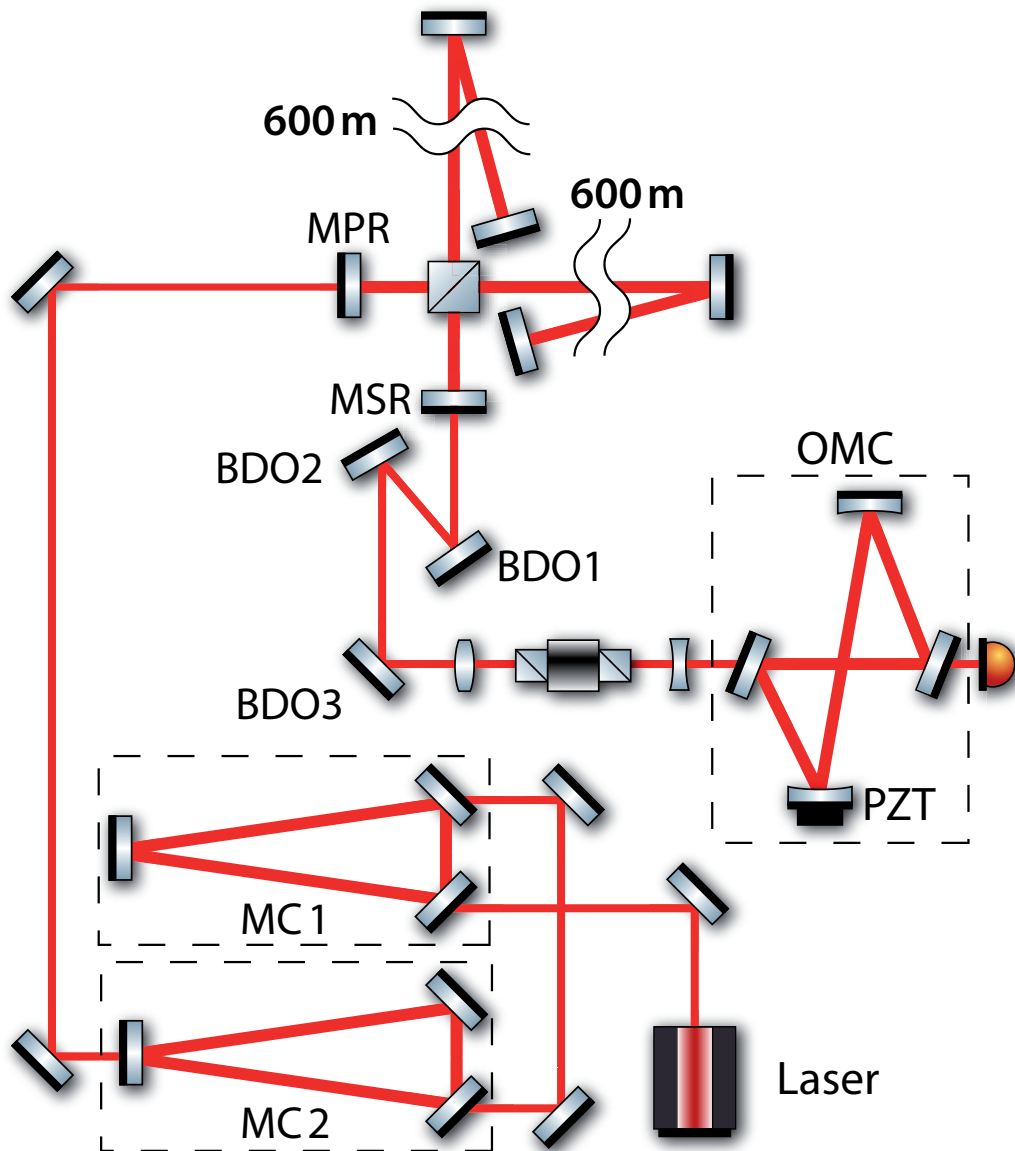


Figure 1.6: Simplified GEO 600 layout. Not to scale. The arms are folded vertically, the end mirrors are depicted off-axis for clarity only. **MPR:** Power-recycling mirror, **MSR:** Signal-recycling mirror, **BDO:** Beam director output mirror, **MC:** Mode cleaner, **OMC:** Output mode cleaner.

Space-based gravitational-wave detector projects

While techniques exist to alleviate the effects of seismic and Newtonian noise that limit the low-frequency performance of earth-bound GW detectors, a considerably better performance at low frequencies is to be expected of the space-based projects described below [BBB⁺01, BBB⁺12].

LISA / eLISA/NGO / LISA Pathfinder

The proposed *Laser Interferometer Space Antenna* (LISA) project aims at the detection of GWs at frequencies below 1 Hz [Boa11]. LISA is to consist of three satellites in an equilateral triangle formation separated by several million kilometers from one another. Their relative distances would be measured interferometrically. This would enable LISA to observe GW sources that are inaccessible to current and planned earth-based GW detectors, such as massive black holes with masses of $10^5 - 10^7 M_\odot$, with M_\odot being the mass of the sun. The massive size of these objects limits most of their dynamics to these low frequencies. Recently the possibility of implementing a somewhat scaled-down version of the project under the name *evolved Laser Interferometer Space Antenna/New Gravitational Wave Observatory* (eLISA/NGO) has come under consideration [eLI12, JBC⁺11, R⁺12]. A precursor mission to test the technical principles is planned to launch in 2014 under the name LISA Pathfinder [RM10, AAA⁺11b].

DECIGO / DECIGO Pathfinder / Pre-DECIGO

The Japanese *DECi-hertz Interferometer Gravitational Wave Observatory* (DECIGO) projects aims at the detection of GWs at frequencies between 0.1 and 10 Hz. DECIGO is to consist of three satellites in an equilateral triangle formation separated by one million kilometers from one another. Unlike LISA the arms are planned as Fabry-Perot cavities rather than simple beam lines [KAS⁺11]. Two precursor mission are planned for DECIGO: DECIGO Pathfinder [AKS⁺09] and Pre-DECIGO [SKM⁺09].

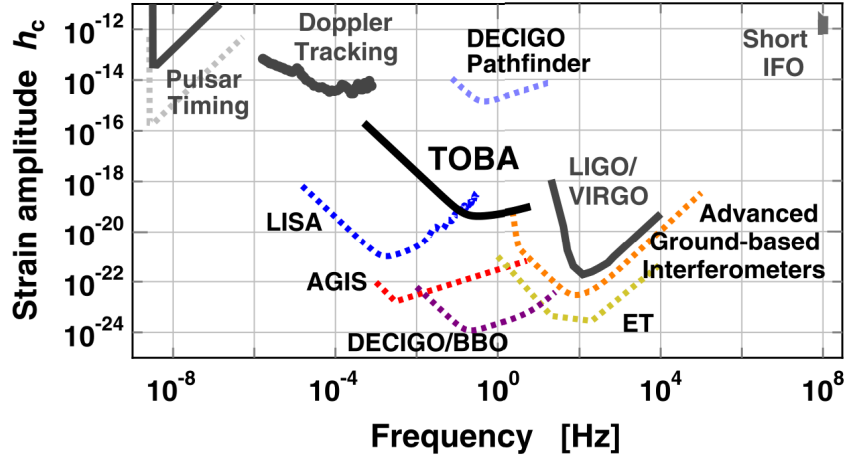


Figure 1.7: Overview of the measurement bands and sensitivities of different GW detection efforts [AIY⁺10]. Details on pulsar timing [HAA⁺10], doppler tracking [Arm06], AGIS [HJD⁺11], and ET [PAA⁺10] can be found in the respective references.

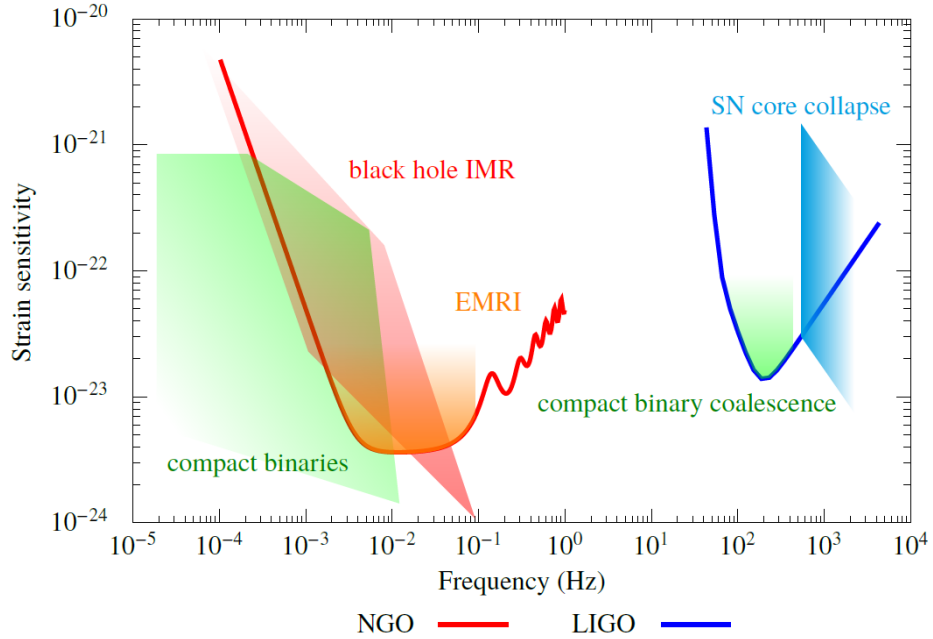


Figure 1.8: Comparison of the proposed NGO project and the LIGO detectors. NGO is sensitive to the inspiral, merger and ringdown (IMR) of massive black hole binaries (in red), the quasi-monochromatic signal from compact binaries (in green) and the extreme mass ratio inspirals (EMRIs, in orange). Ground based detectors operate in the acoustic frequency range and are sensitive to the coalescence of compact binaries (in green) and ‘burst’ events like supernovae core collapses (in cyan) [JBC⁺11].

2 The GEO-HF upgrade program of GEO 600

The smaller scale of GEO 600, when compared to the LIGO and VIRGO detectors, puts GEO 600 at an inherent disadvantage in sensitivity. From its inception GEO 600 was designed to compensate for this by employing more advanced techniques. GEO 600 for example pioneered the use of techniques such as signal-recycling [SM91, Gro03] and monolithic optics suspensions [Goß04], which are now propagating to the LIGO and VIRGO detectors. VIRGO+ implemented monolithic suspensions [L⁺10], which are also planned for Advanced LIGO [CBB⁺12], and both Advanced VIRGO and Advanced LIGO will employ signal-recycling [The09, H⁺10]. To keep GEO 600's sensitivity contemporary even as LIGO and VIRGO are upgraded, GEO 600 would yet again pioneer new technologies as part of the GEO-HF program.

The GEO-HF upgrade program of GEO 600 was first proposed in 2005, with the goal of improving GEO 600's high frequency sensitivity so that it would be comparable to the interim stages Enhanced LIGO and VIRGO+ of the other large-scale GW detectors [Dan05]. Evolved versions of the design can be found in [WAA⁺06, Lüc09]. The upgrade started in 2009 and concentrates on frequencies above 600 Hz where GEO 600 is limited by shot noise. At lower frequencies only small improvements of the sensitivity are possible due to noise contributions by coating Brownian noise and thermo-refractive noise. Changing these noise levels would require the invasive and costly procedure of replacing GEO 600's main optics. At frequencies below 50 Hz GEO 600's sensitivity is dominated by seismic noise caused by motion of the ground. An improvement in this frequency range would have required an improved seismic isolation system, beyond the current triple-stage monolithic pendulum suspension of GEO 600's main optics. Since such an endeavor is similarly invasive to a change of the main optics it was decided to forgo such an upgrade. The GEO-HF upgrade takes place partly in the time frame in which LIGO and VIRGO are undergoing their upgrades to the advanced detector stages and are not taking data. Performing the upgrade with minimal downtime of GEO 600 was therefore of particular importance. The evolution of GEO 600's sensitivity as originally envisioned for the GEO-HF program is presented in fig. 2.1.

GEO 600 is, at low frequencies, less sensitive than Enhanced LIGO and VIRGO+. This makes it difficult to identify low frequency GWs, emitted from binary coalescence events between *black holes* (BHs) and / or *neutron stars* (NSs) in their early inspiral phase, with GEO 600. In a network of detectors GEO 600 can however contribute crucial insights into the later (merger and ringdown) phases of such events which emit GWs at higher frequencies. It might allow insights into sources of burst-like GWs like magnetars and certain types of supernovae [YMM⁺10].

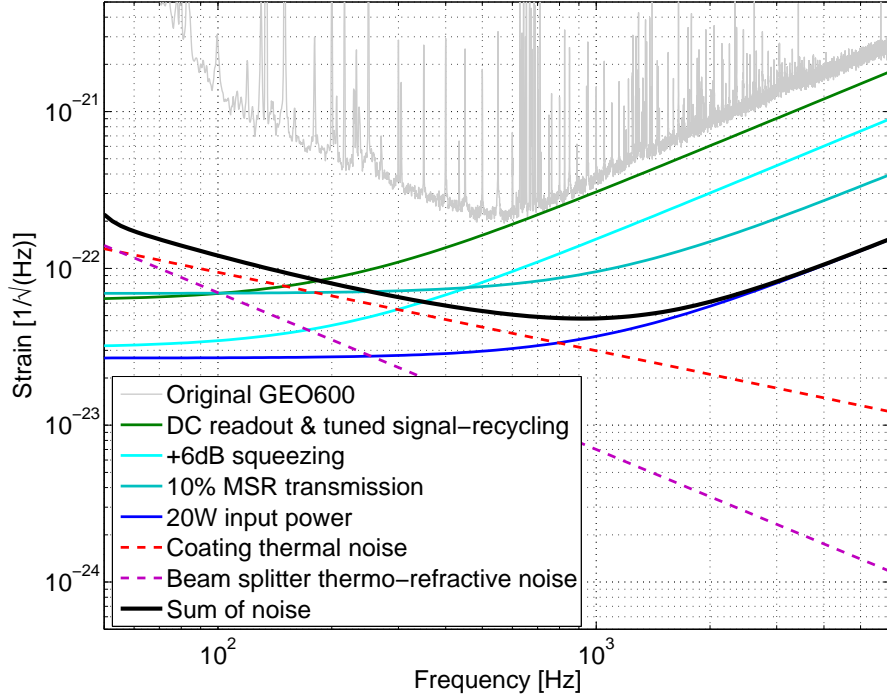


Figure 2.1: Planned evolution of GEO 600’s sensitivity over the course of the GEO-HF upgrade. Only shot noise and thermal noises were taken into account here. Note the limitations to sensitivity by thermal noises in the medium frequency range.

Since October 2011 GEO 600 is the only interferometric GW detector taking data. This situation is expected to last until approximately early 2015 when the Advanced LIGO and Advanced VIRGO detectors are presumed to become operational. See fig. 2.2 for the time line of earth-bound GW detection. While GEO 600 is the only operational interferometric GW detector the search for GWs in GEO 600’s data profits greatly from the incorporation of data from other sensors, such as neutrino detectors [V⁺11], gamma-ray telescopes [GCG⁺04, MLB⁺09], and radio telescopes [PCC⁺10] to distinguish between detector glitches and actual GW detection events. This technique is generally known as multi-messenger astronomy [Sha11].

In the following sections we will give an overview of the different improvements the GEO-HF upgrades brings to GEO, and their respective current states. Please refer to chapter 5 for details on the *output mode cleaner* (OMC), on which this thesis focuses.

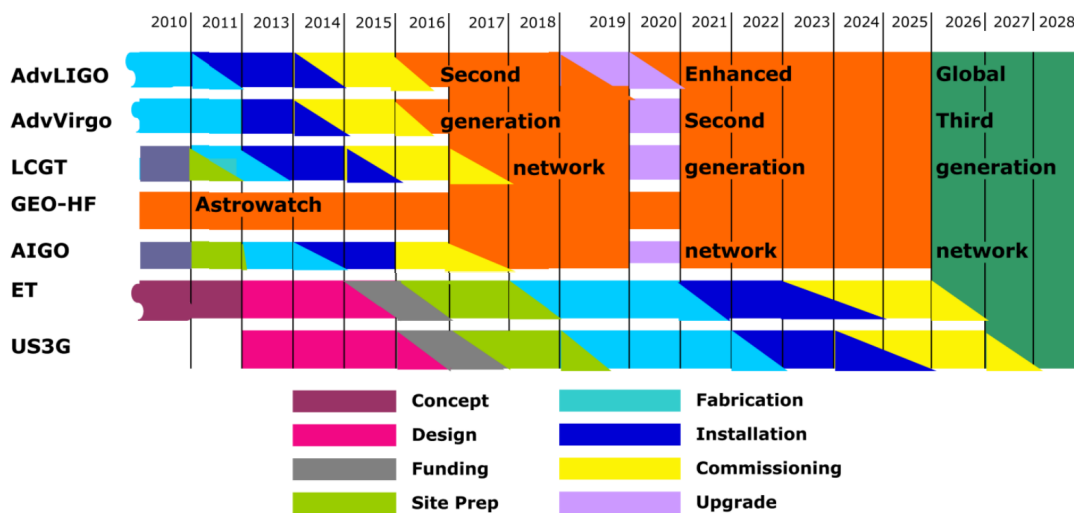


Figure 2.2: Time line for earth-bound GW detectors as outlined by the *Gravitational Wave International Committee* (GWIC). Note that LCGT has since been renamed KAGRA and the Australian AIGO project was abandoned, with the new US-Indian LIGO-India project as a possible alternative [Gra12].

Change of the readout technique from heterodyne readout to homodyne / DC readout

A particularly challenging task in operating a GW detector is to extract the information about the relative arm length fluctuations from the interferometer's output port. This is because GW signals are encoded in the output beam as phase fluctuations on the order of 10^{-12} radians. Originally the so-called heterodyne readout was used at GEO 600. In this radio-frequency *sidebands* (SBs) at f_{SB} are imprinted on the laser beam using an *electro-optic modulator* (EOM) before it enters the interferometer (see fig. 2.3). The interferometer's arms are *not* of equal length. This so-called Schnupp asymmetry amounts to 69 mm in GEO 600. In this configuration the interferometer reflects the main component (the carrier) of the laser light back towards the laser almost entirely but lets the SBs exit the interferometer through the output port. Relative fluctuations of the arm lengths off of this position will lead to some / more carrier light leaving the interferometer through the output port. This creates a radio-frequency beat signal between the SBs and the carrier from which the information about the relative arm length fluctuations is extracted. The reason to originally decide on this somewhat complex readout technique was the expectation that a readout at radio-frequencies would attenuate technical noises such as fluctuations in the laser amplitude. While this was somewhat successful heterodyne readout showed to possess several drawbacks. It leads to an unnecessarily high level of shot noise because the demodulated signal is not only constituted by elements originally around f_{SB} , but also integer multiples of f_{SB} . Heterodyne readout also introduced new technical noise sources that proved to be extremely challenging. Instabilities in the amplitude and

frequency of the SBs directly coupled to noise in the GW signal, creating a noise level that nearly limited GEO 600's sensitivity across a wide frequency range (see fig. 2.4).

The drawbacks of heterodyne readout lead us to develop the so-called DC readout technique [HGD⁺09]. In this the interferometer's arms are set to a relative length difference, the *dark-fringe offset* (DFO), that allows a small amount of carrier light to exit the interferometer. Any fluctuations in the relative arm length are then directly visible in the amount of carrier light at the output port. This technique reads out the interferometer at audio-band frequencies close to 0 Hz or DC (hence the name), rather than radio-frequencies. It lowers the shot noise level, for identical signal level, by between a factor of $\sqrt{1.5}$ and $\sqrt{2}$ with regard to heterodyne readout [HGD⁺09]. Another benefit of DC readout is that it allows for the implementation of squeezed vacuum injection to reduce shot noise as we showed at GEO 600 [The11].

DC readout was implemented at GEO 600 in September 2009 [DGP⁺10], and simultaneously in Enhanced LIGO [FSLA⁺12]. The Advanced LIGO, Advanced VIRGO, and KAGRA detectors are also going to employ DC readout [H⁺10, The09, ASM⁺12].

Change of the tuning of the signal-recycling

Signal-recycling creates a resonance in the interferometer to signals generated by differential arm length motions, as caused by GWs, by creating a cavity for such signals [SM91]. This cavity is created by placing the so-called signal-recycling mirror into the output beam of the interferometer as depicted in fig. 1.6. The properties of this cavity, and therefore the resonance, have to be optimized to realize the maximum benefit from signal-recycling. In the original GEO 600 setup the signal-recycling resonance was detuned from DC to a

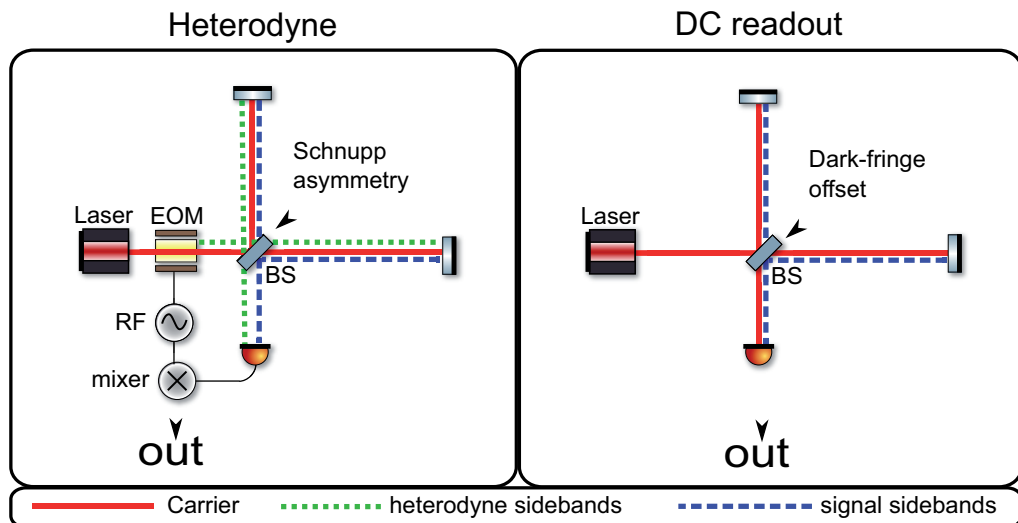


Figure 2.3: Illustration of heterodyne and DC readout.

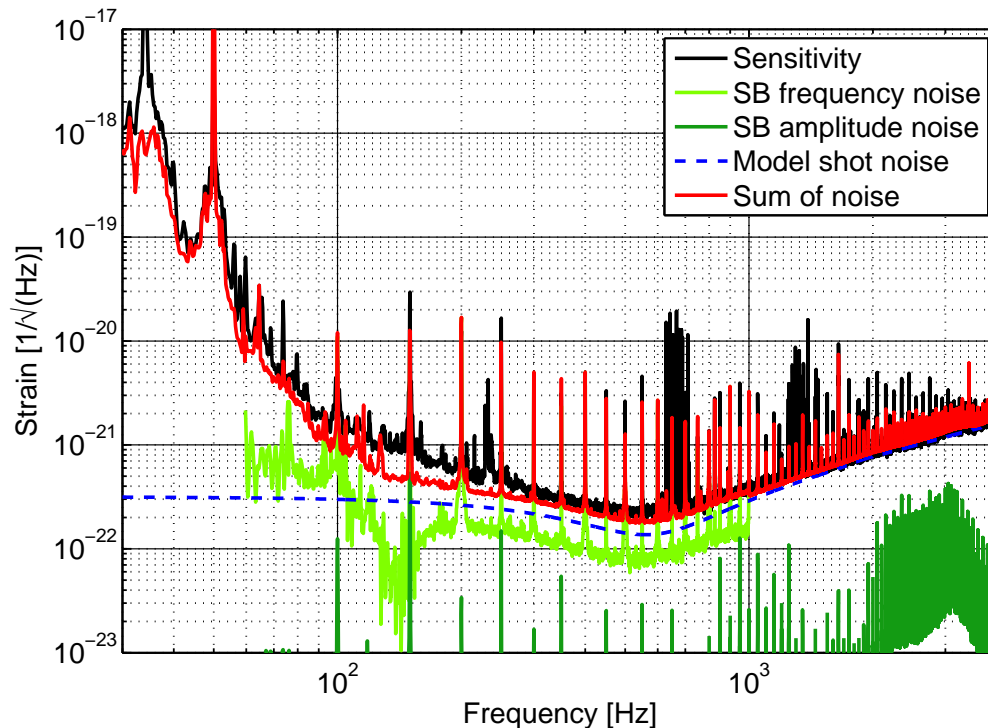


Figure 2.4: Excerpt of a noise projection for heterodyne readout with signal-recycling detuned to 550 Hz. Note the significance of the SB frequency noise which is created by imperfect frequency stability of the radio-frequency SBs at f_{SB} . The sum of noise is calculated taking noise sources into consideration that were omitted in this graph for clarity. For details on the noise projection procedure refer to section 6.1.

frequency of 550 Hz. As part of the GEO-HF upgrade the tuning was changed to DC, or 0 Hz. The bandwidth of the signal-recycling cavity was later increased by decreasing the the signal-recycling mirror's reflectivity from 98 % to 90 %.

The benefit of these changes are an improved shot noise limited sensitivity of GEO 600 at all frequencies except for a small frequency band a few tens of Hertz wide around 550 Hz. Furthermore these changes improve the effectiveness of frequency-independent squeezed vacuum injection at frequencies below 300 Hz [Kha11]. Details on the changes to the signal-recycling and their effects are presented in chapter 4.

The output mode cleaner

The output beam of GEO 600's interferometer contains spurious components that carry non-extractable GW information. Because these components contribute to shot noise but do not contribute GW signal they impair GEO 600's shot noise limited sensitivity. This is especially true after the changes made to the signal-recycling as part of the GEO-HF upgrade, which increased the power of these spurious beam components so much that they constitute 90 % of the output beam's power, as described in section 5.5. An OMC is also necessary for the effective injection of squeezed vacuum, another part of the GEO-HF upgrade program. Squeezed vacuum injection reduces shot noise, as detailed later in this chapter. It however only reduces shot noise in the GW carrying beam component. When other beam components dominate, the overall shot noise can not be effectively reduced.

It was the goal of this thesis to implement an OMC into GEO 600 without introducing new noise sources that would limit GEO 600's performance. To this end requirements on the OMC control systems were formulated based on numerical simulations. The OMC was then implemented and its performance examined as described in chapters 5,6.

Laser power increase

An obvious way to improve shot noise limited sensitivity in an interferometric GW detector is to increase the power circulating in the interferometer. This is because the shot noise scales with the power P as \sqrt{P} whereas the signal scales linearly with P . As part of the GEO-HF upgrade the original GEO 600 laser system with a maximum output power of approximately 15 W [ZBD⁺02] was exchanged for a more powerful model with a maximum output power of 35 W [WSW⁺08]. Both systems were developed and built at the Albert-Einstein-Institute in Hannover, Germany, with the latter one being identical to the ones employed in the Enhanced LIGO detectors.

Several limitations in the original GEO 600 design need to be overcome to allow usage of the full available laser power. GEO 600's main mirrors are suspended via multiple pendulum stages, with resonances near 1 Hz [Goß04]. As presented in subsection 5.4.1 these harmonic oscillators amplify motion at their resonance frequencies. This was recognized as problematic during GEO 600's design phase and so-called *local controls* were implemented at each pendulum's top stage (see fig. 2.5) to suppress motion around the respective pendulum's resonance frequencies. These local controls employ an optical readout of the positions of the fibers that suspend the intermediate masses. This readout was too susceptible to stray laser light to allow for an increase in circulating light power in the main interferometer beyond 3 kW. We implemented a modulation-demodulation, lock-in type, readout of the local control sensors that allowed for a substantial increase in circulating power. Another limitation arose from the design of the two *input mode cleaners* (IMCs) that are used in the frequency stabilization between the laser and the *power-recycling cavity* (PRC), and also clean the laser's spatial beam profile before it enters the interferometer. Due to the high finesse of the IMCs of 2700 and 1800 for the first and second IMC

respectively, the power circulating in the IMCs is resonantly enhanced to a level at which the radiation pressure apparently can not be handled by the actuators controlling the IMCs' lengths. A change of the IMCs' mirrors that will reduce their finesse to approximately 300 is planned for later this year. Yet another limitation arises from the EOMs used to imprint radio-frequency SBs onto the laser beam before it enters into the interferometer. The *Lithium niobate* (LiNb) crystals used in the current EOMs are not able to withstand the envisioned laser powers over prolonged durations of time. We will replace these EOMs with EOMs that use *Rubidium Titanyle Phosphate* (RTP) crystals, whose laser power damage threshold is approximately twice as high as that of the LiNb crystals ($> 600 \text{ MW/cm}^2$ compared to 280 MW/cm^2 for 10 ns laser pulses). Similar EOMs were tested successfully at similar power levels at the LIGO detectors [DMF⁺12].

Overall these changes will increase the power circulating inside the interferometer from approximately 3 kW to approximately 30 kW.

Thermal compensation system

With the expected tenfold increase in power circulating in the interferometer the absorption inside the *beam splitter* (BS) becomes an important issue, even though it was established to be very low at less than 0.5 ppm/cm [HW12]. The absorption creates a thermal profile in the beam splitter. Due to the thermo-refractive effect and thermal expansion of the beam splitter's material, this creates a collimating lens in the beam splitter. Because only the light going into the east arm passes through the beam splitter, whereas the light to the north arm is reflected at the beam splitter's surface, this creates an asymmetry between the arms. This reduces the contrast in the interferometer and reduces its sensitivity to GWs. The thermal lens can be partially compensated for by heating either the beam splitter or the far east mirror with appropriate heating patterns. Investigations into implementing a *thermal compensation system* (TCS) at GEO 600 are currently underway [Wit11].

GEO 600 is the only GW detector in which this effect appears strongly in the beam splitter because it does not employ Fabry-Perot arm cavities. In the other GW detectors thermal lenses appear in the mirrors in the arms that are close to the beam splitters, commonly called the *input test masses* (ITMs). Thermal compensation systems were installed at the LIGO detectors in 2004 [AG⁺10], and at VIRGO in 2008/2009 [AAA⁺11a, FR10]. Investigations regarding adaptation of these systems for the Advanced LIGO and Advanced VIRGO detectors are currently underway [Wil10, Faf10].

Squeezed vacuum injection

The quantum nature of light limits the sensitivities GW detectors can achieve. This quantum nature manifests itself in two forms:

- **Shot noise (SN):** Shot noise originates from fluctuations in the phase quadrature of the vacuum noise. Its spectral density is white and the shot noise limited amplitude

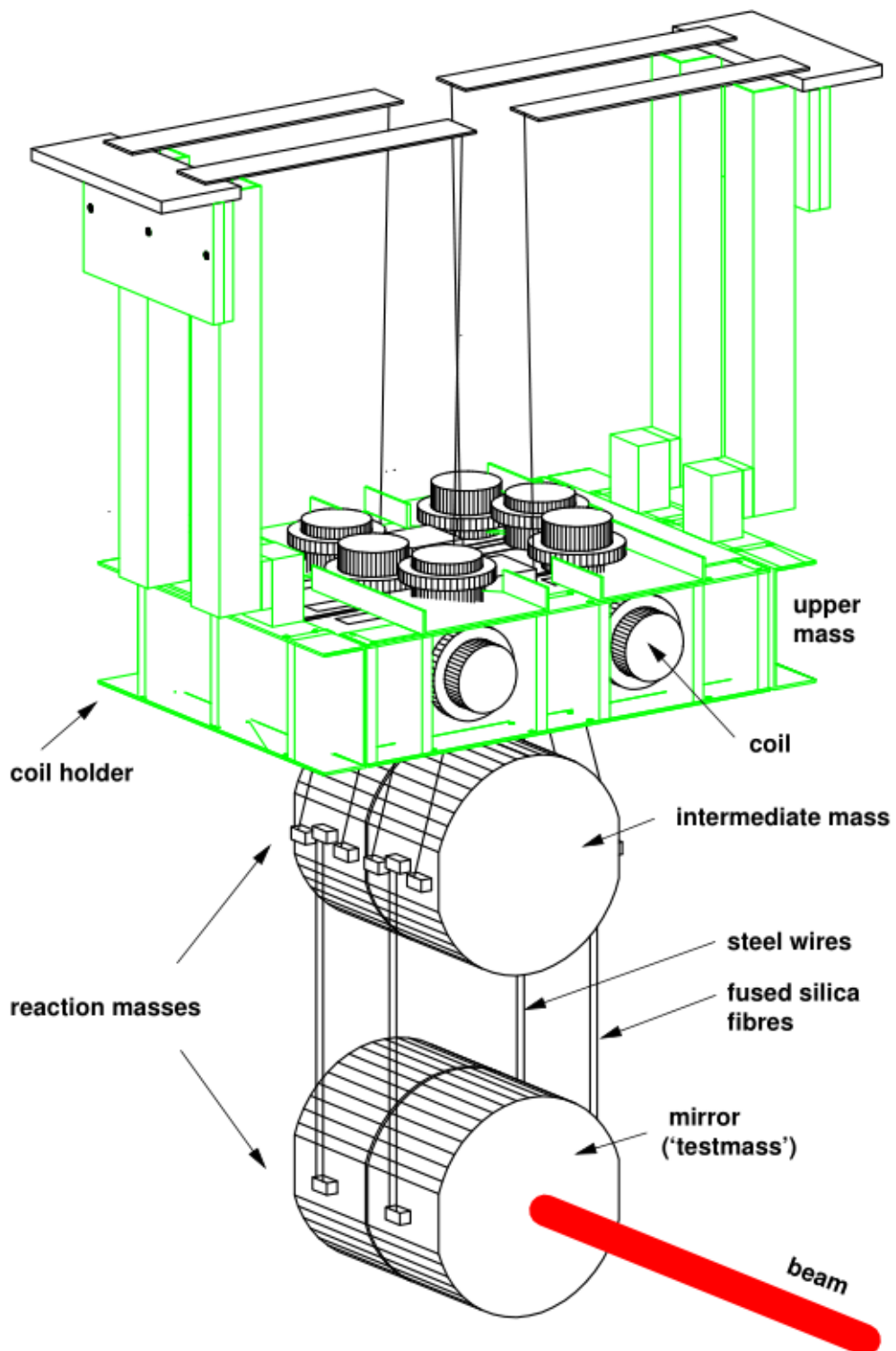


Figure 2.5: Suspension of GEO 600's main mirrors. The local control sensor assembly is located inside the upper mass construction [Gro03].

spectral density strain sensitivity of a GW detector is [Kha11]:

$$h_{\text{SN}} = \frac{1}{L} \sqrt{\frac{\hbar c \lambda}{\pi P}} \quad (2.1)$$

with

L = Length of the interferometer

\hbar = Planck constant

c = Speed of light

λ = Wavelength of the light used in the GW detector

P = Light power inside the interferometric GW detector

- **Radiation pressure noise (RPN):** Radiation pressure noise originates from fluctuations in the amplitude quadrature of the vacuum noise. These fluctuations exert fluctuating forces on the test masses of the interferometer. Since the test masses can be considered as freely falling at frequencies above the pendulum resonances, RPN in a GW detector has typically a $1/f^2$ characteristic, with its limit to the sensitivity being [Kha11]:

$$h_{\text{RPN}}(f) = \frac{1}{m f^2 L} \sqrt{\frac{4 \hbar P}{\pi^3 c \lambda}} \quad (2.2)$$

with

m = Mass of the test mass

f = Measurement frequency

The overall quantum noise can be calculated as

$$h_{\text{QN}}(f) = \sqrt{h_{\text{SN}}^2 + h_{\text{RPN}}(f)^2} \quad (2.3)$$

As is evident from eqs. 2.1,2.2,2.3 an increase in power circulating in the GW detector decreases shot noise but increases radiation pressure noise when normalized to a constant GW signal level. A consequence of this connection between shot noise and RPN is the fact that, for any power, the quantum noise curve always touches on one point a $1/f$ line in the GW detector's sensitivity, the minimal optical readout noise for the respective frequency. This line, which is called the *standard quantum limit* (SQL) can be calculated as

$$h_{\text{SQL}}(f) = \frac{1}{\pi f L} \sqrt{\frac{4 \hbar}{m}} \quad (2.4)$$

The location of this touching point can be chosen by varying either the power in the detector, as depicted in fig. 2.6, or by employing squeezed vacuum injection.

GEO 600's sensitivity is limited by shot noise at frequencies above approximately 500 Hz, but is not limited by RPN. In this case an increase in circulating power is beneficial, but as described before, challenging. GEO 600 therefore implemented the injection of squeezed vacuum into the interferometer's output port in April 2010, and uses it routinely since June 2011. Squeezing reduces the fluctuations in one quadrature of the vacuum noise and increases it in the other quadrature. The size of this asymmetry, the squeezing strength, is a measure for the quality of the squeezing source, with the best sources reaching approximately 13 dB [ESB⁺10]. A particular challenge in the creation of squeezing sources for GW detectors is that strong squeezing is required down to audio-band frequencies [Che07]. Another challenge is the required long-term stability of the squeezing source. Stable squeezing on hour time-scales is required, with maintenance intervals spaced weeks or months apart.

The strength of the GEO 600 squeezing source is approximately 10 dB. The best resulting observed enhancement of GEO 600's shot noise limited sensitivity to date is 3.5 dB [The11]. As described in section 6.2 this value is lower than the expected 6 dB due, in part, to excess losses at the OMC that are currently under investigation, and other noise sources.

Future GW detectors are not only going to be limited by SN, but also by RPN at lower frequencies. To extend the benefit of squeezing into the frequency region in which RPN dominates, a frequency dependent squeezing would be beneficial. This is currently under investigation as an upgrade to second generation GW detectors [Kha10, MMC⁺11, BBB⁺12].

Table 2.1: Time table of the GEO-HF upgrade to GEO 600.

Date	Upgrade
07/2009	Tuned signal-recycling
09/2009	DC readout
12/2009	OMC installation
04/2010	Squeezed vacuum injection installation
10/2010	Signal-recycling mirror exchange
06/2011	Use of 5 W instead of 3 W laser power, routinely using squeezing
09/2011	Upgrade of the laser to a 35 W system
2012-2013	Planned: Use the full laser power of 35 W
2012-2013	Planned: Changes to the input mode cleaners, installation of a TCS

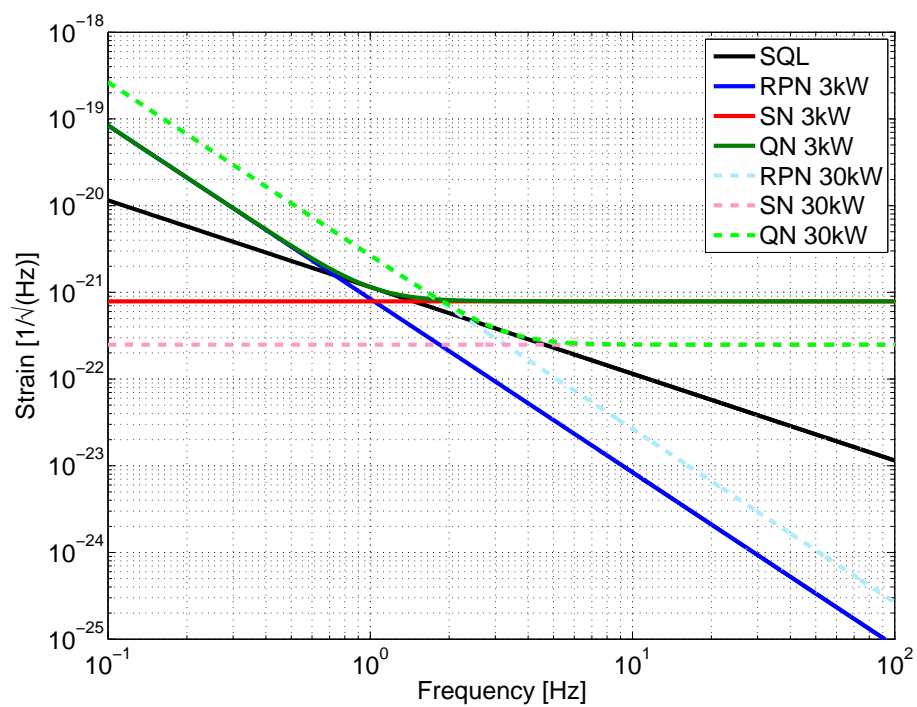


Figure 2.6: Shot noise, radiation pressure noise and combined quantum noise in two configurations of a Michelson interferometer without arm cavities and signal-recycling. Solid: $P = 3 \text{ kW}$, $\lambda = 1064 \text{ nm}$, $m = 5.6 \text{ kg}$, and $L = 2400$, corresponding to the original GEO 600 parameters. Dashed: Increased power $P = 30 \text{ kW}$ as envisioned for the final stage of the GEO-HF program. Note that the standard quantum limit is touched once by the quantum noise of each of these two configurations.

3 Optical resonators

An optical resonator, or optical cavity, is an arrangement of optics in which a light beam can travel in a closed path. A cavity can be used to analyze or manipulate the contents of a light beam. We will present the methods used to describe a beam as a superposition of different optical modes. Then we will lay out the fundamental functional principle of optical resonators. Finally we will expand the discussion to the interaction between cavities and beams of high higher order optical mode content.

3.1 A light beam as a superposition of optical modes

Any beam can be expressed as a superposition of a fundamental and *higher order optical modes* (HOMs) [Oug82]. It is advantageous to describe beams in the self-similar¹ *Hermite-Gaussian* (HG) or *Laguerre-Gaussian* (LG) modes as presented in eq. 3.1, [KL66, BH84]².

$$\psi_{m,n}^{\text{HG}}(x,y,z) = N_{m,n}^{\text{HG}} \left(1 + \left(\frac{z}{z_{\text{R}}} \right)^2 \right)^{-1/2} H_m(a(x))H_n(a(y))\exp(e_{m,n}) \quad (3.1a)$$

$$\psi_{p,l}^{\text{LG}}(x,y,z) = N_{p,l}^{\text{LG}} \left(1 + \left(\frac{z}{z_{\text{R}}} \right)^2 \right)^{-1/2} a(r)L_p^{(l)}(a^2(r))\exp(e_{p,l}) \quad (3.1b)$$

with

ψ = Amplitude distribution

z = Position along the optical axis. Beam waist at $z = 0$

$N_{m,n}^{\text{HG}} = \left(\pi\omega_0^2 2^{m+n-1} m!n! \right)^{-1/2}$ = Normalization factor

$z_{\text{R}} = \frac{\pi\omega_0^2}{\lambda}$ = Rayleigh range

H_m = Hermite polynomial of order m

1 Self-similar here means that the mode content of a beam in HG or LG description does not change due to diffraction.

2 There is a second basis of LG modes. These helical LG modes are presented in [FS10].

$$a(x) = \frac{x}{\omega_0} \left(\frac{2}{1 + \left(\frac{z}{z_R}\right)} \right)$$

$$\phi_{\text{gouy}, m, n}(z) = i(m + n + 1) \arctan \left(\frac{z}{z_R} \right) = \text{Gouy phase shift}$$

$$\omega_0 = \text{Size of the beam waist}$$

$$e_{m, n} = \phi_{\text{gouy}, m, n}(z) - \frac{x^2 + y^2}{\omega_0^2 \left(1 - i \frac{z}{z_R}\right)}$$

$$N_{p, l}^{\text{LG}} = \left(\pi \omega_0^2 \frac{(p + l)!}{2p!} \right)^{-1/2} = \text{Normalization factor}$$

$$L_p^{(l)} = \text{Laguerre polynomial of order } p, l$$

$$e_{p, l} = \pm i l \phi + \phi_{\text{gouy}, p, l}(z)$$

$$\phi_{\text{gouy}, p, l}(z) = i(2p + |l| + 1) \arctan \left(\frac{z}{z_R} \right) = \text{Gouy phase shift}$$

Any beam can then be described as a superposition of these modes with different amplitude coefficients $A_{m, n}$ or $A_{p, l}$ as in eq. 3.2

$$E = \sum_{m=0}^{\infty} \sum_{n=0}^{\infty} A_{m, n} \psi_{m, n}^{\text{HG}} \quad (3.2a)$$

$$E = \sum_{p=0}^{\infty} \sum_{l=-\infty}^{\infty} A_{p, l} \psi_{p, l}^{\text{LG}} \quad (3.2b)$$

The order of the HOMs is described via two coefficients, m, n for HG modes and p, l for LG modes, with m and n describing the intensity distribution in Cartesian coordinates along two axes perpendicular to the optical axis and l and p describing the intensity distribution in polar coordinates with the beam axis in the origin. Here p describes the radial dependence and l describes the azimuthal dependence¹. The intensity distributions of several HOMs are shown in fig. 3.1.

The amplitude coefficients $A_{m, n}$ and $A_{p, l}$ are dependent on the chosen axis used to describe the beam propagation. E.g. a beam consisting of purely the fundamental mode described in a propagation axis tilted with regard to the optical axis appears as a superposition of fundamental and HG_{01/10} modes. A change of beam direction can in turn be described via addition of HG_{01/10} modes while keeping the axis used to describe the beam propagation constant.

¹ Note that in the literature the ordering of these indices as well as their actual meanings may be interchanged.

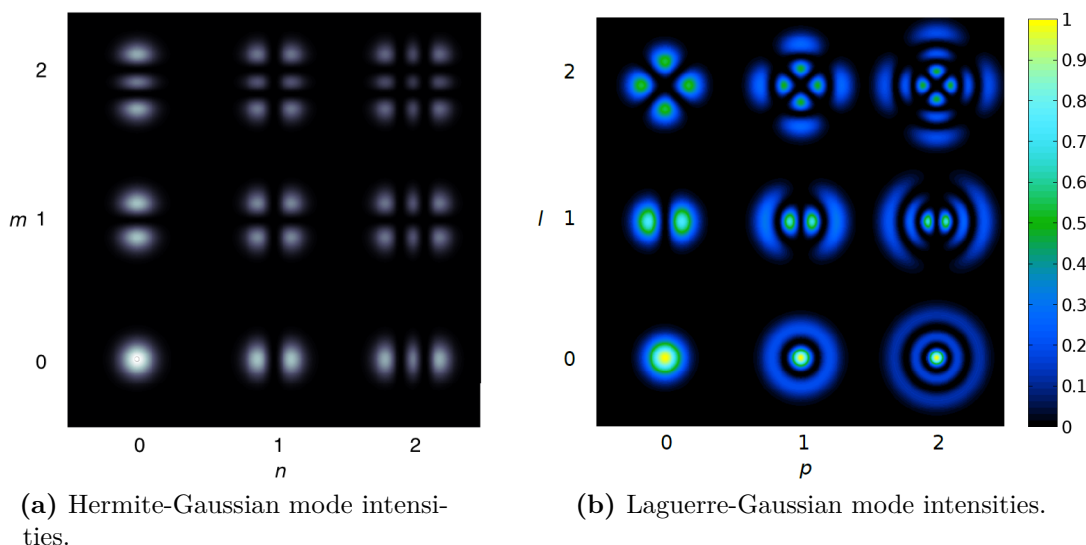


Figure 3.1: Power distribution of different optical modes [FS10].

3.2 The M^2 beam quality parameter

A commonly used, albeit somewhat limited, figure of merit for the modal quality of a laser beam is the M^2 parameter, defined as [Sie90]

$$M_{\text{HG}}^2 = \sum_{n=0}^{\infty} \sum_{m=0}^{\infty} (n + m + 1) |c_{nm}|^2 \quad (3.3a)$$

$$M_{\text{LG}}^2 = \sum_{p=0}^{\infty} \sum_{l=-p}^p (2p + l + 1) |c_{pl}|^2 \quad (3.3b)$$

with

$$M_{\text{HG}} = M^2 \text{ as defined for Hermite-Gaussian mode contributions.}$$

$$M_{\text{LG}} = M^2 \text{ as defined for Laguerre-Gaussian mode contributions.}$$

$$|c_{nm}|^2, |c_{pl}|^2 = \text{Power in the respective mode.}$$

As is evident from the definition in eq. 3.3 a beam purely in the fundamental mode has a M^2 value of 1. The physical relevance of this parameter is that the beam size of beams with otherwise identical parameters but different M^2 values will differ by the factor of the M^2 values. E.g. a beam with $M^2 > 1$ will have spot sizes bigger by a factor M^2 than a beam with $M^2 = 1$ everywhere along the beam axis.

As a frame of reference note that continuous-wave laser systems, for which a good beam

quality was a design goal, typically reach values of $M^2 < 1.1$ [WSW⁺08], with more than 96% of their output power in the fundamental mode [KSW⁺07].

3.3 Functional principle of an optical resonator

An optical mode is resonant in an optical resonator if the phase ϕ_{rt} it accumulates during one round-trip in the cavity fulfills the condition in eq. 3.4a. The fundamental mode of a beam can be separated from SBs and HOMs because their resonance conditions are usually not fulfilled at the same time. Because SBs are of a different frequency from the carrier light, they accumulate different amounts of phase during the round trip (see eqs. 3.4b and 3.4c). HOMs ($(m + n \neq 0)$ in HG description, $(2p + |l| \neq 0)$ in LG description) are resonant for different round-trip lengths compared to the fundamental mode because they accumulate different amounts of gouy phase (see eqs. 3.4d, 3.4e).

$$\phi_{\text{rt}} \stackrel{!}{=} n2\pi, n \in \mathbb{N} \quad (3.4a)$$

$$\phi_{\text{rt}} = \phi_{\text{propagation}} + \phi_{\text{gouy}} \quad (3.4b)$$

$$\phi_{\text{propagation}} = \frac{l_{\text{rt}}}{\lambda} 2\pi = \frac{l_{\text{rt}}}{c} f 2\pi \quad (3.4c)$$

$$\phi_{\text{gouy}} = (m + n + 1) \arctan\left(\frac{z}{z_R}\right) \text{ in HG description [Sie86]} \quad (3.4d)$$

$$\phi_{\text{gouy}} = (2p + l + 1) \arctan\left(\frac{z}{z_R}\right) \text{ in LG description [Sie86]} \quad (3.4e)$$

3.4 Parameters of optical resonators

In this section we reproduce some important equations describing the properties of optical resonators for later reference. These equations originate mainly from [Sie86].

3.4.1 Free spectral range

As seen in eq. 3.4a the resonance condition for individual mode repeats indefinitely. The *free spectral range* (FSR) is the distance, in frequency, between these repetitions.

$$\text{FSR} = \frac{c}{2l}, [\text{FSR}] = \text{Hz} \quad (3.5)$$

with

$$l = \text{Optical round-trip length inside the cavity.}$$

A longer cavity therefore has a smaller FSR than a shorter one.

3.4.2 Finesse

The finesse of a cavity is the ratio between the width of the resonance, measured as *full width at half maximum* (FWHM), and the FSR of said cavity.

$$F = \frac{\text{FSR}}{\delta f}, [F] = 1 \quad (3.6a)$$

$$= \frac{\pi\sqrt{g_{\text{rt}}}}{1 - g_{\text{rt}}} \quad (3.6b)$$

with

g_{rt} = Round-trip gain / loss

δf = FWHM bandwidth of the resonance

The resonant enhancement of power in the cavity depends on the finesse as

$$\frac{P_{\text{Intra-cavity}}}{P_{\text{Input}}} = \frac{F}{\pi} \quad (3.7)$$

As eq. 3.6b shows, a cavity needs to have low losses ($g_{\text{rt}} \approx 1$) to have a high finesse.

The reason to choose a high finesse for a cavity is typically to give it a small bandwidth while keeping it reasonably short. The smaller the bandwidth of a cavity the more powerful a tool it is to analyze a beam or to filter its contents. Such a high finesse cavity however is challenging to control. Firstly, due to the small bandwidth the control systems need to control the cavity's length very accurately. Secondly, a high finesse leads to a strong resonant enhancement of the intra-cavity power, as shown in eq. 3.7. This leads to a strong radiation pressure exerted on the cavity's mirrors when the cavity is in lock. During lock acquisition the radiation pressure quickly builds up and needs to be compensated by the control systems.

3.4.3 G factor

In our deliberations of optical resonators we so far omitted the curvature of the phase fronts of the light circulating in the resonators. A requirement for the stability of a cavity is that the beam size does not extend beyond all bounds while it circulates in the cavity. The g factor can be used to ascertain the stability of a cavity. The g factor for two mirror cavities is defined as

$$g = g_1 g_2 \quad (3.8a)$$

$$g_i = 1 - \frac{l}{R_i} \quad (3.8b)$$

with

$R_i =$ Radius of curvature of mirror i

The range of stable g factors is $0 \leq g \leq 1$ with corresponding configurations depicted in fig. 3.2.

An important aspect of the g factor is that it defines the resonance condition of HOMs relative to the fundamental mode by defining the shape of the beam circulating inside the cavity. This was already implicitly stated in eqs. 3.4d,3.4e. Explicitly, the resonance frequency of HOMs with respect to fundamental mode's frequency is defined as

$$\omega_{q,n,m} = \left[q + (n + m + 1) \frac{\arccos(\pm\sqrt{g})}{\pi} \right] \cdot \text{FSR} \quad (3.9)$$

with

$$\begin{aligned} q &\in \mathbb{N} \\ n, m &= \text{Mode order in HG representation} \\ \arccos(\pm\sqrt{g}) &= \arccos(+\sqrt{g}) \text{ for } g_1 > 0 \text{ and } g_2 > 0 \\ \arccos(\pm\sqrt{g}) &= \arccos(-\sqrt{g}) \text{ for } g_1 < 0 \text{ and } g_2 < 0 \end{aligned}$$

When we want to use a cavity to filter out HOMs, it is therefore important to choose a g factor that does not lead to a coincident resonance of HOMs and the fundamental mode.

3.4.4 Impedance matching

One can accomplish a high transmission of a beam component through an optical resonator only if said beam component is resonant in the resonator and the resonator is impedance matched for the beam component. Impedance matching means that the reflectivity of the input mirror and output mirror are equal. Losses in the cavity are treated as reductions in the reflectivity of the output coupler mirror [RCG⁺10]. With this we can calculate the reflectivity of the cavity presented in fig. 3.3 as

$$R = \frac{E_{\text{refl}}^2}{E_{\text{inc}}^2} = \left(\frac{r_1 r_2 (t_1^2 + r_1^2)}{1 - r_1 r_2} \right)^2 \quad (3.10)$$

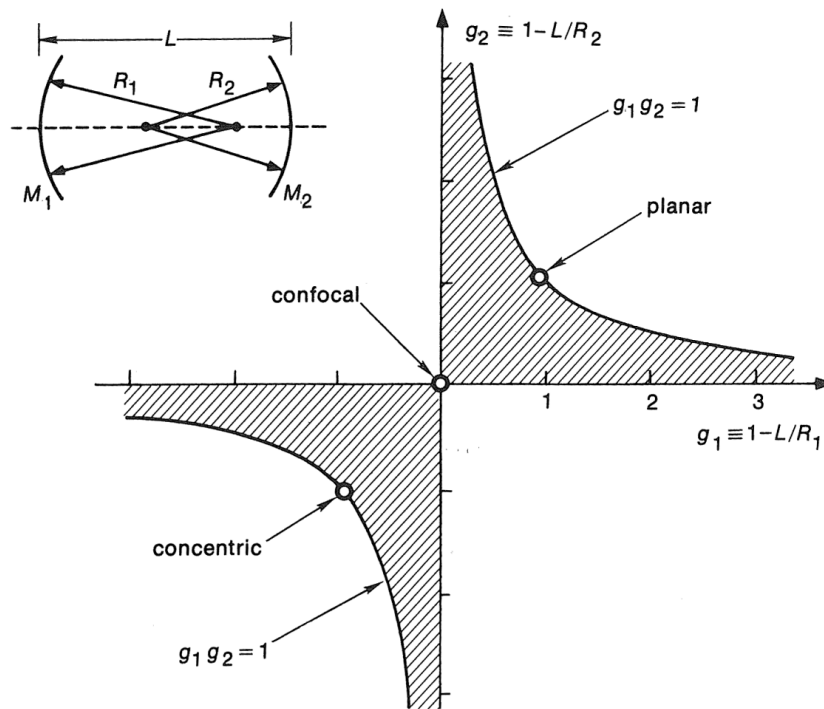


Figure 3.2: G factors of different resonator configurations. The stable area is striped [Sie86].

with

R = Reflectivity (in power) of the cavity

r_1 = Reflectivity (in amplitude) of the input mirror

r_2 = Reflectivity (in amplitude) of the output mirror.

Losses in the cavity reduce this value.

t_1 = Transmittance (in amplitude) of the input coupler mirror

$= \sqrt{1 - r_1^2}$ = For low loss mirror

$R_i = r_i^2$

$T_i = t_i^2$

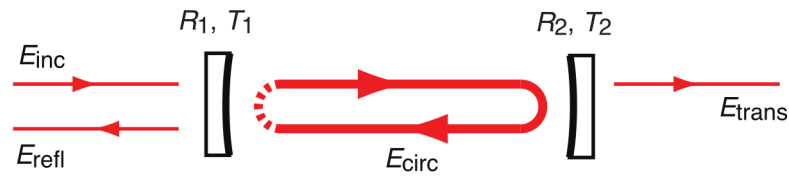


Figure 3.3: A resonant two-mirror cavity [RCG⁺10].

In fig. 3.4 we show the reflectivity of a cavity for three different impedance matching regimes:

- **Under coupled:** ($r_1 > r_2$)
- **Impedance matched:** ($r_1 = r_2$)
- **Over coupled:** ($r_1 < r_2$)

Note the sharp drop in reflectivity (to 0) of the cavity for the case of impedance matching.

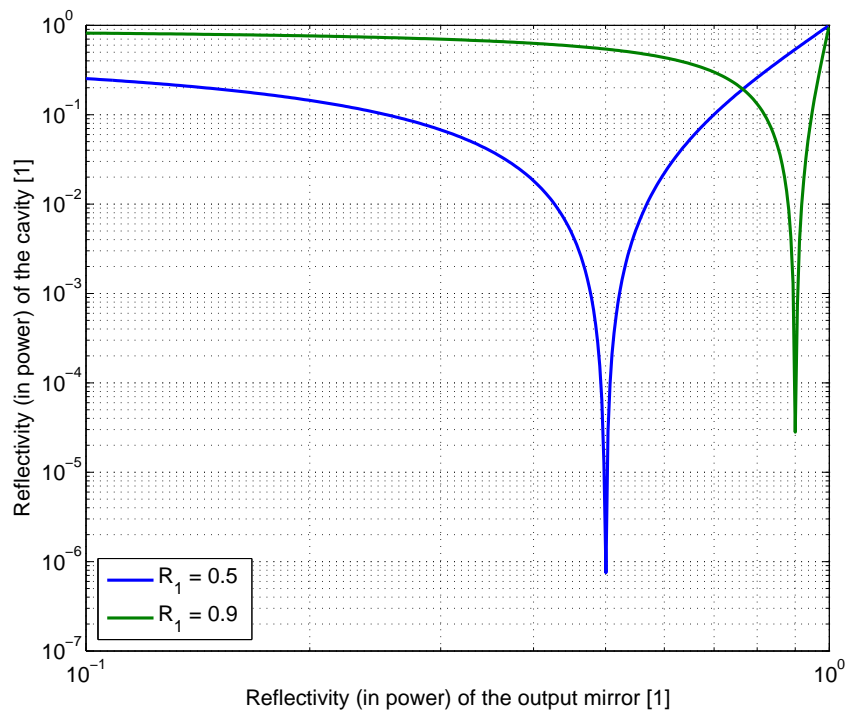


Figure 3.4: Reflectivity of a cavity in different impedance matching regimes, for two different input coupler reflectivities R_1 . In the case of impedance matching the reflectivity drops to 0.

3.5 Mode-conversion when coupling into an optical resonator

Coupling a beam into an optical resonator, or optical cavity, creates couplings between different modes. These couplings depend on 6 parameters, two of which describe tilts between the propagation axis of the incoming beam and the eigenmode of the resonator, two describe translations between the incoming beam and the eigenmode, and another two describe the mode-matching between incoming beam and resonator eigenmode [And84, MMR⁺94]. It is instructive to consider pure misalignments in one dimension for an input beam consisting only of light in the fundamental mode. Quantities related to the incoming beam are marked by a (0) , and quantities related to the resonator eigenmode are marked by a $(\bar{})$. We will describe misalignments by their effect at the beam waist $z = 0$. First we look at a translation of the incoming beam in $-x$ direction by dx in eq. 3.11.

$$\left(\psi_{m=0}^{\text{HG}}(x)\right)^{(0)} \propto \exp\left(-\frac{(x+dx)^2}{\bar{\omega}_0^2}\right) = A_1 \exp\left(-\frac{(x+dx)^2}{\bar{\omega}_0^2}\right) \quad (3.11a)$$

$$\stackrel{dx \approx 0}{\approx} A_1 \left(1 + 2dx \frac{x}{\bar{\omega}_0}\right) \exp\left(-\left(\frac{x}{\bar{\omega}_0}\right)^2\right) \quad (3.11b)$$

$$= A_1 \left(\overline{\psi_{m=0}^{\text{HG}}(x)} + \frac{dx}{\bar{\omega}_0} \overline{\psi_{m=1}^{\text{HG}}(x)}\right) \quad (3.11c)$$

Now we consider a tilt of the incoming beam by α_x around the y -axis.

$$\left(\psi_{m=0}^{\text{HG}}(x)\right)^{(0)} \propto \exp\left(-\frac{x^2}{\bar{\omega}_0^2} + i\alpha_x x\right) = A_2 \exp\left(-\frac{x^2}{\bar{\omega}_0^2} + i\alpha_x x\right) \quad (3.12a)$$

$$\stackrel{\alpha_x \approx 0}{\approx} A_2 \left(\overline{\psi_{m=0}^{\text{HG}}(x)} + i\sqrt{\pi\bar{\omega}_0}\alpha_x \overline{\psi_{m=1}^{\text{HG}}(x)}\right) \quad (3.12b)$$

With this we see that misalignments create mode-conversions from $\text{HG}_{00}^{(0)}$ to $\overline{\text{HG}_{01/10}}$.

If we allow for mode-mismatch and HOM content in the input beam as well as misalignments, the mode-conversion coefficients k presented in eq. 3.13 become considerably more

complex [BH84]. The coefficients $k_{m,n,\bar{m},\bar{n}}$ can be split into $k_{m,n,\bar{m},\bar{n}} = k_{m,\bar{m}} \cdot k_{n,\bar{n}}$.

$$k_{m^{(0)}=0,\bar{m}=0} = E^{(x)}(1 + K_0)^{1/4}(1 + K^*)^{-1/4} \quad (3.13a)$$

$$k_{m^{(0)}=1,\bar{m}=0} = E^{(x)}(1 + K_0)^{3/4}(1 + K^*)^{-1}\bar{X} \quad (3.13b)$$

$$k_{m^{(0)}=0,\bar{m}=1} = -E^{(x)}(1 + K_0)^{1/4}(1 + K^*)^{-1}\bar{X} \quad (3.13c)$$

$$k_{m^{(0)}=2,\bar{m}=0} = E^{(x)}2^{-1/2}(1 + K_0)^{5/4}(1 + K^*)^{-3/2}(\bar{X}^2 - 2\bar{F}) \quad (3.13d)$$

$$k_{m^{(0)}=1,\bar{m}=1} = -E^{(x)}(1 + K_0)^{3/4}(1 + K^*)^{-3/2}(\bar{X}X - 1) \quad (3.13e)$$

$$k_{m^{(0)}=0,\bar{m}=2} = E^{(x)}2^{-1/2}(1 + K_0)^{1/4}(1 + K^*)^{-3/2}(\bar{X}^2 + 2\bar{F}) \quad (3.13f)$$

with

$$E^{(x)} = \exp\left(-\frac{\bar{X}X}{2} - i\frac{x^{(0)}}{\omega_0} \frac{\gamma}{\gamma_0}\right)$$

$$\bar{X} = (1 + K^*) \frac{dx}{\omega_0} - \left(\frac{\bar{z}_2}{z_0} - i\right) \frac{\gamma}{\gamma_0}$$

$$X = (1 + K^*) \frac{dx}{\omega_0} - \left(\frac{\bar{z}_2}{z_0} + i(1 + 2K^*)\right) \frac{\gamma}{\gamma_0}$$

$$dx =$$

= Shift of the input beam in the -x direction

$$\bar{F} = \frac{K}{2(1 + K_0)}$$

$$\gamma =$$

= Tilt of the incoming beam about the $-y$ axis

$$\gamma_0 = \omega_0/\bar{z}_0$$

= Beam divergence angle

$$\bar{\omega}_0 =$$

= Waist size, eigenmode

$$K = (K_0 + iK_2)/2$$

= Mode-matching parameter

$$K_0 = (z_0^{(0)} - \bar{z}_0)/\bar{z}_0$$

= Waist size mismatch

$$z_0^{(0)} =$$

= Rayleigh range, incoming beam

$$\bar{z}_0 =$$

= Rayleigh range, eigenmode

$$K_2 = (z^{(0)} - \bar{z}/\bar{z})$$

= Waist position mismatch

$$z_2^{(0)} =$$

= Waist position, incoming beam

$$\bar{z}_2 =$$

= Waist position, eigenmode

4 GEO 600 signal-recycling configurations

Signal-recycling is generally a technique associated with second generation GW detectors, with GEO 600 being the only first generation GW detector employing it. Signal-recycling creates a resonance in the interferometer to signals generated by differential arm length motion, as caused by GWs, by creating a cavity for such signals. This cavity is created by placing the so-called signal-recycling mirror into the output beam of the interferometer. The cavity is formed by the mirrors MSR, MCE, and MCN depicted in fig. 1.6. The properties of this cavity and therefore the resonance have to be optimized to realize the maximum benefit from signal-recycling.

The GEO 600 interferometer is dual-recycled in that it employs power-recycling and signal-recycling. This technique was first demonstrated in 1991 [SM91, HSM⁺98]. As described in section 4.2 the relative properties of the power-recycling and signal-recycling cavities have a great influence on the mode content of the interferometer's output beam.

4.1 Shot noise limited sensitivities for different signal-recycling configurations

In the original GEO 600 setup the signal-recycling resonance was detuned from DC, or 0 Hz, to a frequency of 550 Hz. As part of the GEO-HF upgrade the tuning was changed to DC in June 2010 which allows for the direct implementation of squeezing without a compensating cavity [Kha11]. In conjunction with the change of the readout method from heterodyne to DC / homodyne, this offered a considerable benefit in shot noise limited sensitivity. In this configuration the maximum benefit to shot noise limited sensitivity is at low frequencies where the noise is dominated by technical noise sources and benefits from reduced shot noise can not be realized. To improve on this situation, we exchanged the signal-recycling mirror in November 2010 for one with a lower reflectivity of 90 % rather than 98 % used before. This increased the signal-recycling cavity's bandwidth, measured as *half width at half maximum* (HWHM), from approximately 220 Hz to approximately 1100 Hz and improved the shot noise limited sensitivity above 430 Hz as depicted in fig. 4.1.

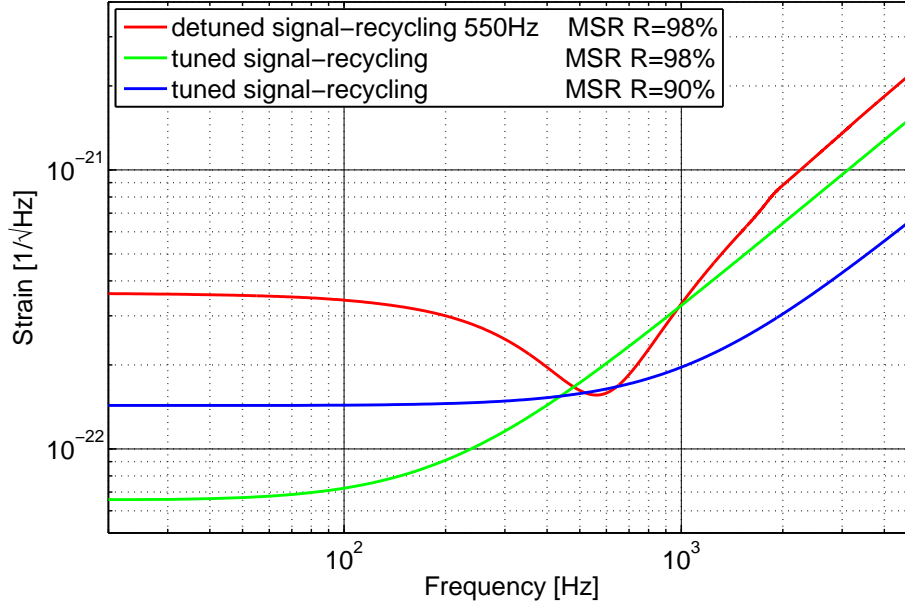


Figure 4.1: Calculated shot noise limited sensitivities of GEO 600 for different signal-recycling configurations.

4.2 Dependence of higher order optical mode generation on the signal-recycling configuration

The considerable amounts of HOMs present in the output beam of GEO 600's interferometer are generated inside the interferometer. The upgraded laser system of GEO 600 emits 96 % of its power in the fundamental mode [KSW⁺07]. The IMCs are expected to further clean the mode content of said beam. The interferometer's input beam therefore only contains negligible amounts of HOMs, while its output beam contains considerable amounts of HOMs. When we, for a moment, neglect the signal-recycling aspect of the interferometer's dual-recycling, then the coupling of a beam into the interferometer is synonymous to coupling it into the PRC. In this there are several conceivable mechanisms that could generate HOMs inside the interferometer:

- **Mode-conversion due to errors in alignment and / or mode-matching:** As described in section 3.5, even a beam consisting of only the fundamental mode can be partially converted to HOMs when coupled into a cavity due to errors in alignment and / or mode-matching. Imperfect coupling of the input beam into the PRC could therefore generate HOMs in the PRC.

The PRC contains an additional DOF over a simple cavity due to the fact that it contains an interferometer. The resonance condition of the Michelson interferometer

is an additional DOF to be considered. GEO 600's operating point is at or near the dark-fringe, meaning that almost the entire fundamental mode carrier light is reflected towards the power-recycling mirror. Due to the Schnupp asymmetry described in chapter 2 this is not necessarily also true for HOMs. We can calculate the suppression of these HOMs based on eqs. 3.4d,3.4e as

$$\Delta\phi = |\phi_1 - \phi_2| = (m + n) \arctan\left(\frac{|z_1 - z_2|}{z_R}\right) \quad (4.1a)$$

$$\approx (m + n) \arctan\left(\frac{0.069}{300}\right) \quad (4.1b)$$

$$\approx (m + n) 2.3 \cdot 10^{-4} \quad (4.1c)$$

with

$\Delta\phi =$ Difference of phase accumulated in the two interferometer arms.

$z_i =$ Length of the i -th interferometer arm.

which leads to an extinction ratio K of these HOMs of

$$K \approx \frac{1}{(m + n) 2.3 \cdot 10^{-4}} = \frac{4300}{(m + n)} \quad (4.2)$$

when the interferometer is perfectly at the dark-fringe for the fundamental mode carrier light. Because the mode content of the 3 kW light power circulating in the PRC is dominated by the fundamental mode, as visible in fig. 4.2, and the mode content in the interferometer's output beam does not follow a $1/(m + n)$ behavior, as seen in figs. 5.35,5.42, we can rule out mode-conversion as a source for HOMs in the output beam.

- **Mode-conversions due to arm asymmetries:** Asymmetries in the arms cause imperfect extinction of the arms' beams at the beam splitter. The residuals of this imperfect extinction are HOMs.

Conceivable causes of such asymmetries are:

- **Thermal lensing in the beam splitter:** Because the beam to the east arm is transmitted through the beam splitter, whereas the beam to the north arm is reflected at the beam splitter's surface, thermal lensing in the beam splitter is asymmetric in the arms. In the future we will compensate this asymmetry using a TCS (see also chapter 2,[Wit11]).
- **Asymmetric ROCs of the arms' mirrors:** The ROCs of the mirrors in the arms are not identical due to imperfect manufacturing. This is partially compensated using a heater element behind the MFE mirror with which we can dynamically adjust that mirror's ROC [Gro03]. The effect of asymmetric



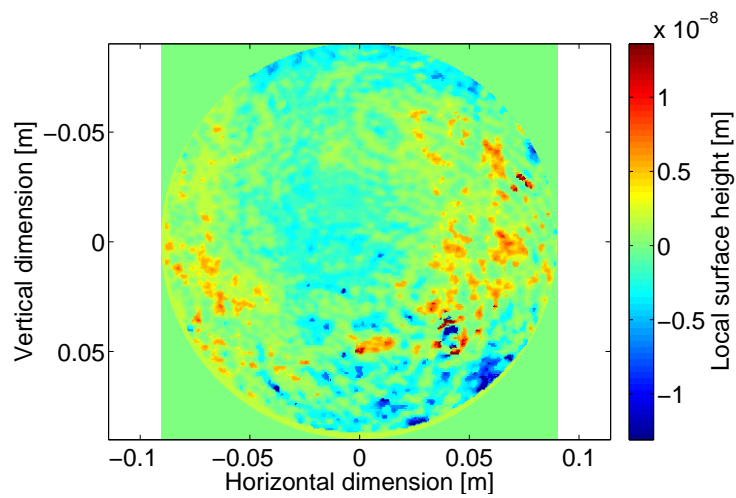
Figure 4.2: Picture of the beam circulating in the interferometer, as seen in transmission of MFE. The horizontal fringes are interference patterns caused by the fact the MCE and MCN are hanging higher than MFE, MFN and the beam splitter.

ROCs of the arms' mirrors on the HOM content of the interferometer's output beam is shown in subsection 5.5.2.

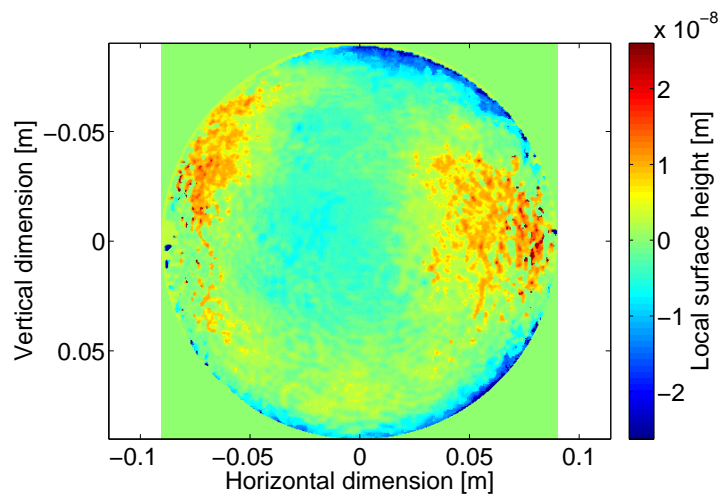
- **Asymmetric defects in the mirrors' surfaces:** Aside from asymmetries in the overall ROC of the mirrors, there can also be asymmetries in the local mirrors' surface heights. Manufacturer provided data on such mirror defects of three of GEO 600's main optics is presented in fig. 4.3. Preliminary simulations regarding the effects of these defects were carried out using the OSCAR optical FFT software [Deg10, Deg12]. We assumed the interferometer to be exactly at the dark-fringe for the fundamental mode carrier light. The simulated interferometer contained a signal-recycling mirror with a power reflectivity of 98%. In table 4.1 we present the effect that these mirror defects have on the properties of GEO 600. In fig. 4.4 we display the intensity distributions of the output beams.

Because these HOMs are generated at the beam splitter they are not subject to the same extinction as the HOMs generated by errors in alignment and / or mode-matching.

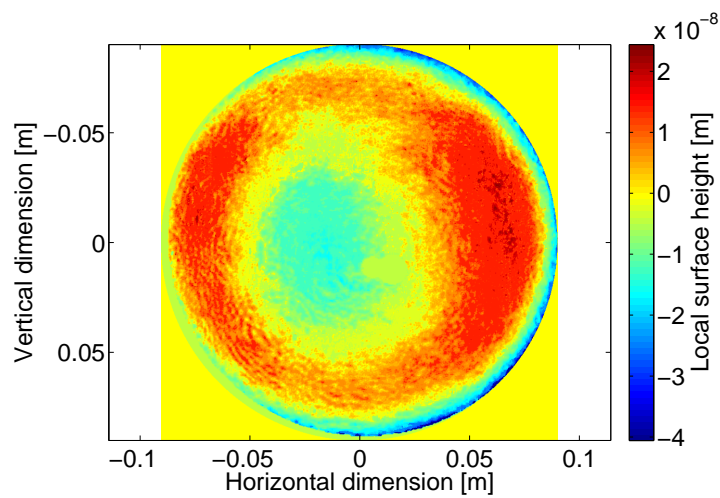
HOMs generated at the beam splitter, due to asymmetries, can be emitted towards the input port and power-recycling mirror, or towards the output port and signal-recycling mirror. Ignoring the signal-recycling, the direction into which the HOMs are emitted



(a) The MCN mirror's HR surface.

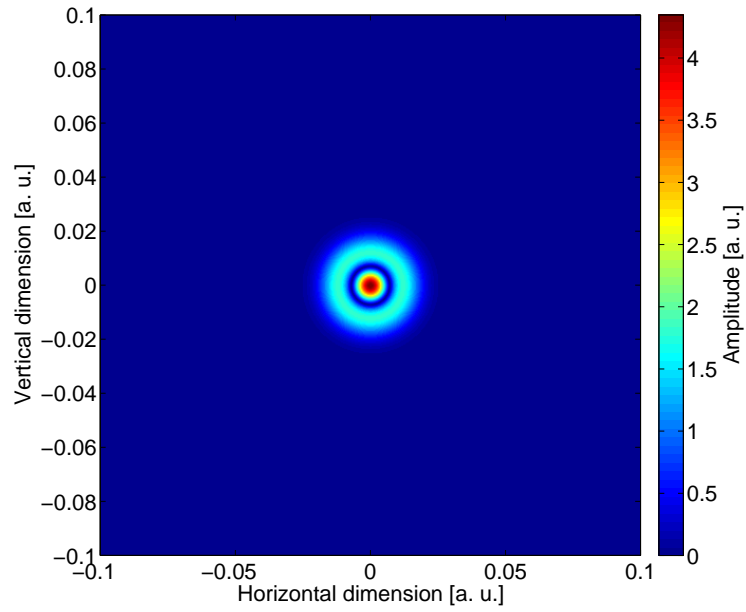


(b) The MFE mirror's HR surface.

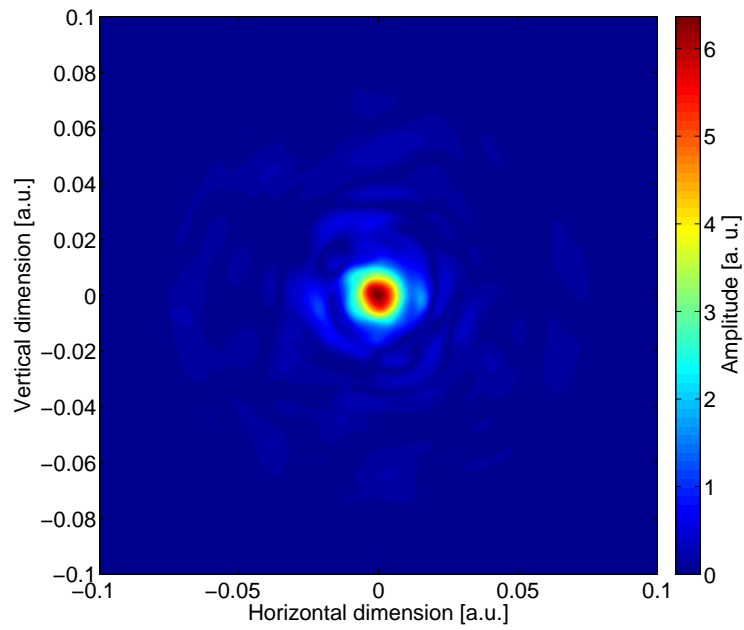


(c) The MFN mirror's HR surface.

Figure 4.3: Local mirror surface heights of some of GEO 600's main optics as indicated by the manufacturer. Overall ROC removed.



(a) Perfect mirrors.



(b) Realistic mirrors.

Figure 4.4: Absolute amplitude distribution of the interferometer's output beam for different mirror qualities and a signal-recycling mirror reflectivity of 98%.

Table 4.1: Simulated effects of local mirror defects. Simulated defects similar to those displayed in fig. 4.3. The interferometer was set to the dark fringe with regard to the fundamental mode carrier light. The reflectivity of the signal-recycling mirror was 98 %. The measured value for the resonant enhancement of power in the PRC is approximately 1000.

Configuration	Resonant enhancement	Output power [mW]
Perfect mirrors	2772	22
Realistic mirrors	1589	21

depends entirely on the resonance of the HOMs in the PRC. If the HOMs are resonant in the PRC, they are emitted towards the power-recycling mirror, and no HOMs are emitted towards the output port. HOMs that would be emitted towards the output port are annihilated by the HOMs being reflected at the power-recycling mirror. In this configuration power-recycling reduces the amount of HOMs in the output beam when compared to a configuration without power-recycling, because the HOMs that are reflected back into the interferometer get partially converted back to the fundamental mode. This effect is known as mode-healing.

4.2.1 Mode-healing due to signal-recycling

When the HOMs are not resonant in the PRC they are emitted towards the interferometer's output port and signal-recycling mirror. The beam splitter is the input through which the HOMs enter the signal-recycling cavity. In this case the reflectivity of the signal-recycling cavity for these HOMs influences the extent of the mode-healing effect. High reflectivity increases the amount of HOMs circulating in the PRC leading to more mode-healing.

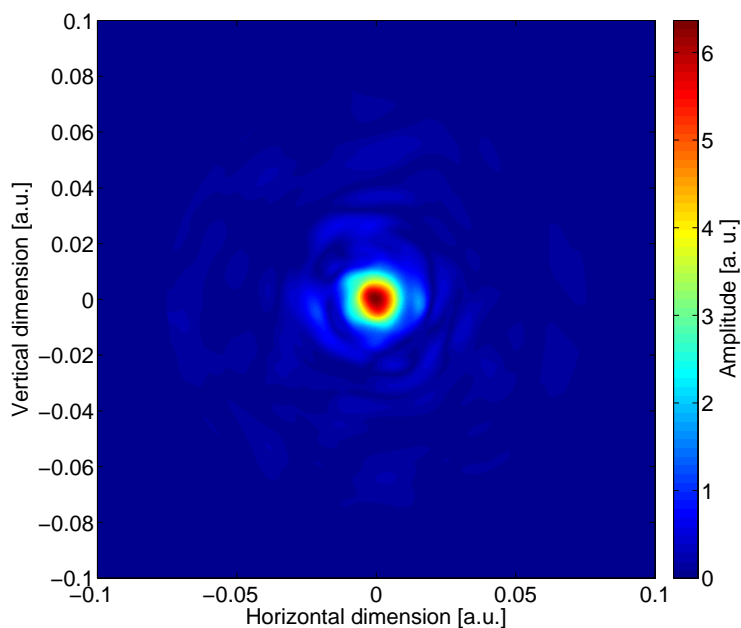
The reflectivity of the SRC for HOMs is determined by the HOMs' fulfillment of the SRC's resonance condition, and the impedance matching between HOMs and SRC (see sections 3.3, 3.4.4). Let us first assume perfect impedance matching. When the HOMs are resonant in the SRC, then the HOMs are resonantly enhanced in the SRC and exit the interferometer through the signal-recycling mirror. When they are not resonant, then the SRC reflects the HOMs back into the PRC and additional mode-healing occurs. Let us now consider the actual impedance matching. Section 5.5 shows us that the reduction of the signal-recycling mirror's reflectivity from 98 % to 90 % reduces the mode-healing effect. This means that the reflectivity of the SRC for HOMs is reduced, and the SRC is closer to impedance matching for the HOMs than before. This also means that the SRC was over coupled for HOMs before the signal-recycling mirror exchange.

Preliminary simulations regarding the dependence of the mode-healing effect on the signal-recycling mirror's reflectivity were performed for realistic MCN, MFE and MFN mirrors using a not yet published version of the OSCAR software. In table 4.2 we present the simulated effects that different signal-recycling mirror reflectivities have on

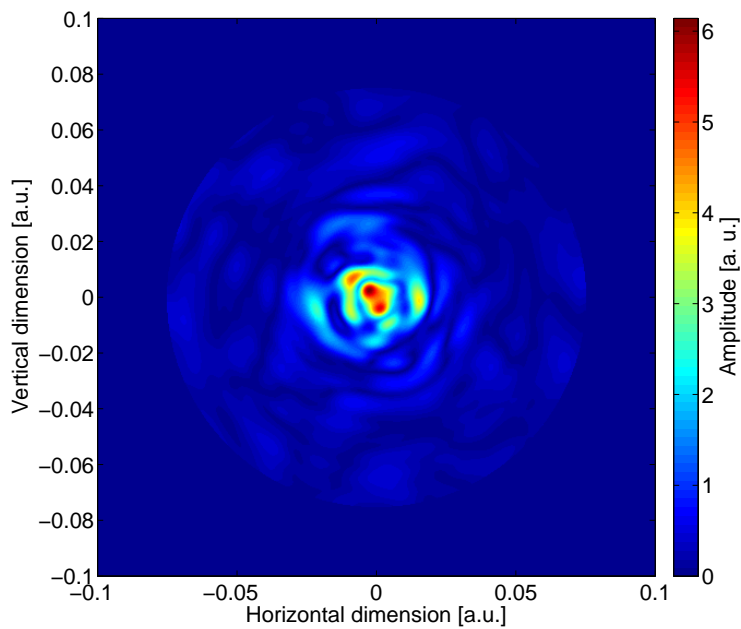
the properties of GEO 600. The simulated relative change in resonant enhancement due to the exchange of the signal-recycling mirror is -1.5% which is in good agreement with the measured change of -1.9%. In fig. 4.5 we display the power distributions of the output beams as dependent on the signal-recycling configuration.

Table 4.2: Simulated effects of different signal-recycling mirror reflectivities. Simulated defects similar to those displayed in fig. 4.3. The interferometer was set to the dark fringe with regard to the fundamental mode carrier light. The measured value for the resonant enhancement of power in the PRC is approximately 1000.

Configuration	Resonant enhancement	Output power [mW]
MSR R = 98%	1589	21
MSR R = 90%	1565	90



(a) Signal-recycling mirror's reflectivity: 98%.



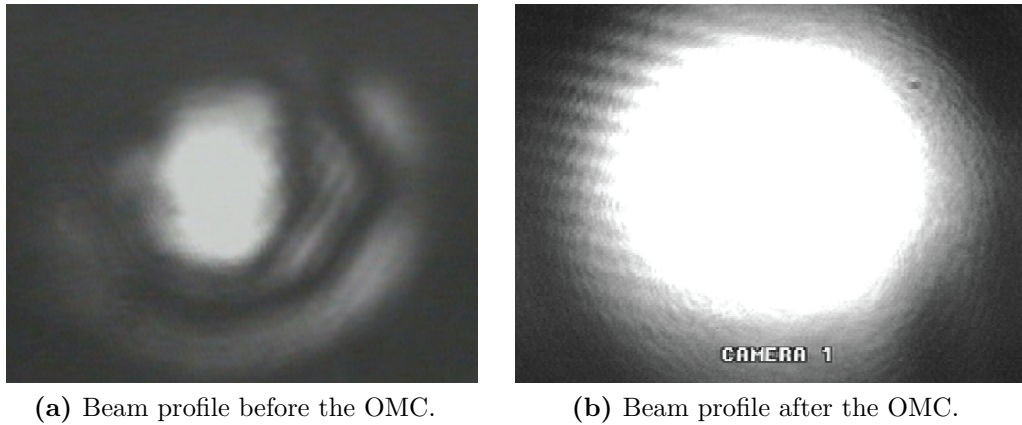
(b) Signal-recycling mirror's reflectivity: 90%.

Figure 4.5: Simulated absolute amplitude distribution in the interferometer's output beam for realistic mirrors and different signal-recycling configurations.

5 The output mode cleaner

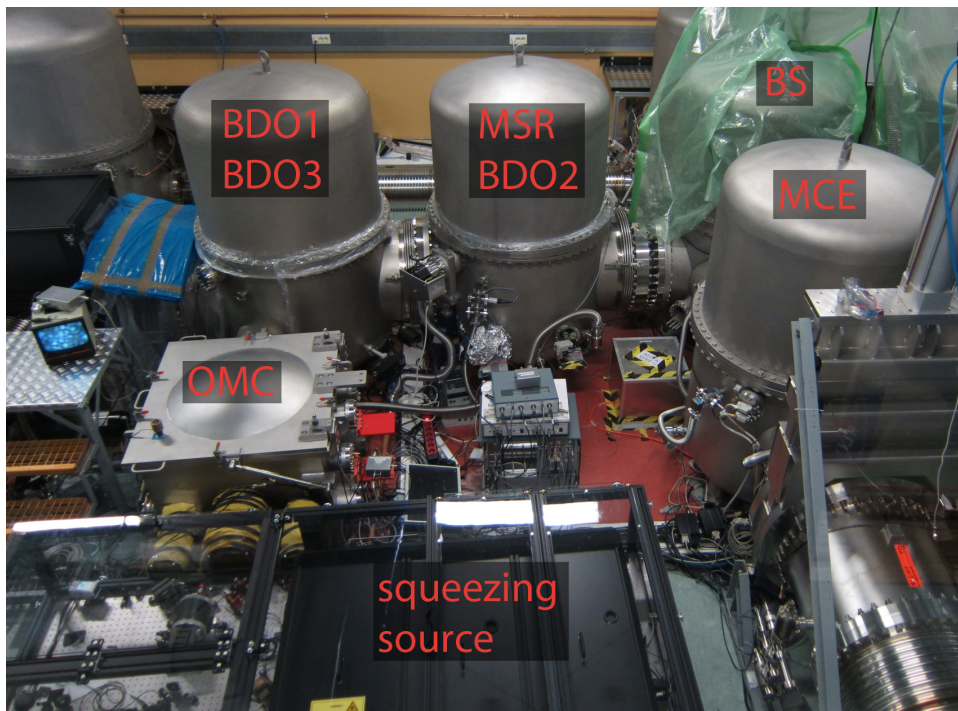
The *signal* a GW creates in a Michelson interferometer type GW detector can be influenced by adjusting the microscopic asymmetry of the interferometer's arm lengths, also called the *dark-fringe offset* (DFO). *Noise* sources in a GW detector can either be dependent or independent of the DFO. The *signal to noise ratio* (SNR) between the GW signal and the noise which is dependent on the DFO is better for a smaller DFO because several noise couplings amplify with increasing the DFO. A prime example is the coupling of laser amplitude noise. A small DFO is therefore desirable. The downward limiting factors for the DFO are noises that are independent of the DOF, such as shot noise generated by spurious output beam components that carry no extractable GW signal. Attenuation of these components therefore allows for a smaller DFO and a better overall sensitivity of GEO 600 to GWs.

The OMC is designed to strongly attenuate output beam components that do not contribute to the GW measurement. These consist of HOMs and control SBs. The HOMs are created by asymmetries between the interferometer's arms. The control SBs are imprinted onto the beam before it enters the interferometer and are used to control several of its *degrees of freedom* (DOFs) [Gro03]. Before the OMC these beam components constitute approximately 90 % of the beam power of approximately 50 mW. The OMC attenuates their power by a factor of at least 100, reducing their shot noise contributions by at least a factor 10. A comparison of the beam before and after the OMC is presented in fig. 5.1. The design of the OMC minimized the changes necessary to the pre-existing GEO 600 infrastructure. Fig. 1.6 and 5.2 show schematically and photographically the location of the OMC.



(a) Beam profile before the OMC.

(b) Beam profile after the OMC.

Figure 5.1: The interferometer's output beam profile before and after the OMC.**Figure 5.2:** The location of the OMC and surrounding optics. The labels identify, with the exception of the squeezing source, the optical components inside the vacuum tanks. **BDO:** Beam director output mirror, **MSR:** Signal-recycling mirror, **BS:** Beam splitter, **MCE:** Mirror in the east arm, close to the BS, **OMC:** Output mode cleaner.

5.1 Design of the output mode cleaner

The optical specifications for the OMC were derived by setting an upper limit for the shot noise contribution from spurious beam components of 1 % of the overall shot noise. Before the OMC these spurious components constitute approximately 90 % of the overall beam power, requiring their attenuation by a factor of 100. As such, two main specifications were derived:

1. The 14.9 MHz control sideband's power must be attenuated by at least a factor of 100 in power in transmission of the OMC. This requirement produces a lower limit on the bandwidth of the OMC optical cavity.
2. The higher order optical mode's power must also be attenuated by at least a factor of 100 in transmission. That requirement gives a lower limit on the cavity finesse and also restricts the choice of the possible g factor for the OMC.

The above specifications were taking into account that the GEO-HF upgrade program includes an increase in laser power from 15 W to 35 W [PGD⁺10].

To ensure that the OMC meets these specifications, simulation tools were developed based mainly on analytical formulas and ray-transfer matrix (ABCD-matrix) propagation laws. Then, the optimal parameters found were later checked with the Finesse software [FHL⁺04, Fre].

Based on simulations, it was decided that the OMC would consist of a four mirror cavity in a diamond shape as seen in fig. 5.3 and the dashed box in fig. 1.6. This particular configuration features several advantages. Firstly, it can be made compact in the direction of the beam, which suited the conditions at the GEO 600 site. Secondly, the center of mass of the structure is along the optical axis defined by the input and output beams. The equal distribution of mass on either side of the optical axis simplifies the seismic isolation. Thirdly, of the 4 mirrors of the cavity, 2 are used as input and output mirrors, the third is mounted on a *piezo-electric actuator* (PZT)¹ (Physik Instrumente S-303) for length control and finally the remaining mirror can be partially transparent and its transmission can be used to monitor the beam circulating in the OMC. And last but not least, using an even number of mirrors kept the resonance degeneracy between the transverse electro-magnetic modes of the same order $N = m + n$. So, when scanning through one FSR of the OMC modes of the same order N appear combined as a single transmission peak. This simplifies the identification of modes and reduces the risk of an unintended coincident resonance between HOMs and the fundamental mode carrier light.

The optical design parameters of the OMC are presented in table 5.1. This design allows for a small DFO of around 20 pm differentially, resulting in approximately 4 mW

¹ Even though the term PZT strictly speaking refers to Lead Zirconate Titanate ceramics, it is customary to refer to any piezo-electric actuator as a PZT.

of fundamental mode carrier light leaving the interferometer. For thermal stability, the OMC is entirely made of fused silica glass with optics and mounts glued with UV cured epoxy (Electronic Materials Inc. Optocast 3553-UTF-LV). A schematic view of the OMC is presented in fig. 5.3.

5.2 Building the output mode cleaner

The OMC was assembled at the class 1000 cleanroom facility at the Albert-Einstein-Institute. Two of the OMC mirror structures were constructed from three individual glass plates: a rectangular ground plate, a rectangular vertical plate and the round actual mirror. One mirror structure additionally contained the PZT used for length adjustment of the OMC. The mirror structures' elements were arranged with the help of machined templates and glued by putting a thin layer of vacuum compatible UV curable epoxy between them and then exposing them to an UV light source for approximately 60 seconds (see fig. 5.4). The positions of the mirror structures on the OMC baseplate was guided by another machined template. Three mirrors were placed at the positions defined by the template. We coupled a laser beam (generated by an Innolight Mephisto 500 NE) into the OMC, using two lenses for mode-matching, and checked the OMC output beam before bonding the flat output mirror. We found the structure displayed in fig. 5.5a in the OMC output beam and could attribute it to a tilt of the PZT mirror of approximately 10 mrad. We glued the spare PZT mirror structure and achieved a singular OMC output beam (see fig. 5.5b). In this configuration we glued the OMC mirrors.

After successfully constructing the OMC we experimented with locking it to the laser. Employing *control feedback* (FB) only to the PZT we were able to lock the OMC for approximately 90 seconds. Lock duration was limited by the actuation range of the PZT. By employing a split-path feedback to the OMC PZT and the thermal set-point of the laser we were able to keep the OMC locked for more than 90 minutes.

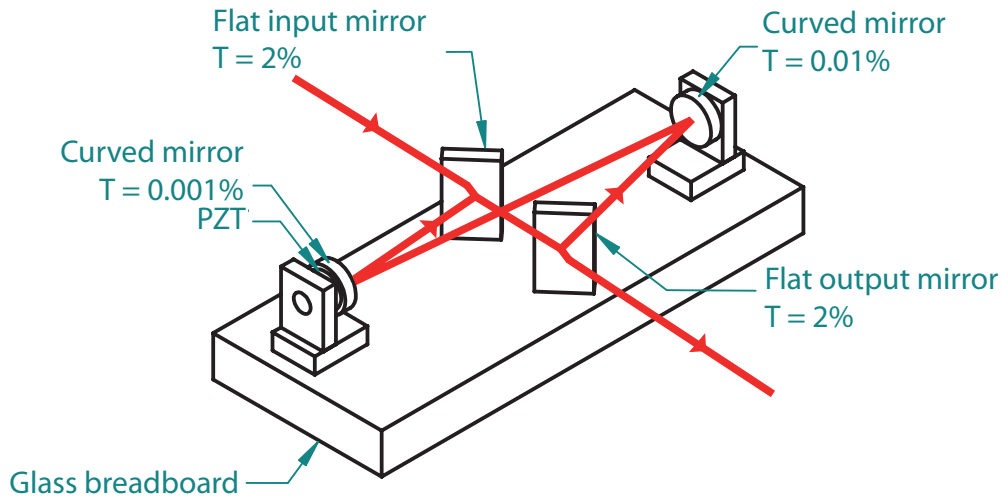


Figure 5.3: Schematic view of the GEO 600 OMC. All parts are made of fused silica except for the PZT. The glass breadboard is 400 mm by 160 mm and 38 mm thick (modified from [DGP⁺10]).

Table 5.1: Optical design parameters of the OMC.

Property	Design value
FSR	456 MHz
Finesse	155
Bandwidth (FWHM)	2.9 MHz
g factor	0.73
Round trip length	66 cm
Waist size	440 μm

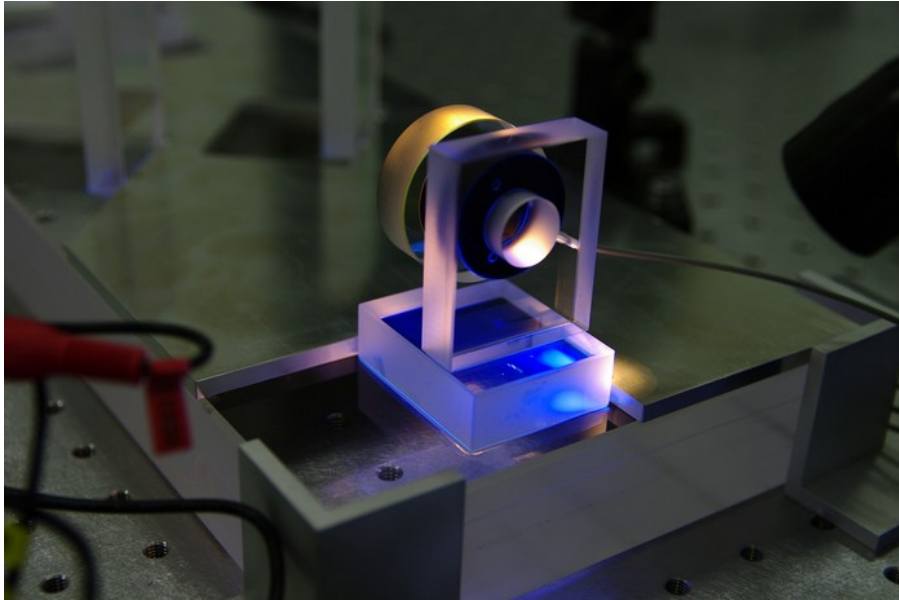
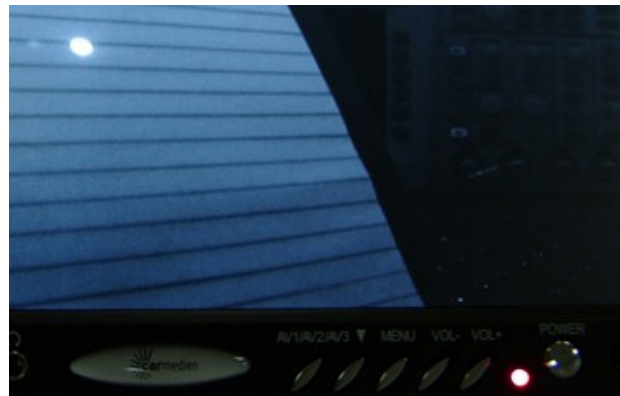


Figure 5.4: UV light curing of the epoxy layer between the PZT mirror structure and the OMC baseplate. The PZT mirror's position is defined by the machined metallic template. The UV light source can be seen on the right hand side.



(a) Tilted PZT mirror.



(b) Non-tilted PZT mirror.

Figure 5.5: Beam in transmission of the OMC for tilted and non-tilted PZT mirror. Detected via an IR-sensitive CCD on a screen.

5.3 Control system requirements and schemes

The addition of an OMC introduces several noise sources to GEO 600. Mainly these are fluctuations in the transmittance of the OMC due to fluctuations in the relative frequency offset Δf between interferometer's output beam and OMC resonance frequency, and also fluctuations in alignment onto the OMC. These noise sources can be mitigated by control systems. In the following sections we formulate requirements on these control systems which ensure that the new noise sources stay below shot noise in GEO 600's measurement frequency band.

5.3.1 Longitudinal control requirements

The transmittance of the OMC for the fundamental mode carrier light in the GEO 600 output beam is dependent on the frequency offset Δf between the GEO 600 carrier light frequency f_{laser} and the OMC resonance frequency f_{OMC} . The OMC transmittance shows a $1/|\Delta f|^2$ dependence for small Δf (see fig. 5.7). Fluctuations Δf_{audio} in Δf at frequencies in the GEO 600 measurement band create noise in the GW measurement. The size of this noise source depends on the *root mean square* (RMS) value of Δf . Below we estimate the size of Δf_{audio} and formulate requirements on control systems that confine the RMS value of Δf so that the noise due to Δf_{audio} stays below 1/10 shot noise.

The RMS value of Δf is dominated by low frequency fluctuations Δf_{LF} of the GEO 600 laser light frequency f_{laser} at frequencies around 1 Hz. The frequency of the GEO 600 laser is locked to the PRC formed by the mirrors MPR, MCE, and MCN [WAA⁺02]. These mirrors are seismically isolated by multiple pendulum stages with a resonance frequency of around 1 Hz [Goß04]. If we omit frequencies below 0.2 Hz their residual motion is dominated by frequencies around 1 Hz. This is well below the GEO-HF measurement band. The amplitude of these low frequency fluctuations was conservatively approximated to be $\pm 2 \mu\text{m}$. Given the PRC length of 1200 m this results in a frequency change of the laser of $\pm 470 \text{ kHz}$. Because fluctuations in the OMC length at 1 Hz are negligible due to its monolithic design this introduces a frequency mismatch Δf_{LF} between the interferometer output beam and the OMC resonance frequency of the same amount. At higher frequencies, in the GEO-HF measurement band, length fluctuations of the PRC can be neglected due to the elaborate seismic isolation system of the mirrors forming the PRC.

Audio band frequency fluctuations Δf_{audio} are dominated by the length change of the OMC. Coupling coefficients from Δf_{audio} to the strain measurement were calculated using the software Finesse. We required a design that added less noise than 1/10 shot noise. This results in requirements for Δf_{audio} as

$$\Delta f_{\text{audio}} \leq 10.8 \frac{\text{Hz}}{\sqrt{\text{Hz}}} \frac{470 \text{ kHz}}{\Delta f_{\text{LF}}} \quad (5.1)$$

The required OMC length stability in the measurement band can be restated via

$$\frac{\Delta f}{f} = \frac{\Delta l}{l} \quad (5.2)$$

to

$$\text{OMC length stability} \leq 2.52 \cdot 10^{-14} \frac{\text{m}}{\sqrt{\text{Hz}}} \frac{470 \text{ kHz}}{\Delta f_{\text{LF}}} \quad (5.3)$$

for an OMC length of 65.8 cm.

The ground motion at the GEO 600 site is typically [KAB⁺02]

$$1 \cdot 10^{-11} \frac{\text{m}}{\sqrt{\text{Hz}}} \frac{(100 \text{ Hz})^2}{f^2} \quad (5.4)$$

We assumed very conservatively that this seismic couples directly to OMC length changes, while it is more realistic that the seismic couples greatly to motion of the entire OMC. As described in more detail in section 5.4.1 the OMC seismic isolation provides an attenuation of 85 dB at 100 Hz resulting in motion of the OMC of $5 \cdot 10^{-16} \text{m}/\sqrt{\text{Hz}}$ at 100 Hz. If we conservatively assume a length stability of the OMC of $1 \cdot 10^{-14} \text{m}/\sqrt{\text{Hz}}$ we can derive from eq. 5.3 that OMC length fluctuations at Δf_{audio} result in noise in the strain measurement within design requirements even for an uncontrolled OMC. A low frequency / drift-keeping control is nonetheless required to compensate drifts on minute or hour time scales.

After implementation of the OMC we were able to measure the length fluctuations of the PRC directly by looking into the FB of the OMC longitudinal control. The measured length fluctuations are approximately $0.07 \mu\text{m}$, as presented in fig. 5.6. This is well below the conservative estimate of $\pm 2 \mu\text{m}$ we made earlier.

5.3.2 Longitudinal control scheme

We decided to use a dither / modulation locking [GR83] control scheme for the longitudinal control of the OMC. In this scheme the OMC length is dithered at f_{dither} via the PZT attached to one of its mirrors. At $\Delta f = 0$ this leads to a modulation of the power transmitted through the OMC purely at $2 \cdot f_{\text{dither}}$. With increasing frequency mismatch a modulation in the transmitted power at f_{dither} appears. This is used as the error signal in the OMC length control loop. An illustration of this concept is shown in fig. 5.7. We actuate on the OMC length to have its resonance frequency follow the GEO 600 output beam's frequency. This avoids adding feedback into the complex control loops controlling the PRC length, and according to eq. 5.2 requires less actuator travel due to the OMC being much shorter than the PRC.

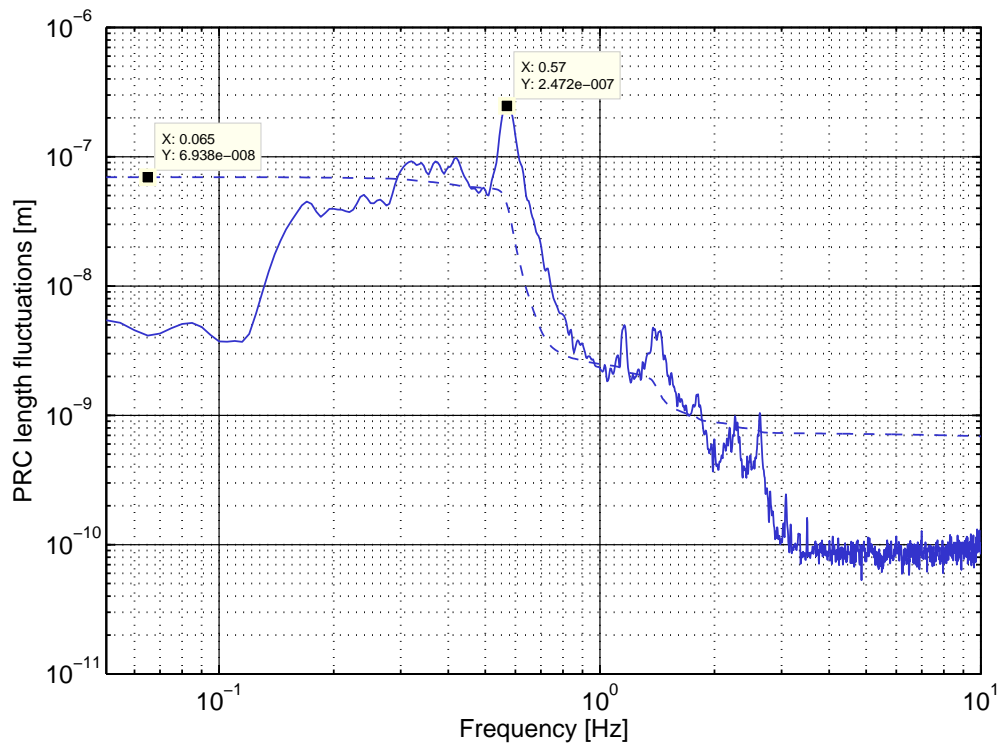


Figure 5.6: PRC length fluctuations as measured via the OMC longitudinal FB. Dashed line: RMS value.

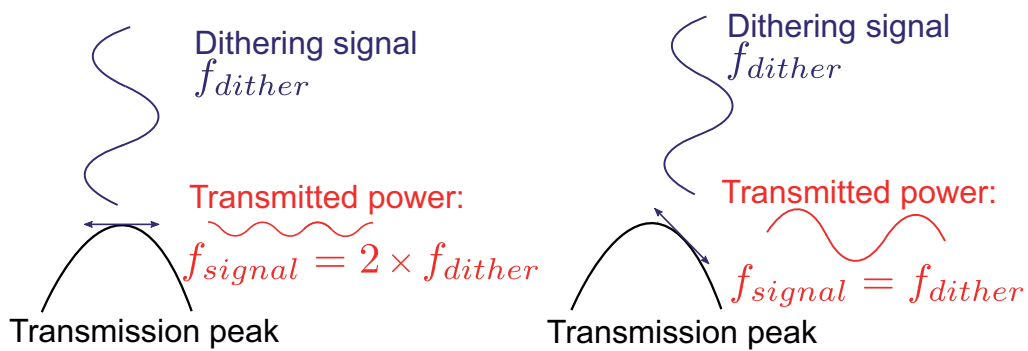


Figure 5.7: Illustration of the dither locking concept in two extreme cases. The error signal is found in transmission of the cavity at the frequency f_{dither} .

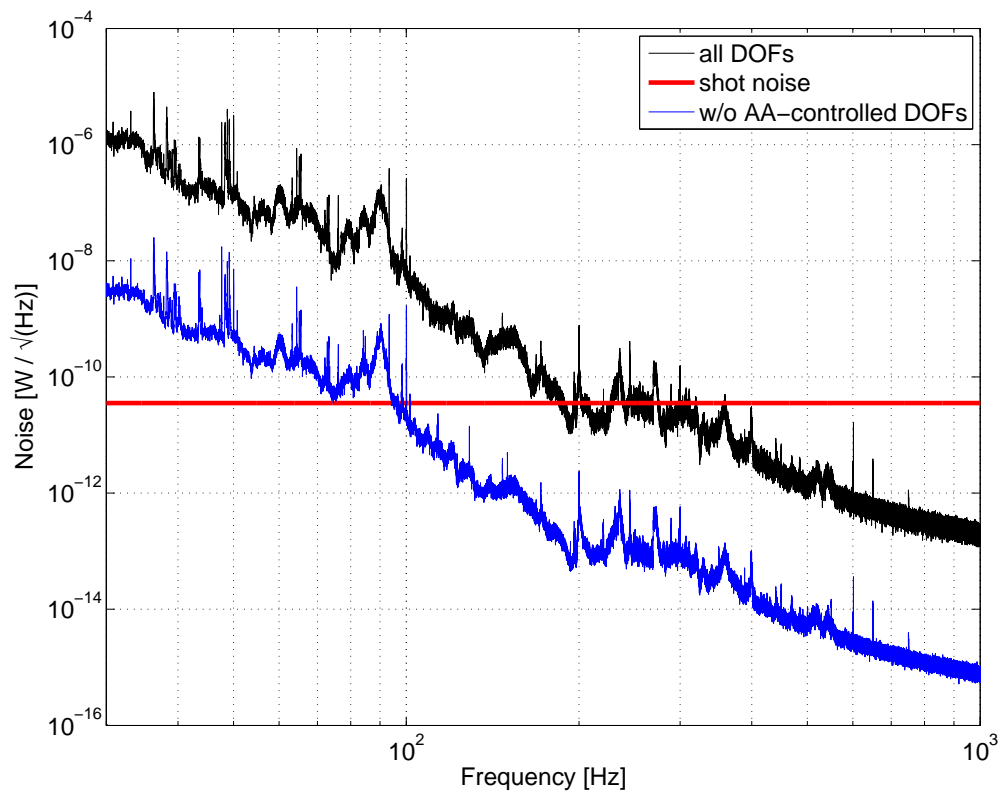
5.3.3 Alignment control requirements

Determination of the alignment control requirements follows the same structure as the determination of the longitudinal control requirements in section 5.3.1. Alignment fluctuations are caused by fluctuations in rotation (yaw) and tilt (pitch) of the interferometer mirrors and translation of the OMC. We concentrated on the mirrors MPR, MCE, MCN, MSR, BDO1, and BDO3 as a sufficient subset (see fig. 1.6). Misalignments of MFE and MFN are canceled in first order by the fact that the *radii of curvature* (ROCs) of MCE and MCN are approximately equal to the arm length, so that beams from the beam splitter that are reflected by MFE and MFN are projected back onto the original spot at the beam splitter. Due to the GEO 600 configuration it is useful to investigate the motions of the mirrors MCE and MCN as degrees of freedom MCE-MCN and MCE+MCN. MCE-MCN is the differential alignment, controlling the overlap of the beams from the two arms. Low frequency rotations and tilts are conservatively assumed to be within ± 250 nrad [Gro03]. Rotation and tilt in the measurement band were estimated by multiplying seismometer (Streckeisen STS-2) data from the GEO 600 site with the respective pendulum transfer functions, which were assumed to be of magnitude 1 up to the pendulum resonance frequency at 1 Hz and f^{-2n} , with n being the number of pendulum stages, for higher frequencies. The number of pendulum stages for different mirrors is presented in table 5.2.

The coupling coefficient from alignment fluctuations in the measurement band to fluctuations in the OMC transmitted power depends for every DOF on the state of alignment of all other DOFs. To establish an upper limit in alignment noise in the OMC transmitted power it was therefore necessary to find, for all other DOFs, the combination of misalignments which maximize this coupling coefficient. We simulated for any DOF all possible misalignments for all other DOFs between -250 nrad and +250 nrad in steps of 50 nrad. This leads to $(7 \text{ DOFs} \cdot 11 \text{ misalignment values} \cdot 2 \text{ axis})^2 = 23716$ combinations. For each DOF we recorded the biggest coupling coefficient and multiplied the alignment fluctuations in the measurement band with it. The resulting fluctuations in the power transmitted by the OMC were summed coherently. The resulting noise is shown in fig. 5.8 (see trace 'all DOFs'). It can be seen that the misalignment falls below shot noise at 300 Hz. The alignment of the DOFs MPR and MCE-MCN are controlled by an *automatic alignment* control (AA) system [Gro03]. If we assume perfect alignment for these DOFs, the upper limit of the alignment noise is shown in trace 'w/o AA-controlled DOFs' in fig. 5.8. These simulations indicate that noise introduced by the OMC falls below shot noise in the 100 Hz to 300 Hz region, and stays well below other technical noises which dominate up to approximately 600 Hz. The conclusion is that we only need a very low bandwidth / drift-keeping automatic alignment system for the OMC that keeps the beams from walking off the mirrors.

Table 5.2: Number of pendulum seismic isolation stages of different GEO 600 mirrors.

	MPR	MCE	MCN	MSR	BDO1	BDO3
# of pendulum stages	2	3	3	3	1	1

**Figure 5.8:** Noise in the power transmitted through the OMC induced by misalignments. Uncalibrated spectrum at the detector behind the OMC. Transmitted power 40 mW.

5.3.4 Alignment control scheme

The state of alignment of a beam onto a cavity is a point in a 4D alignment parameter space. The most instructive way to map this abstract parameter space to intuition is to think of rotations and translations of the intra-cavity beam at the beam waist in the horizontal and vertical plane as the 4 dimensions. Actuators that adjust the alignment can be represented as vectors in this parameter space. For technical reasons, most prominently available actuation ranges, the separation angles between these actuation vectors should ideally be close to 90° . As a rule of thumb, a bigger separation angle leads to a more robust control system. The separation angle is determined by the gouy phase that the fundamental mode of the beam accumulates between the actuators, not by the optical distance of the actuators.

This can be derived from the formalism presented in section 3.1. For convenience eqs. 3.11,3.12 describing a beam translation in $-x$ direction by dx and a tilt by α_x around the y -axis are reproduced here. Because we do not consider a resonator beam the superscripts discerning between incoming beam and resonator eigenmode were omitted in eq. 5.5.

$$\text{Beam translation: } \psi^{\text{HG}}(x) \stackrel{dx \approx 0}{\approx} A_1 \left(\psi_{m=0}^{\text{HG}}(x) + \frac{dx}{\omega_0} \psi_{m=1}^{\text{HG}}(x) \right) \quad (5.5a)$$

$$\text{Beam tilt: } \psi^{\text{HG}}(x) \stackrel{\alpha_x \approx 0}{\approx} A_2 \left(\psi_{m=0}^{\text{HG}}(x) + i\sqrt{\pi}\omega_0\alpha_x\psi_{m=1}^{\text{HG}}(x) \right) \quad (5.5b)$$

Equation 5.5 shows that rotations create first order modes 90° out of phase with the fundamental, while displacements create first order modes in phase with the fundamental. During propagation the first order modes accumulate twice as much gouy phase shift as the fundamental mode (see eq. 3.1). An actuator that rotates the beam looks therefore, after a propagation that causes a 90° gouy phase shift of the fundamental, like an actuator that displaces the beam. Two beam rotators separated by 90° gouy phase shift therefore constitute an optimal set of actuators.

We investigated the separation angles for two different optical configurations. The alignment actuators are the BDO1 and BDO3 mirrors (see fig. 1.6). The distances between the different output optics components are approximately constant and presented in table 5.3. The boundary condition for this investigation was that a good mode-matching of the beam onto the OMC needed to be possible. Mode-matching efficiency with spherical lenses is limited by the astigmatism of the GEO 600 output beam. The investigated configurations were:

1. No BDO mirror change. Mode-matching via two lenses.
2. Replacing the flat BDO2 mirror with a curved mirror. Mode-matching via one lens.

The angles of separation for different BDO2 ROCs are presented in fig. 5.9. The different configurations are described in table 5.4. We decided on configuration 1 because it offered the benefit of keeping the existing BDO mirrors.

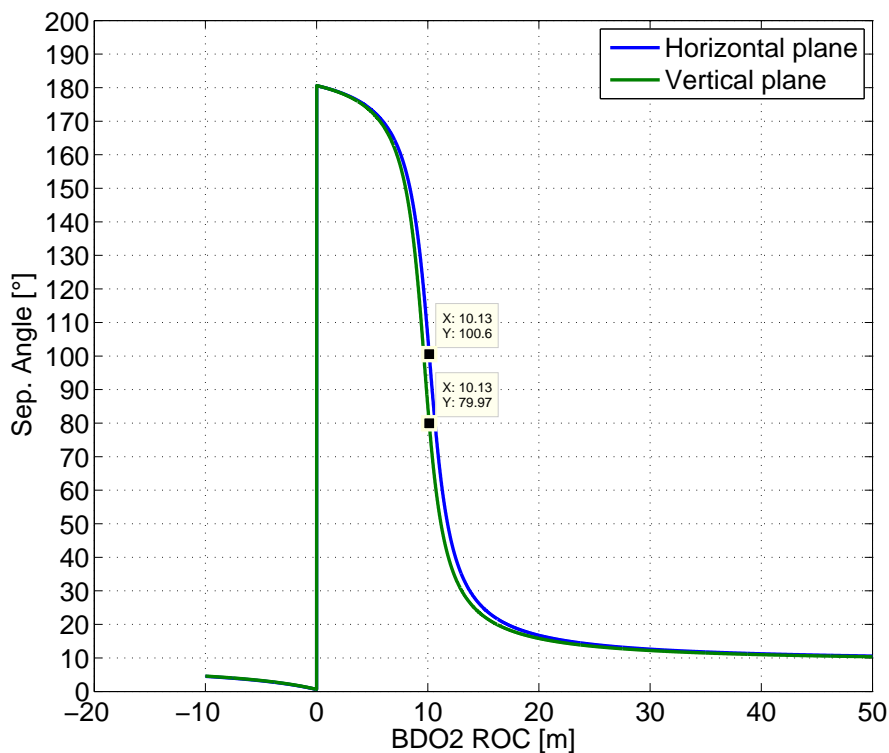


Figure 5.9: Separation angle between BDO1 and BDO3 for different BDO2 ROCs. For $\text{ROC} \rightarrow \infty$ the separation angle approaches 8.5° .

Table 5.3: Approximate relative distances between adjacent output optics components. Starting at the signal-recycling mirror. See fig. 1.6 for a depiction of the arrangement of these components.

Component	Distance [m]
Signal-recycling mirror	0
BDO1	1.80
BDO2	1.58
BDO3	1.35
L1	1.2
L2	0.34
OMC input mirror	0.20

Table 5.4: Comparison of optical configurations of the output optics and resulting separation angles for the actuators BDO1 and BDO3. The two separation angles are for the horizontal and vertical plane. R_{BDO1} and R_{BDO2} are the radii of curvature of BDO1 and BDO2. f_{L1} and f_{L2} are the focal lengths of the mode-matching lenses. The mode-matching (MM) is given as transmittance (in power) of the OMC of the fundamental mode carrier light.

Configuration	R_{BDO1} [m]	R_{BDO2} [m]	f_{L1} [m]	f_{L2} [m]	Sep. angle [°]	MM [%]
Existing BDO2	6.27	∞	0.25	-0.052	8.5 & 8.5	98.3
Alternative BDO2	6.27	10.13	-0.2448	∞	100.6 & 80.0	97.0

Several designs for the automatic alignment system were investigated:

1. Dither lock with four frequencies. Dithering is applied to BDO1 and BDO3: Both rotation and tilt degrees of freedom for BDO1 and BDO3, respectively, are dithered at separate frequencies f_1 to f_4 . At perfect alignment the power transmitted through the OMC will be modulated at frequencies $(2 \cdot f_1)$ to $(2 \cdot f_4)$. Modulations at f_1 to f_4 appear in the transmitted power with amplitudes proportional to misalignment. With the available actuators, the maximum possible dither amplitude is limited to

$$\text{Dither amplitude} \leq 5.7 \cdot 10^{-7} \text{ rad} \frac{(100 \text{ Hz})^2}{f_{\text{dither}}^2} \quad (5.6)$$

In the simulation we assumed a dither amplitude of $1 \cdot 10^{-7}$ rad which corresponds to a maximum dither frequency of about 240 Hz. This dithering leads to an RMS loss in the OMC transmitted power as presented in table 5.5.

2. Dither lock with a common frequency. Dithering is applied to BDO1 and BDO3: Again the BDO mirrors are dithered. This time with a common frequency ($f_1 = \dots = f_4$). The light reflected off the OMC is split 50:50 and detected by two quadrant photo

Table 5.5: Relative loss in the OMC transmitted power due to dithering of the BDO DOFs at $1 \cdot 10^{-7}$ rad.

DOF	RMS relative power loss [1]
BDO1 rotation	$6.4 \cdot 10^{-10}$
BDO1 tilt	$5.8 \cdot 10^{-10}$
BDO3 rotation	$1.1 \cdot 10^{-14}$
BDO3 tilt	$3.2 \cdot 10^{-15}$

detectors. The Gouy phase shift between them is $\pi/2$. Essentially this is differential wavefront sensing [MMR⁺94] with sidebands created by dithering the BDO mirrors instead of by an electro-optic modulator. HOM-content of the GEO 600 output beam was assumed to be 1.4 mW. Ideal mode-matching was assumed.

3. Dither lock with a common frequency. Dithering is applied to the OMC length: In this configuration the OMC length is dithered. The same OMC length dither can be used for longitudinal and alignment control. The full width at half maximum of the OMC resonance is about 7 nm. The dither amplitude was assumed to be 1 nm, leading to a loss in OMC transmitted power of approximately 5%. Just as in design 2 the light reflected off the OMC is split 50:50 and detected by two quadrant photo detectors.

The shot noise limited sensitivities of designs 1 to 3 were estimated using the Finesse software for a power of 40 mW transmitted through the OMC. Their sensitivities are presented in table 5.6. We decided to implement design 1 for its simplicity.

Table 5.6: Shot noise limited sensitivity of different designs for the output mode cleaner automatic alignment system in terms of BDO1 and BDO3 misalignments.

	Shot noise limited sensitivities [rad]		
	Design 1	Design 2	Design 3
BDO1 rotation	$4.88 \cdot 10^{-12}$	$9.00 \cdot 10^{-3}$	$2.04 \cdot 10^{-9}$
BDO1 tilt	$1.95 \cdot 10^{-10}$	$9.30 \cdot 10^{-4}$	$1.48 \cdot 10^{-9}$
BDO3 rotation	$1.05 \cdot 10^{-9}$	$7.26 \cdot 10^{-2}$	$2.70 \cdot 10^{-8}$
BDO3 tilt	$9.78 \cdot 10^{-8}$	$1.19 \cdot 10^{-1}$	$3.15 \cdot 10^{-8}$

5.4 Details of the implementation of the output mode cleaner

The OMC is located in a dedicated vacuum tank called TCOc (see fig. 5.11 and 5.13). The pressure in TCOc is kept in the high 10^{-3} mbar range. This reduced pressure reduces fluctuations in the refractive index of air, keeps the beam path free of dust particles, and provides some isolation from acoustic noise. The tank is separated from the other GEO 600 vacuum tanks by a septum window allowing for venting and pump-down in a matter of hours, thereby allowing easy access to the OMC.

5.4.1 Vibration isolation

The vibration isolation of the OMC is the first in GEO 600 that is not based on wired pendulums. The OMC is located on top of a multi-stage seismic isolation as depicted in fig. 5.11. The main isolation stage consists of three SM-30 isolators by Minus-K Technology Inc. These provide isolation of 10 dB at 1 Hz and 45 dB above 10 Hz from motion in the horizontal and vertical directions. Additional seismic isolation is provided by three layers of fluorubber (viton[®] and fluorel[®]) pads. Each layer of rubber acts as a damped harmonic oscillator, amplifying excitations at its resonance frequency f_0 and providing seismic isolation for frequencies $f > \sqrt{2}f_0$. We calculated f_0 following [Saw12]

$$f_0 = \frac{\sqrt{D/m}}{2\pi} \quad (5.7)$$

$$D = \frac{EA}{L} \quad (5.8)$$

with

f_0 = Harmonic oscillator's resonance frequency

D = Spring constant

E = Young's modulus = $5.8 \frac{\text{N}}{\text{mm}^2}$ for viton[®]

A = Rubber surface area

L = Rubber thickness

m = Suspended mass

The top layer consists of four hand-cut rubber pieces. The middle layer consists of four O-rings with an outer diameter of 60 mm and a thickness of 5 mm. The bottom layer consists of 20 rubber pieces with the dimensions $10 \times 10 \times 5 \text{ mm}^3$. The properties of these isolation layers are presented in table 5.7.

Mind that the effective suspended mass of the lower layers is not necessarily the physical mass on top of those layers. The effective suspended mass can be smaller than the physical

mass above it, if that mass is suspended by another isolation system with similar or lower resonance frequency f_0 . To conservatively estimate the performance of the rubber isolation layers we estimated the effective suspended mass of each layer as the mass between that layer and the next layer above it.

Damped harmonic oscillators provide isolation at frequencies $f > \sqrt{2}f_0$. For frequencies $f \gg f_0$ this isolation takes on a $1/f^2$ characteristic. For frequencies $f \approx f_0$ the behavior depends on the damping. Velocity damping only affects the height of the amplification of excitations at the resonance frequency f_0 and is therefore of little interest here. The effect of damping due to internal friction on a harmonic oscillator's transfer function is presented in eq. 5.9 [Sau94] and fig. 5.10.

$$TF = \frac{f_0^2 (1 + \phi)}{f_0^2 - f^2 + if^2\phi} \quad (5.9)$$

with

TF = Magnitude of the oscillators transfer function.

ϕ = Loss angle. Describes the damping due to internal friction. $[\phi] = 1$

We did not measure the loss angle of the rubber pads, but we expect it to be non-negligible, meaning we receive less than $1/f^6$ isolation from the three layers of rubber pads for frequencies slightly above their respective resonance frequencies f_0 .

5.4.2 Optical configuration in the output mode cleaner's vacuum tank

The optical configuration inside TCOc is presented in fig. 5.13. The lenses adjust the mode-matching onto the OMC. The Faraday rotator in conjunction with the beam splitter acts as a Faraday isolator impeding backscattering from the OMC into the interferometer. The beam splitter is also used to couple the squeezed vacuum into GEO 600 [Kha11].

Table 5.7: Properties of the rubber vibration isolation stages of the OMC.

	Isolation layer		
	Top	Middle	Bottom
L [mm]	0.5	5	5
A [mm ²]	78	13200	2000
m [kg]	6.2	112	80
f_0 [Hz]	61	58	27
Isolation above [Hz]	86	82	38

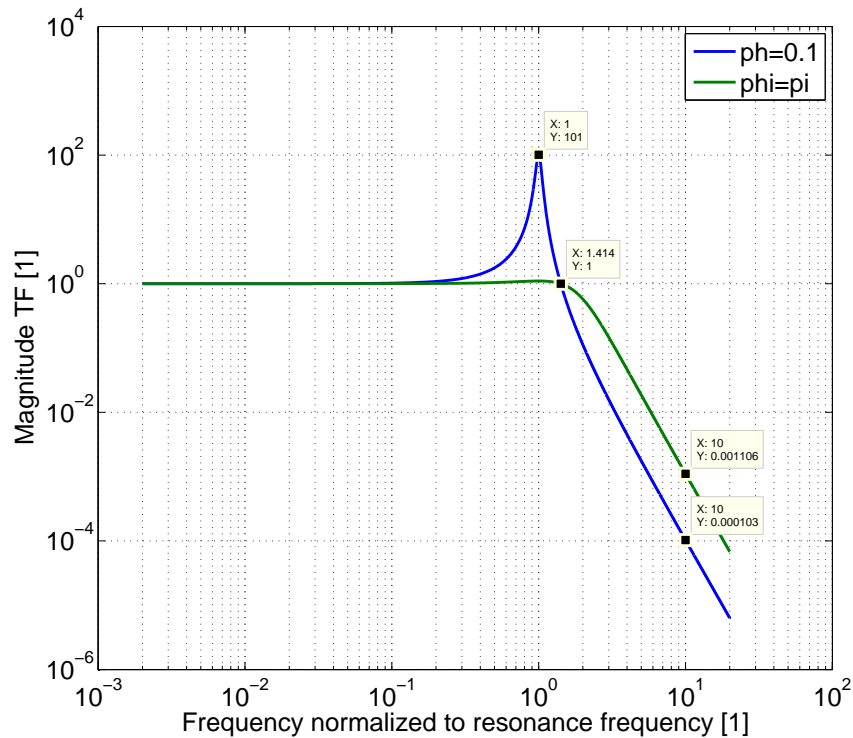


Figure 5.10: Calculated magnitude of the transfer function of a harmonic oscillator for different amounts of internal friction. Calculated according to eq. 5.9.

The light reflected off the OMC is directed to a quadrant photodiode located on an optical table in air. This beam can be used to ascertain the mode-matching onto the OMC as described in section 5.4.3. The beam transmitted by the southern OMC mirror with (transmission = 10^{-4}) is directed towards a CCD camera on an optical table in air. This picture allows us to see which mode is circulating inside the OMC. The OMC transmitted beam, which carries the gravitational wave signal, is detected in vacuum by a custom-made photodiode (by Fraunhofer Heinrich Hertz Institute) with a quantum efficiency of approximately 99%.

5.4.3 Mode-matching

Adjusting the mode-matching onto the OMC is a challenging task due to the high HOM content in the interferometer's output beam. As presented in section 3.5 incorrect mode-matching onto the OMC can convert HOMs in the output beam back to the fundamental mode. Maximizing the OMC transmitted power in the fundamental mode is therefore not optimizing the mode-matching.

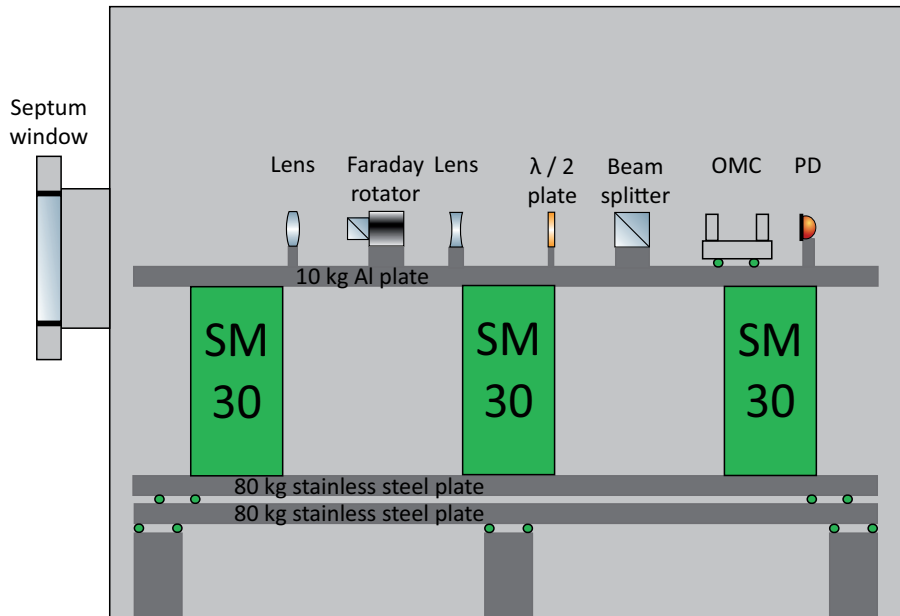


Figure 5.11: Schematic view of the OMC vacuum tank TCOc. The elements providing seismic isolation are colored green. Note the three layers of rubber pads depicted as green circles. Not to scale.

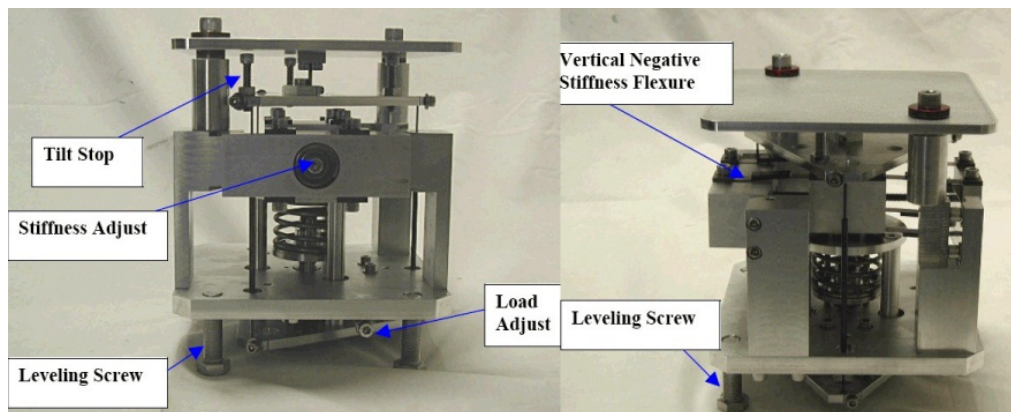


Figure 5.12: SM-30 seismic isolators by Minus-K Technology Inc. The weight of each isolator is approximately 12 kg.

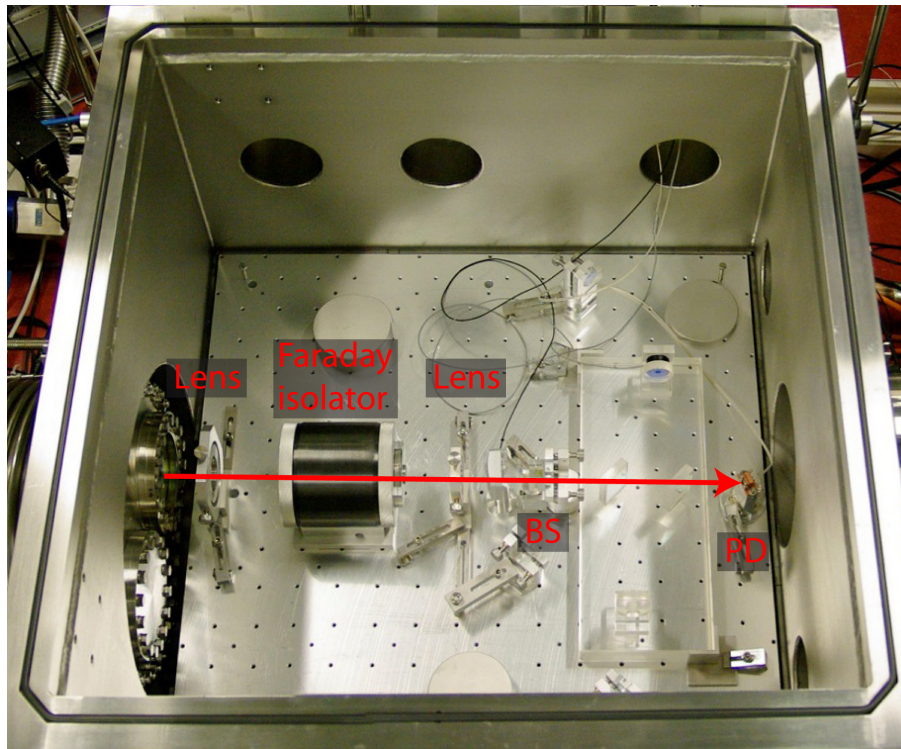


Figure 5.13: Optical path inside TCOc. **BS:** Beam splitter, **PD:** Photodiode

We developed a technique using the 14.9 MHz sidebands to ascertain the mode-matching efficiency. In this we detect the LG_{02} mode and the fundamental mode of the 14.9 MHz SBs in transmission and reflection of the OMC. These SBs contain less HOMs than the carrier light due to the resonance conditions of the dual-recycled interferometer. Therefore they are better suited to ascertain the mode-matching than the carrier light.

1. We lock the OMC onto the fundamental mode of the 14.9 MHz sideband and measure the OMC transmitted power.
2. We lock the OMC onto the LG_{02} mode of the 14.9 MHz sideband and measure the OMC transmitted power.
3. The ratio of the power measured in step 1 and 2 provides us with the mode-matching efficiency.

We were able to achieve a mode-matching efficiency of 98.0%.

5.4.4 Control system infrastructure

The OMC control systems needed to be integrated into the pre-existing GEO 600 control systems infrastructure. The OMC control is the first application of the fully digital *Control and Data System* (CDS) [Bor10] in GEO 600. It is based on, and very similar to, the system planned for Advanced LIGO. CDS is a real-time control system with selectable cycle frequency of up to 64 kHz. We decided to use a cycle frequency of 32 kHz, providing us with additional processing time. CDS and a PC running National Instruments *LabView* (LV) 2009 collectively form the OMC control system. LV 2009 is responsible for high-level non-real-time duties and provides a *graphical user interface* (GUI) for the OMC. Most pre-existing GEO 600 control systems are analog electronics, supervised by National Instruments LV 6.1. The LV 2009 PC interfaces the OMC control system with these pre-existing LV 6.1 systems. LV 2009 communicates with CDS via the channel access protocol component of the *Experimental Physics and Industrial Control System* (EPICS) over Ethernet, and with LV 6.1 via a direct *user datagram protocol* (UDP) link at 10 Hz also over Ethernet. It provides the OMC control system with information regarding the interferometer's lock status and also handles some communications regarding the squeezing.

A fully automated lock acquisition for the OMC was developed to allow for autonomous operation of the OMC subsystem, which is imperative to ensure a high duty cycle of GEO 600. The OMC is locked after the interferometer acquires lock, meaning the relative arm lengths and the lengths of the PRC and SRC are kept close to a defined operating point. During the OMC lock acquisition the relative arm lengths of the interferometer and thereby the output beam power is controlled via a quadrant photodiode in transmission of BDO1. The logic scans the OMC length over slightly more than one FSR, and monitors the transmitted power. It watches for a characteristic triplet structure formed by the fundamental modes of the carrier light and control sidebands at 14.9 MHz. Once this is found the position of the middle peak of this triplet is recorded as the desired OMC length. The OMC then jumps back to its starting position and scans toward the pre-recorded position. A blind ramping to the position of the carrier fundamental mode is not possible due to non reproducible PZT hysteresis. When near this position the logic watches transmitted power and OMC longitudinal error signal. If the former is above a certain threshold, and the latter is sufficiently small the OMC longitudinal lock is enabled. This happens in three steps over 6 seconds increasing the DC-gain in each step. After this lock is engaged control of the interferometer transmitted power is transferred to the photodiode in transmission of the OMC. The OMC alignment control is enabled after the OMC longitudinal lock is activated by ramping the control gains up from zero over a period of 90 seconds. The stepwise and gradual activation of the longitudinal and alignment control loop, respectively, minimize nonlinearities and increase the robustness of the lock activation. Changing the gain of a control system at frequencies on the order of its *unity gain frequency* (UGF) makes a linear treatment insufficient, and the control system has to be considered nonlinear. A stepwise increase of the longitudinal gain introduces gain

changes in a broad frequency range. Since the longitudinal control is already active with a high UGF when we change the gain the nonlinearities stay small. A slow ramping of the alignment gain introduces gain changes mainly at low frequencies, so that the loop is only nonlinear while its UGF, and therefore gain, are low.

The automated lock acquisition allows the OMC subsystem to work fully autonomously for weeks at a time. Typically an OMC relock fails due to a problem with the interferometer that considerably changes the output beam parameters or a severe earthquake happening somewhere on the planet creating considerable misalignments in GEO 600.

When the interferometer loses lock the power stored in the dual-recycling cavities can create a high-powered laser pulse. This is known as cavity dumping [HDP66]. The stored power for an interferometer input power of 3 W, a PR gain of 1000 and a total arm length of 2400 m is described in eq. 5.10.

$$E = P_{\text{input}} \frac{L_{\text{arm}}}{c} = 0.024 \text{ J} \quad (5.10)$$

We evaluated the energy and maximum power of the pulses dumped towards the OMC. We evaluated 17 losses of lock for the configuration with a reflectivity of the signal-recycling mirror of $R = 98\%$ and 41 losses of lock for a reflectivity of $R = 90\%$. The corresponding pulse energies and peak powers are presented in figs. 5.14,5.15. In fig. 5.16 we present the pulse shapes we found for $R = 90\%$. Clearly a reduced reflectivity of the signal-recycling mirror leads to stronger pulses being dumped towards the interferometer's output.

To protect the sensitive photodiode in transmission of the OMC we implemented a safety mechanism in CDS that shifts the OMC length off of resonance within 2 ms if an

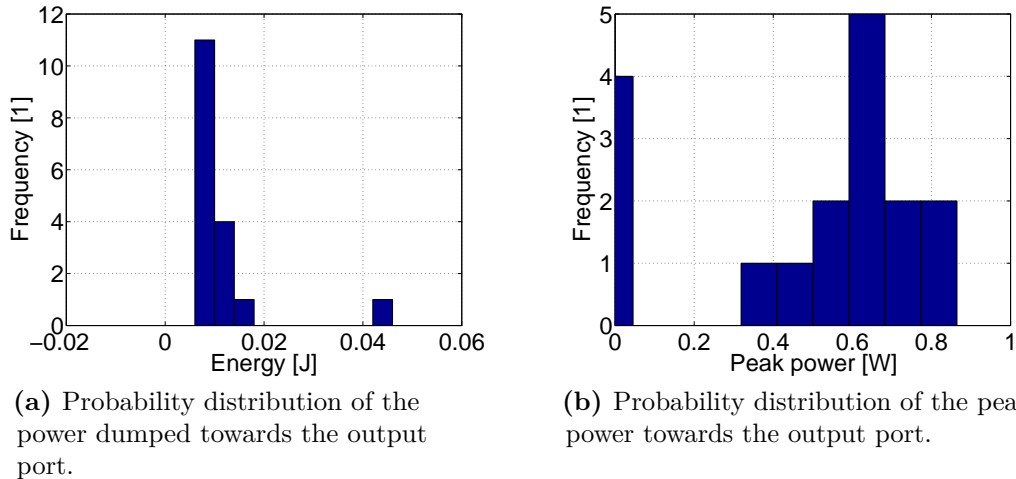


Figure 5.14: Parameters of the laser pulses emitted towards the OMC by cavity-dumping of the dual-recycling cavities for a reflectivity of the signal-recycling mirror of 98%.

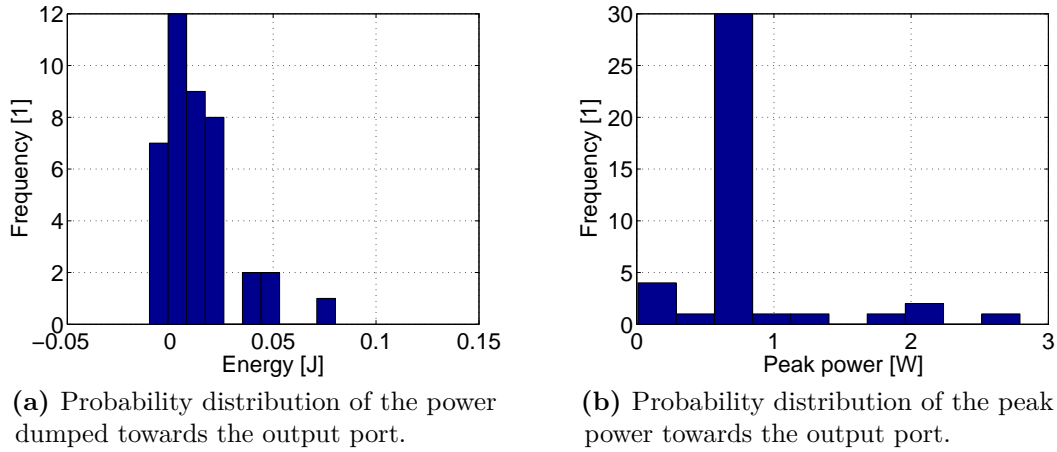


Figure 5.15: Parameters of the laser pulses emitted towards the OMC by cavity-dumping of the dual-recycling cavities for a reflectivity of the signal-recycling mirror of 90 %.

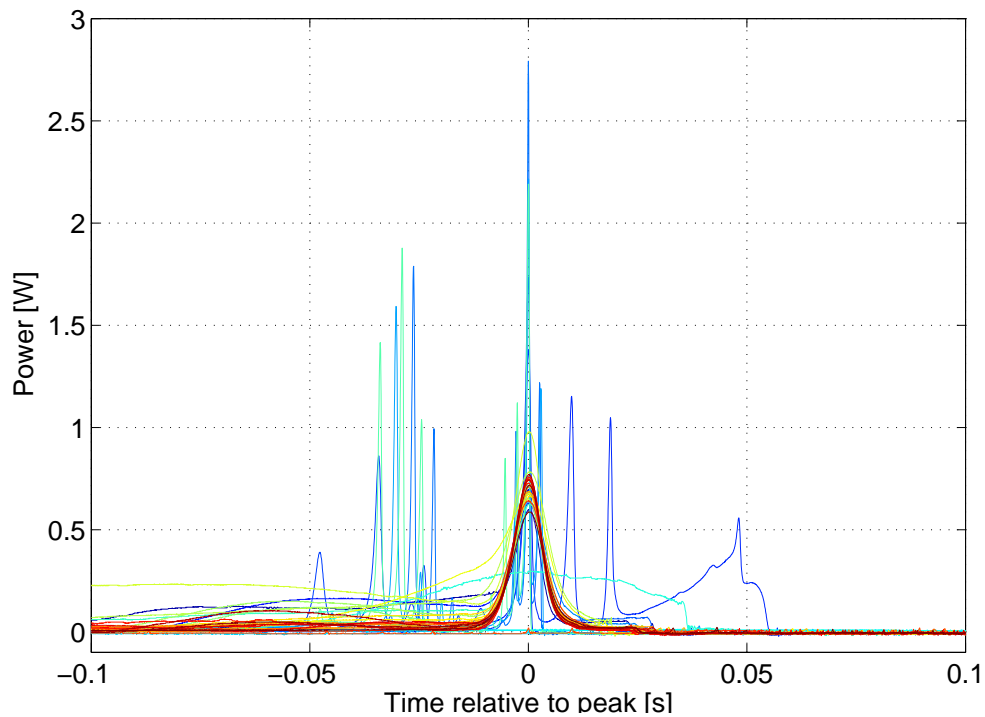


Figure 5.16: Shape of the laser pulses emitted towards the OMC by cavity-dumping of the dual-recycling cavities for a reflectivity of the signal-recycling mirror of 90 %.

excessive amount of power is detected in transmission of the OMC. No photodiode was damaged by cavity dumping.

5.4.5 Longitudinal control implementation

We implemented a low bandwidth dither locking control for the OMC length. The OMC length was dithered by a Physik Instrumente S-303 PZT with a $3\ \mu\text{m}$ or approximately 6 FSR actuation range. The dither signal at 6 kHz was generated in CDS at an peak-to-peak amplitude of 0.42 mV.

We calibrated the OMC dither amplitude to approximately 3 pm peak-to-peak. We measured the voltage needed to cover 1 FSR ($\cong 532\ \text{nm}$) resulting in the calibration factor of 7.09 nm/V. We then calibrated the dither voltage with this to 2.8 pm peak-to-peak. We checked this value by using the following other calibration method: We calibrated the simulated OMC transmitted power to fit the measured DC value. We then dithered the OMC length at 3 kHz and observed the power fluctuations in transmission of the OMC at 6 kHz. We then applied the DC calibration factor to scale the measured power fluctuations at 6 kHz to corresponding length changes in the simulation. The resulting dither amplitude is 0.7 pm peak-to-peak. Past experience tells us that the former calibration method is generally more accurate. Both calibrations agreeing to within an order of magnitude inspires confidence in the approximate calibration value.

The FB signal was sent to a custom-made HV-amplifier with a gain factor of 17. Its output voltage was limited to 114 V, which is below the manufacturer specified maximum voltage of 120 V for the PZT. The dither and FB signals were then added in a custom-made summing box (see fig. 5.17). The dither frequency f_{dither} was chosen as 6 kHz, which places the signal generated at $2 \cdot f_{\text{dither}}$ to 12 kHz out of GEO 600's measurement band that extends to 8 kHz. The *open loop gain* (OLG) of this control loop is depicted in fig. 5.18. Resonant gains were introduced into this loop at 0.55 Hz and 1.3 Hz to provide high gain at the longitudinal resonances of the main mirrors' suspensions, which lead to

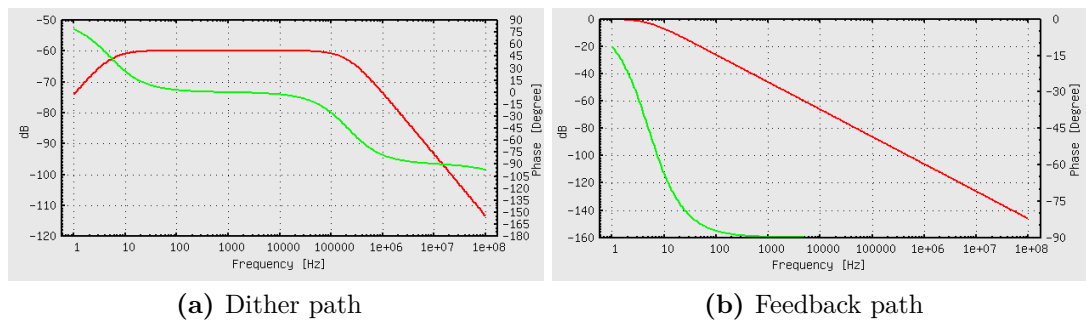


Figure 5.17: Transfer functions of the PZT summation box. Magnitude in red, phase in green.

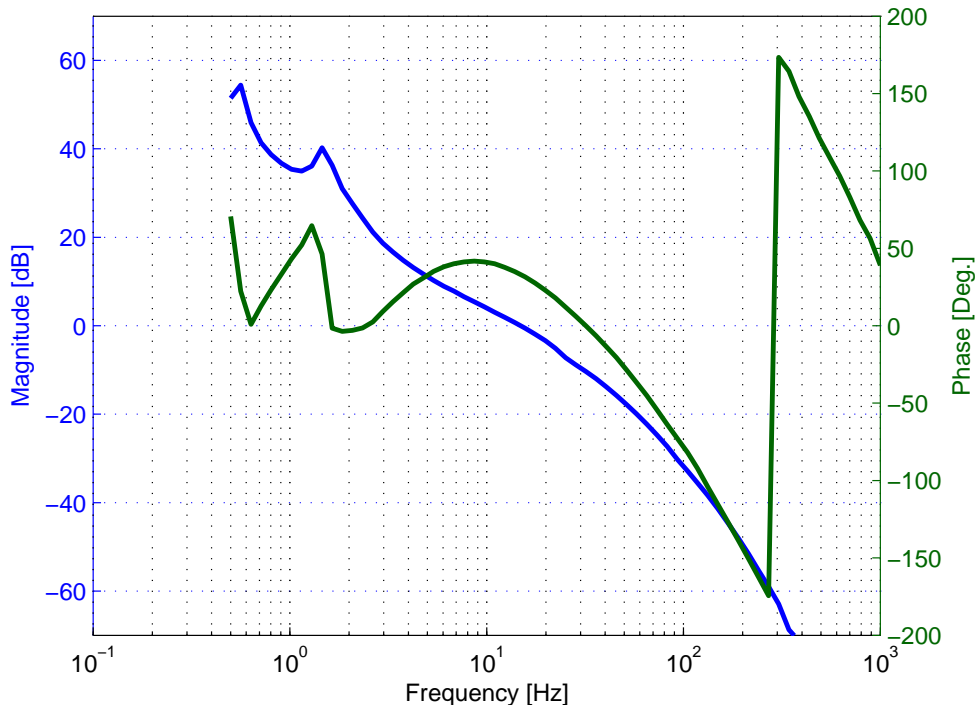


Figure 5.18: Measured OLG of the OMC longitudinal control loop. UGF = 15 Hz, phase margin = 36° , gain margin = 10 dB and -37 dB, DC-gain = 108 dB

strong PRC length fluctuations at these frequencies, as presented in fig. 5.6, and thereby strong fluctuations in the relative frequency Δf between the interferometer’s output beam and the OMC resonance frequency. Increasing the OLG decreases Δf , but increases the FB noise at high frequencies, above the UGF. An example of this problem is clearly evident in fig. 6.1 where the dominant noise source below 100 Hz is the FB noise of the Michelson interferometer’s alignment system which has a UGF of approximately 20 Hz [Gro03]. To alleviate this effect we introduced digital high order low-pass filters into the OMC longitudinal control loop leading to a sharp drop in OLG above the UGF.

5.4.6 Alignment control implementation

The initial automatic alignment system was implemented in June 2010 and used until March 2011 when the change of the signal-recycling mirror necessitated a new solution as described in section 5.5.

The BDO1 and BDO3 mirrors were dithered in rotation and tilt at frequencies between 265 Hz and 520 Hz by signals generated in CDS. The exact frequencies were chosen for

especially low technical noises providing maximum SNR for the alignment control. The FB is also generated in CDS. Dither and FB are sent to the coil-magnet actuators (see fig. 5.19) at BDO1 and BDO3 via two pre-existing electrical pathways. The transfer function of these is depicted in fig. 5.20. The slow path is used to apply the FB and the fast one to apply the dithering. This division ensures a low level of feedback noise. The initial control setup is described in table 5.9.

We checked the validity of the error signal by measuring the error signal while applying dithering to the BDO mirrors and not applying the feedback signal. This was then compared to the sensing noise measured without dithering the BDO mirrors. The error signal is valid up to the frequencies at which these two signals converge (see table 5.8). Above this frequency sensor noise, which can not be suppressed by the control loop, dominates the error signal¹.

The OLG of the BDO alignment control loops is shown in fig. 5.21. The loop shape was known and the overall gain was fitted to an OLG measurement at 0.2 Hz. A higher bandwidth control with a UGF of 3 Hz was implemented but did not show any apparent benefits. Dead-band control loops (see fig. 5.22) were created in LV ‘around’ the CDS control loops. The LV loops average the signal to the BDO1 and BDO3 actuators over

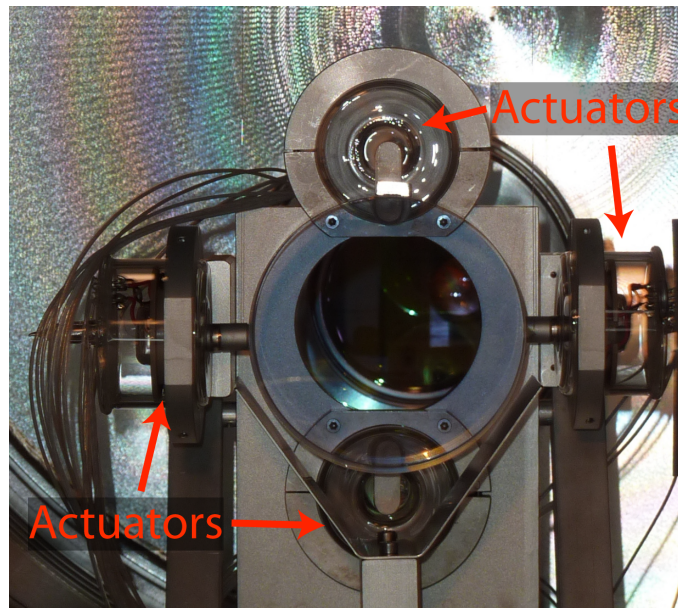


Figure 5.19: BDO mirror with attached coil-magnet actuators.

¹ For in-loop measurements the error signal can in principle be suppressed below sensor noise, however the actual performance of the control loop, measured out-of-loop, can not exceed the limit set by the sensor noise.

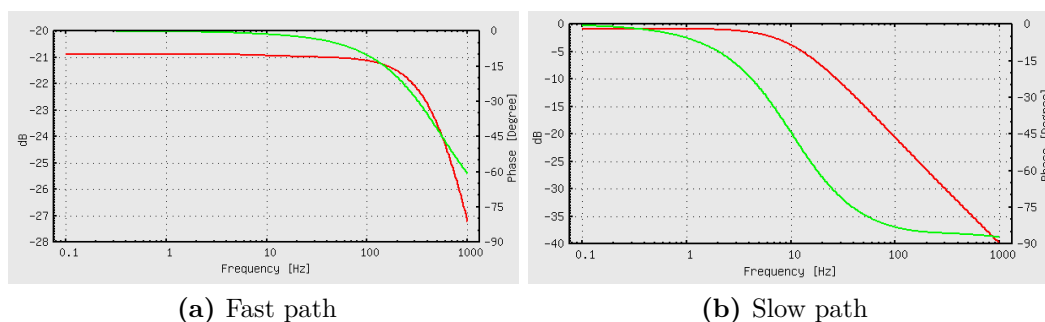


Figure 5.20: BDO coil-magnet actuator pathways. Magnitude in red, phase in green.

Table 5.8: Alignment control error signal validity.

Degree of freedom	Dither freq. [Hz]	Dither ampl. [nrad]	Error signal valid to freq. [Hz]
BDO1 rotation	265	1.35	2.0
BDO1 tilt	420	0.05	0.6
BDO3 rotation	530	0.9	1.0
BDO3 tilt	480	0.6	0.8

Table 5.9: Alignment control loop gain hierarchy as employed during S6/VSR3.

Degree of freedom	UGF [mHz]	DC-gain [dB]
BDO1 rotation	24	16
BDO1 tilt	22	15
BDO3 rotation	11	7
BDO3 tilt	40	25

500 seconds. If these values are out of the dead-band the FBs were offloaded from the CDS loops to the LV loops. This ensures that the BDO mirrors stay well aligned when the CDS loops are reinitialized when GEO 600 loses lock.

We handled the problem of small separation angle between DOFs by using a gain hierarchy. In the two DOFs between which there is a small separation angle (rotation of BDO1 & 3, and also tilt of BDO1 & 3) one has a considerably bigger gain. This dominating DOF compensates the majority of any misalignment. Only the residuals are then compensated by the remaining DOF.

A more mathematical illustration can be seen in fig. 5.24. In fig. 5.24a there is the physical alignment space displayed. The actuators are vectors in this space. Fig. 5.24b

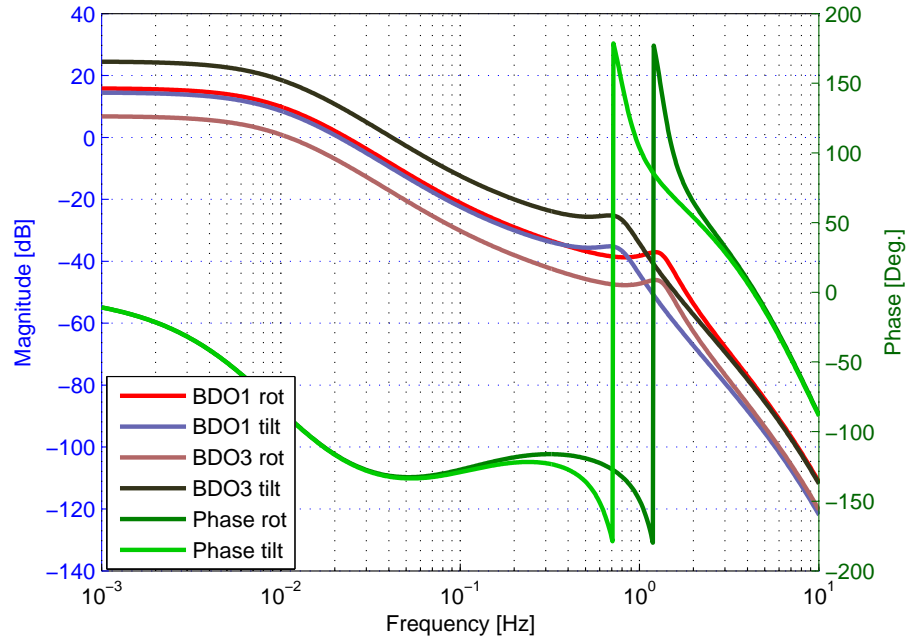


Figure 5.21: OLG of the alignment control for the BDO mirrors. The known loop shapes were fitted to the measured OLG at 0.2 Hz.

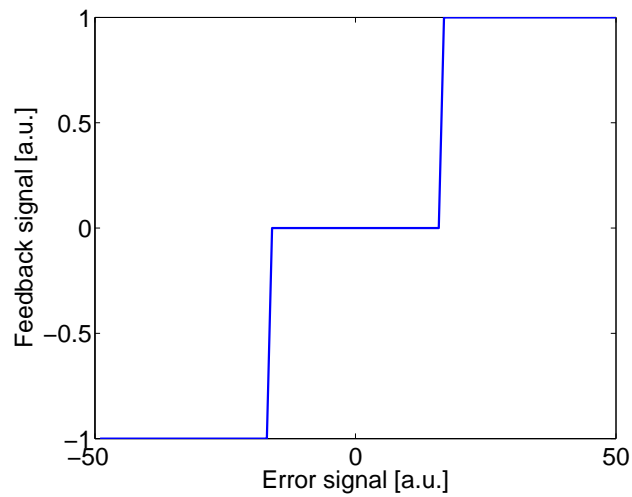


Figure 5.22: Illustration of a dead-band control.

displays the alignment space in the basis of actuation vectors with a separation angle of 8° . This transformation is a shearing coordinate transformation of the form described in eq. 5.11 and fig. 5.23. In this basis the color coding represents the error signal of the alignment control. We can then apply different gains to these error signals $g_{\text{BDO1}} \neq g_{\text{BDO3}}$ in the control servo. As can be seen in fig. 5.24c this balances the feedback to BDO1 and BDO3 actuators somewhat.

$$\begin{pmatrix} \text{DOF1} \\ \text{DOF2} \end{pmatrix} = \begin{pmatrix} g_{\text{BDO1}} \cos(\alpha) & -g_{\text{BDO3}} \sin(\beta) \\ g_{\text{BDO1}} \sin(\alpha) & g_{\text{BDO3}} \cos(\beta) \end{pmatrix} \begin{pmatrix} \text{BDO1 rot} \\ \text{BDO3 rot} \end{pmatrix} \quad (5.11a)$$

$$\begin{pmatrix} \text{BDO1 rot} \\ \text{BDO3 rot} \end{pmatrix} = [\cos(\alpha) \cos(\beta) - \sin(\alpha) \sin(\beta)] \begin{pmatrix} \frac{\cos(\beta)}{g_{\text{BDO1}}} & \frac{\sin(\beta)}{g_{\text{BDO1}}} \\ -\frac{\sin(\alpha)}{g_{\text{BDO3}}} & \frac{\cos(\alpha)}{g_{\text{BDO3}}} \end{pmatrix} \begin{pmatrix} \text{DOF1} \\ \text{DOF2} \end{pmatrix} \quad (5.11b)$$

This automatic alignment system was used when GEO 600, VIRGO and the LIGO detectors were all aiming for a maximum duty factor between 11th August and 20th October 2010. This time coincides with VIRGO's VSR3 science run also from 11th August to 20th October 2010 and overlaps with the S6D science run of the LIGO detectors from 26th June to 20th October 2010. In this period GEO 600 achieved a duty cycle of 88%, VIRGO achieved 70%, and the LIGO detectors achieved 64% for H1 and 65% for L1. This showed that the GEO 600 configuration with OMC was sufficiently robust.

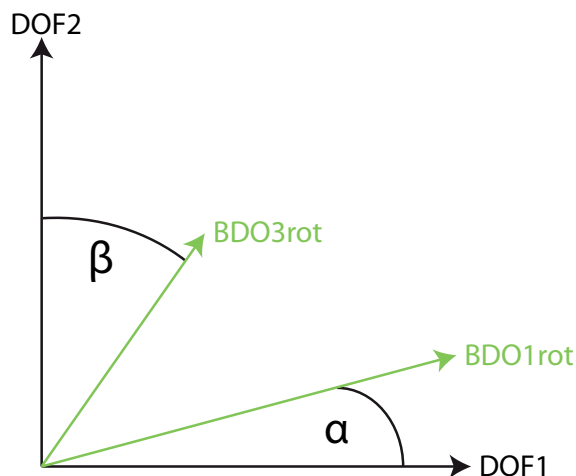
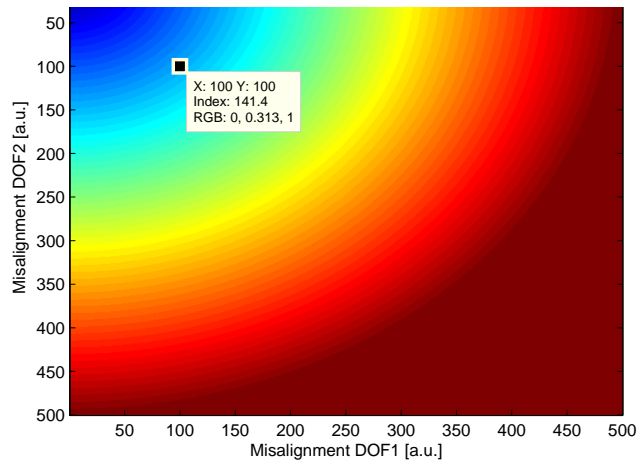
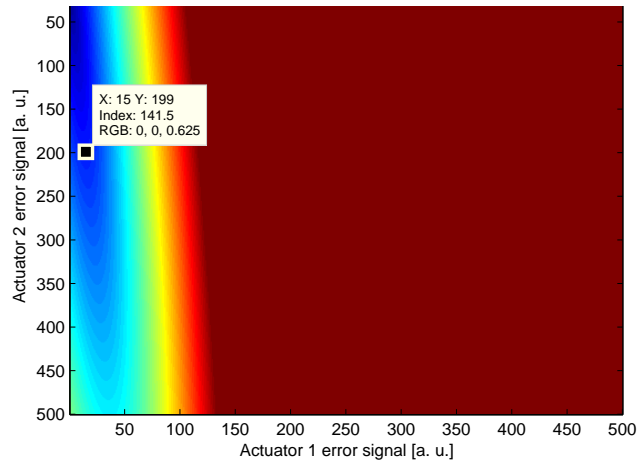
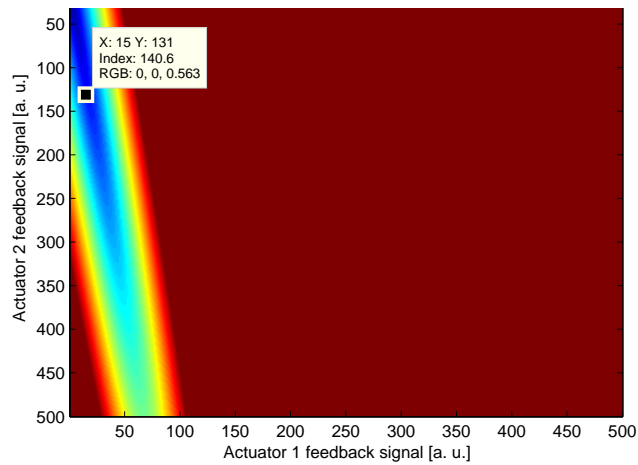


Figure 5.23: Shearing coordinate transformation in one plane. Defined by two angles α, β and the two scalings g_{BDO1} between the DOF1 and BDO1rot axes, and g_{BDO3} between the DOF2 and BDO3rot axes.



(a) The alignment parameter space.

(b) The error signal for different alignments. 8.5° separation angle.

(c) The feedback signal for different alignments. 10 dB gain difference.

Figure 5.24: Effect of a gain hierarchy on feedback signals for a small actuator separation angle. The values of 8.5° separation angle and 10 dB gain difference are similar to the actual values. One example misalignment and its transformations are marked.

5.4.7 BDO mirror suspension upgrade

After the implementation of the OMC the 80 Hz to 300 Hz region showed a considerable and unexpected increase in noise (see fig. 5.25). Investigations showed several indications that this noise was caused by resonances in the BDO suspensions.

Amongst these indications were:

- **Acoustic injections near the output optics increased the noise in the 80 Hz to 300 Hz region.** Fig. 5.26 shows that white noise acoustic injections via loudspeaker near the TCOb tank increased the noise in the 80 Hz to 300 Hz region.
- **Improved isolation of the OMC above 50 Hz, via additional fluorubber pads directly under the OMC, did not reduce the 80 Hz to 300 Hz region.** This indicates that the decreased sensitivity is not due to movement of the OMC itself.
- **Use of a signal-recycling mirror with lower reflectivity increased the 80 Hz to 300 Hz region.** As described in section 5.5 reduction of the reflectivity of the signal-recycling mirror increases the higher-order mode content of the beam leaving the interferometer. The higher-order modes of order $TEM_{01/10}$ can be converted back into the fundamental mode (of the OMC) by alignment fluctuations of the BDO mirrors. Fig. 5.27 indicates that this conversion is fluctuating with frequencies in the 80 Hz to 300 Hz region.
- **Individual features of the 200 Hz forest showed up in measurements of the rotation of BDO1 and BDO2 via an optical lever.** We looked into the signals of the *quadrant photodiode* (QPD) in transmission of BDO3. Since the distance between this QPD and BDO1 and BDO2 is approximately 3.5 m and 2 m respectively this sensor has a good sensitivity for angular fluctuations of these mirrors. We can see in fig. 5.28 a peak at 174.3 Hz in both the strain signal and the vertical optical lever signal.
- **Vibration measurements on top of the BDO1 and BDO3 suspension show resonances matching those observed in the strain measurement.** Given the indications above we decided to vent the TCOa and TCOb tanks. We placed a PZT onto different positions of the common BDO1 and BDO3 suspension, as shown in fig. 5.31. This showed several resonances in the frequency region of the 200 Hz forest as shown in fig. 5.29.

This led us to improve the BDO suspensions. BDO1 and BDO3 are located in the TCOb tank and are attached to a common suspension (see fig. 5.31). We replaced this suspension with the more sturdy suspension designed at Glasgow University and shown in fig. 5.32. We added four 10 by 10 by 10 mm³ fluorubber (fluorel[®]) pads under the suspension of BDO2, visible in fig. 5.30. The benefit from this suspension is evident in fig. 5.33.

We used the opportunity to install PZT actuators (Physik Instrumente P-025.80P), PZT vibration sensors (Physik Instrumente P-876.SP1), and custom-made capacitive sensors on top of the new suspension to allow for more direct vibration measurements in the future.

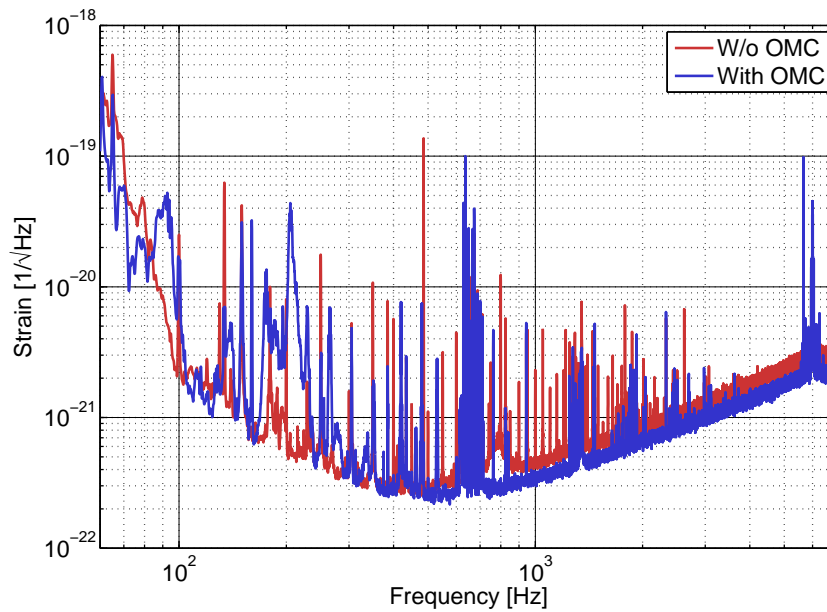


Figure 5.25: GEO 600 sensitivity with and without OMC. Notice the increase in noise in the 80 Hz to 300 Hz region. The improvement above 500 Hz with OMC is due to the reduction in shot noise due to the attenuation of HOMs and SBs by the OMC.

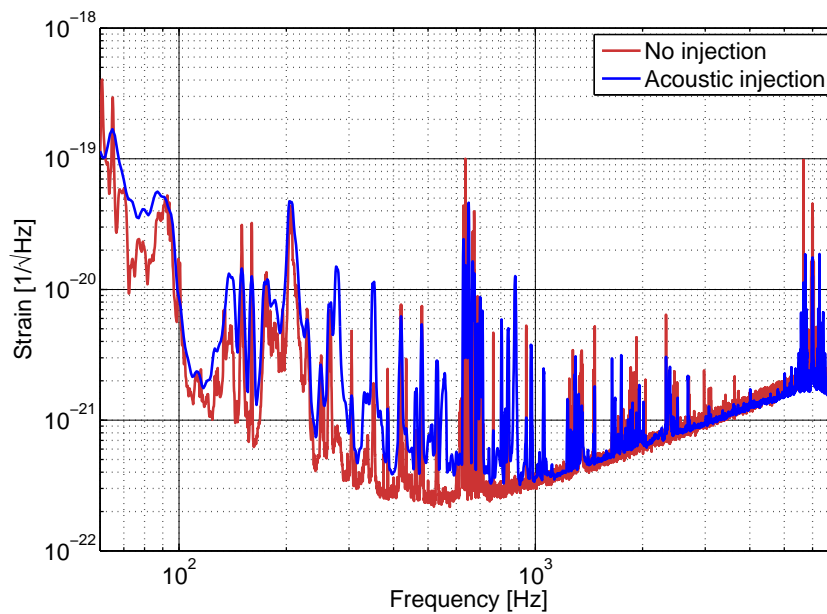


Figure 5.26: Effect of acoustic white noise injection near TCOB onto GEO 600's sensitivity.

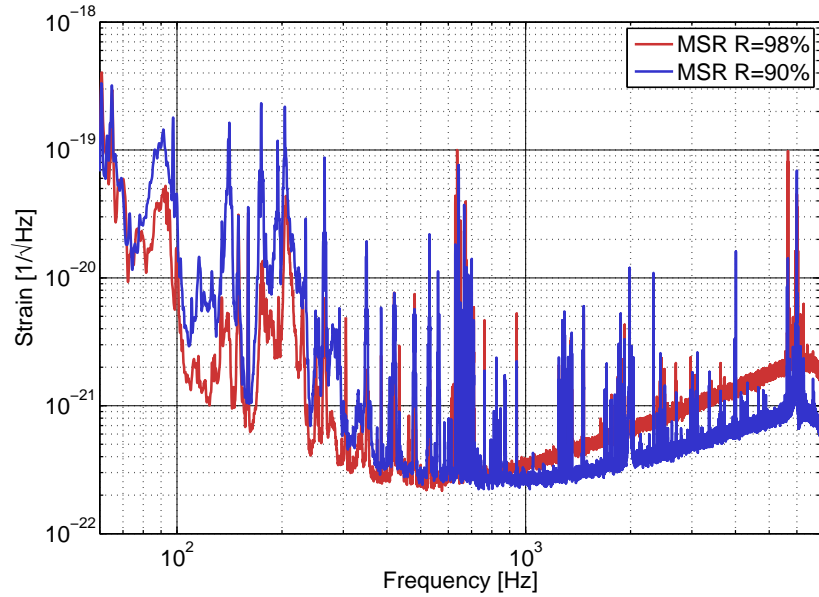


Figure 5.27: Effect of the signal-recycling mirror reflectivity on the sensitivity. Notice the increased noise in the 80 Hz to 300 Hz region. The improved sensitivity is due to reduced shot noise as detailed in section 5.5.

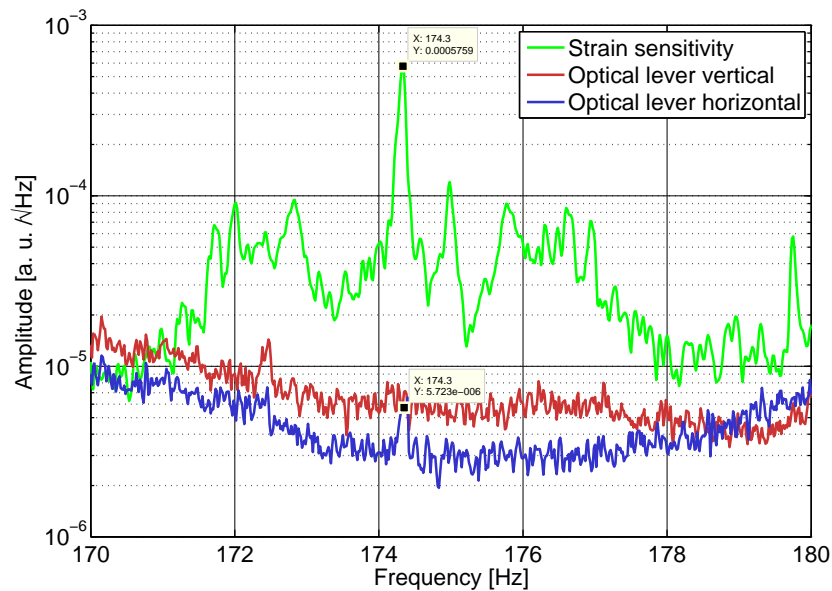


Figure 5.28: Optical lever measurement behind BDO3. Mind the line at 174.3 Hz in both the sensitivity and the optical lever signal.

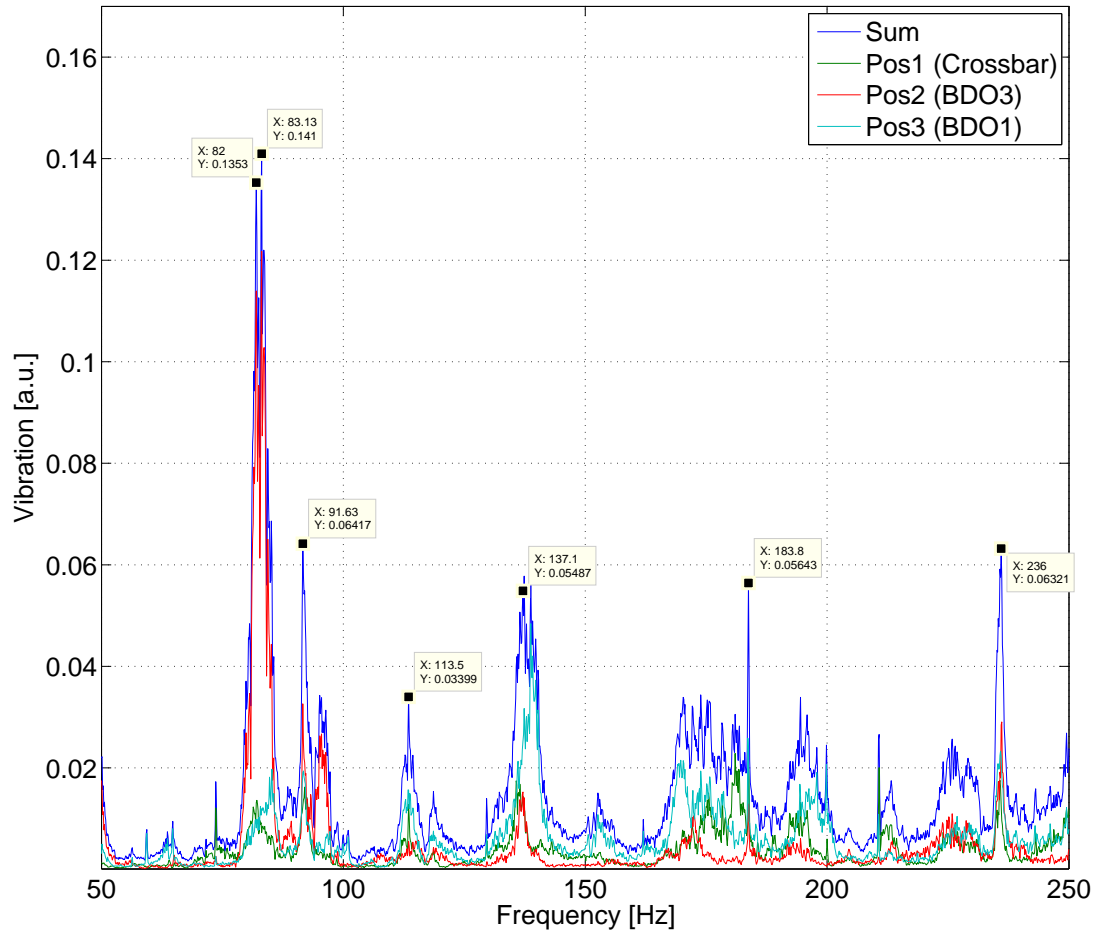


Figure 5.29: Measurement of vibrations on the original suspension in TCOB. Positions marked in fig. 5.31.

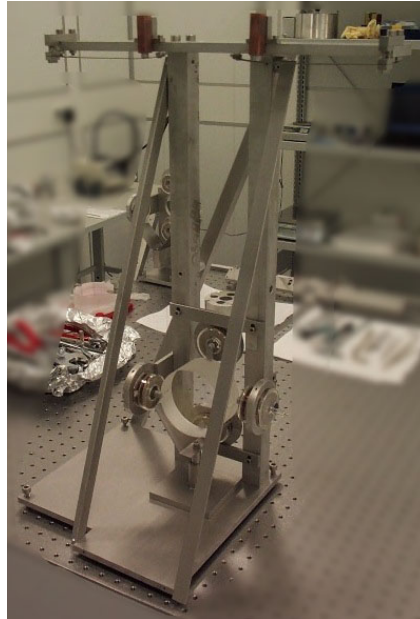
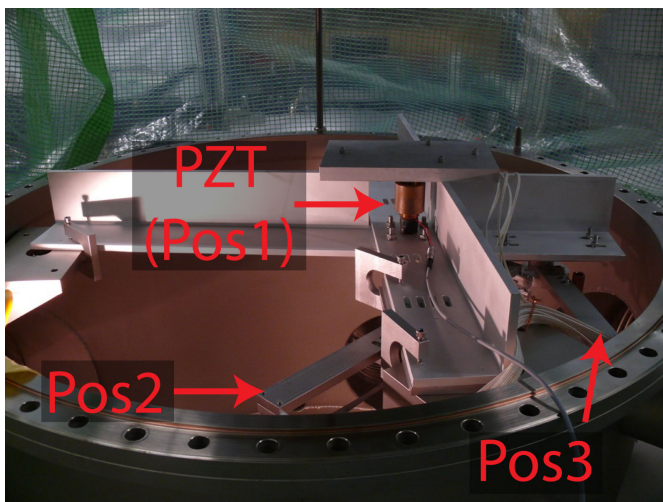


Figure 5.30: Model of the BDO2 suspension in the AEI cleanroom.



(a) Suspension built into TCOB. Notice the PZT for vibration measurements. Pos = Position



(b) Suspension test model in the AEI cleanroom.

Figure 5.31: Original suspension of BDO1 and BDO3.

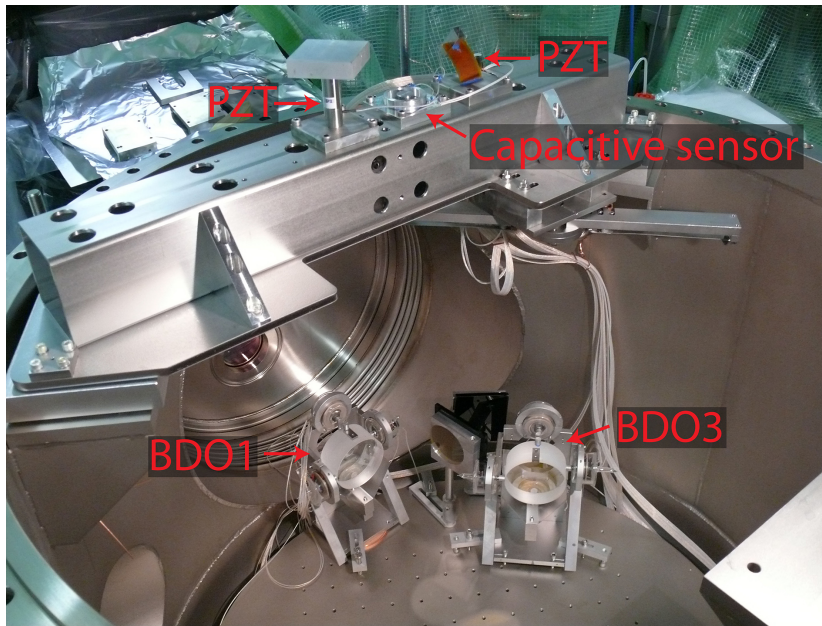


Figure 5.32: Upgraded suspension of BDO1 and BDO3, as built into TCOB.

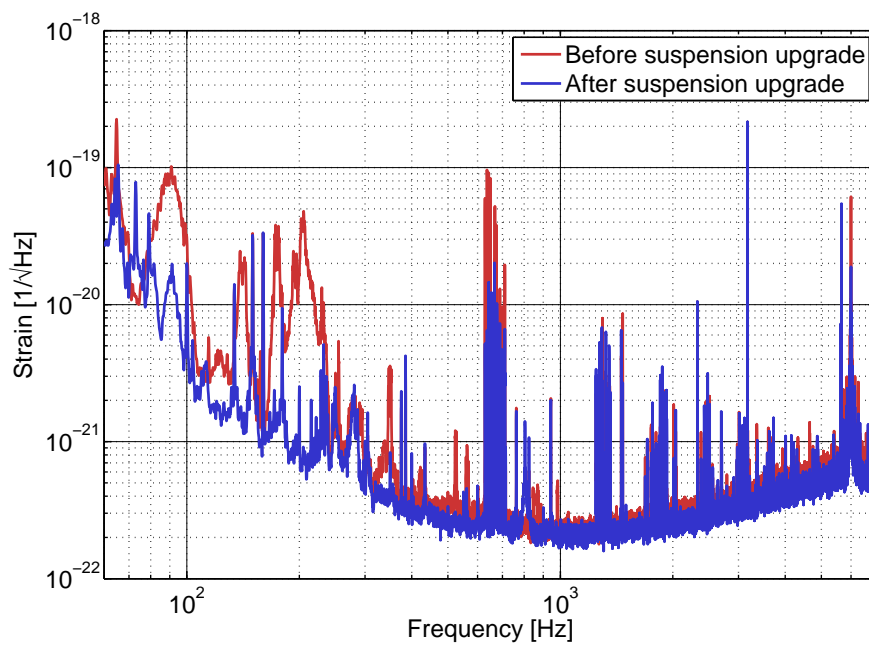


Figure 5.33: Effect of the BDO suspension upgrade. The excess noise in the 80 Hz to 300 Hz region is almost entirely eliminated by the upgrade.

5.5 Effect of signal-recycling configuration change on the output mode cleaner

In November 2010 we exchanged the signal-recycling mirror, reducing its reflectivity from 98 % to 90 %. As described in section 4.1 this widened the signal-recycling cavity's bandwidth and thereby improved GEO 600's shot noise limited sensitivity at frequencies above 400 Hz. This change greatly reduced the quality of the interferometer's output beam (see fig. 5.34). This proved to be challenging for the OMC automatic alignment control system.

We analyzed the mode content of the interferometer's output beam by scanning the OMC length over 1 FSR. We found a strong increase in HOM content with the new signal-recycling mirror, as presented in fig. 5.35. We matched the peaks in the OMC scan to SBs and HOMs based on eq. 5.12 which are adaptations of eqs. 3.4c-3.4e for a cavity with two foci per round-trip, such as the OMC.

$$\phi_{\text{gouy,HG}} = 2(m + n + 1) \arctan\left(\frac{l_{\text{rt}}/2}{z_R}\right) \quad (5.12a)$$

$$\phi_{\text{gouy,LG}} = 2(2p + l + 1) \arctan\left(\frac{l_{\text{rt}}/2}{z_R}\right) \quad (5.12b)$$

which for $z_R \approx 0.595$ m leads to a phase shift of $\phi_{\text{gouy}} = 0.16$ FSR for $\text{HG}_{01/10}$ or LG_{01} modes. The main peak at 0.38 FSR is therefore due to $\text{HG}_{02/11/20}$ or $\text{LG}_{10/02/0-2}$ modes.

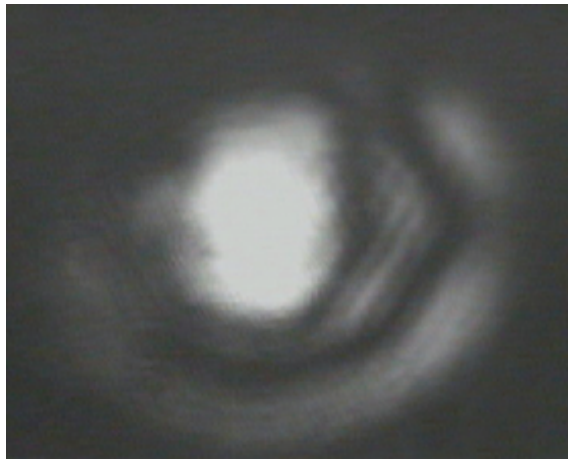
When we compare the corresponding mode shape to fig. 3.1b we see that its intensity distribution matches that of the LG_{02} mode. Since both Hermite-Gaussian and Laguerre-Gaussian modes form a complete basis of any beam shape a LG_{02} mode can be expressed in HG modes as presented in eq. 5.13 [OC00].

$$\psi_{02}^{\text{LG}} = \frac{1}{2}\psi_{20}^{\text{HG}} + \frac{1}{\sqrt{2}}\psi_{11}^{\text{HG}} - \frac{1}{2}\psi_{02}^{\text{HG}} \quad (5.13)$$

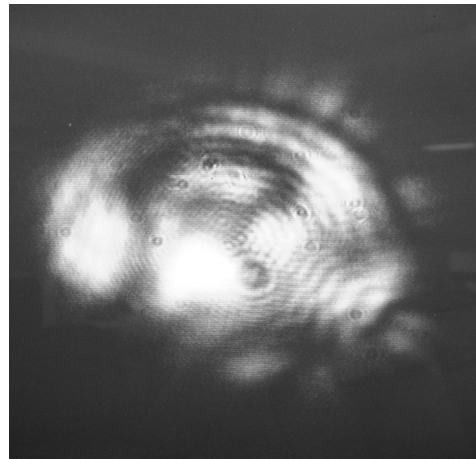
We expected an increase in $\text{HG}_{02/20}$ mode content due to reduced mode-healing with the new MSR as presented in section 4.2.

The asymmetry of the transmission peaks corresponding to the SBs is consistent with additional contributions to the bigger SB's appearance by HOMs of order 6. If we average the measured value of the mode spacing of 0.16 FSR and the measured mode spacing of 0.19 FSR, as measured at the second order HOMs, the resulting mode spacing is 0.175 FSR. Sixth order HOMs are then expected at 1.02 FSR. Since any measurement of the mode spacing is modulo 1 FSR this agrees well with the position of the bigger SB at 0.035 FSR.

It is important to remember that the OMC can *not* be considered as a completely independent measurement device of the interferometer's output beam. As described in section 3.5 misalignments and errors in mode-matching lead to couplings between HOMs and the fundamental mode. The importance of this effect can be judged by the following criterion: For the range of errors in alignment and mode-matching that occur in the



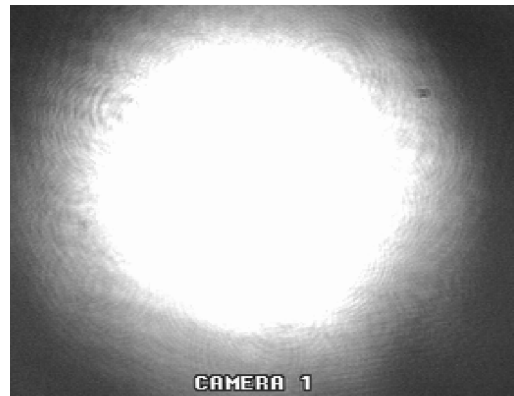
(a) Beam profile with the old ($R = 98\%$) signal-recycling mirror.



(b) Beam profile with the new ($R = 90\%$) signal-recycling mirror.



(c) Beam profile with the old signal-recycling mirror, behind the OMC.



(d) Beam profile with the new signal-recycling mirror, behind the OMC.

Figure 5.34: The interferometer's output beam profile with the old and the new signal-recycling mirror, and the beams in transmission of the OMC. The interferometer was in the configuration to measure GWs, especially a $DFO \neq 0$ was set.

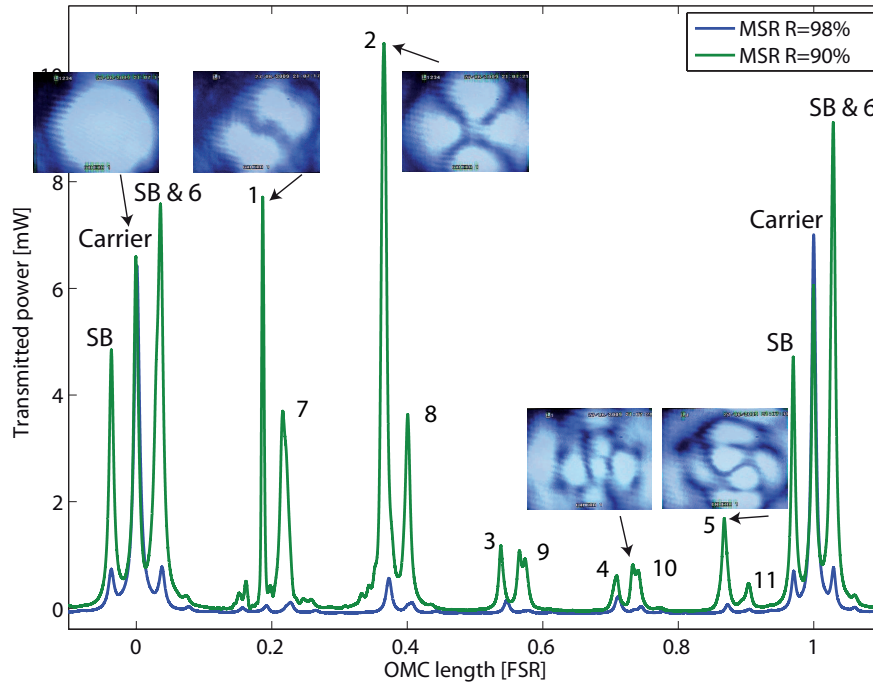
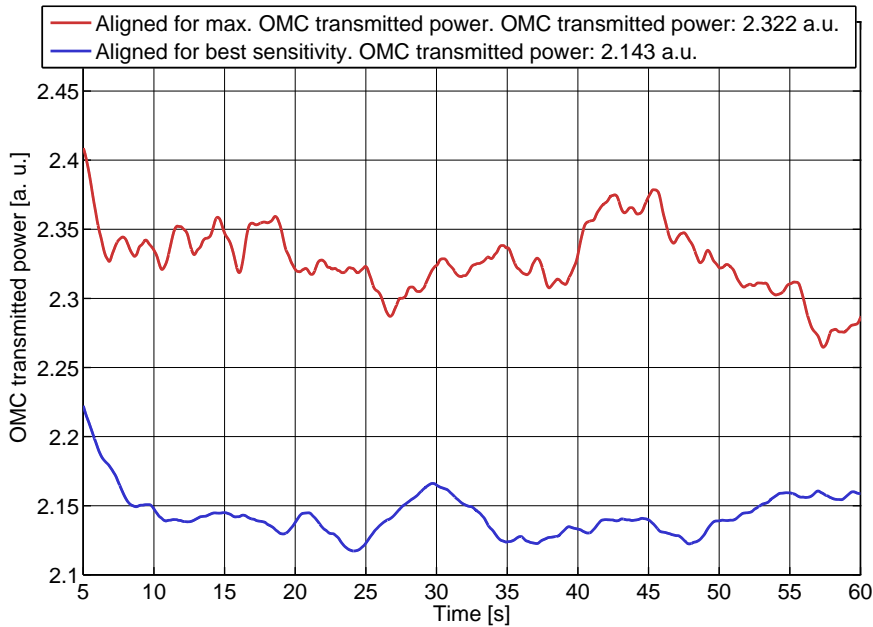


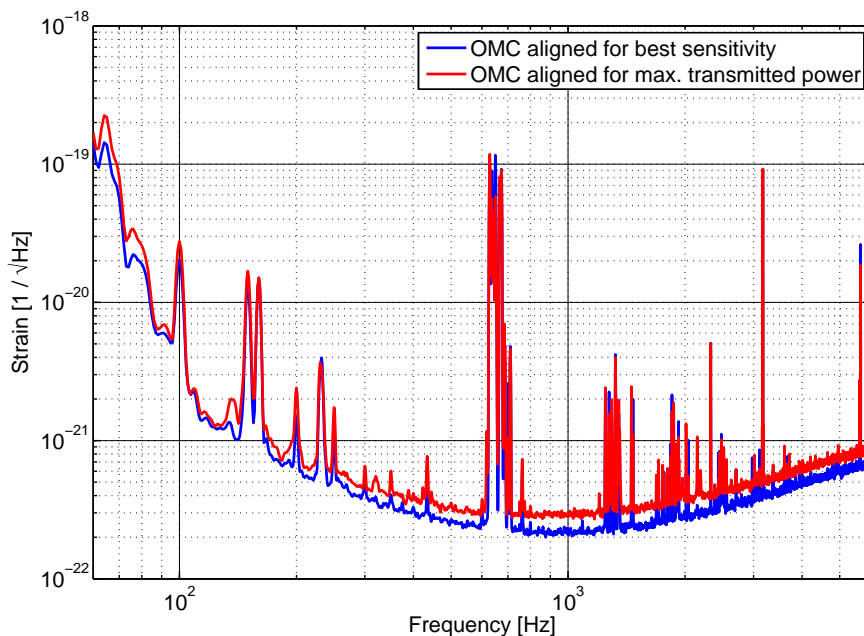
Figure 5.35: Interferometer’s output beam components as measured via a scan of the OMC length. The photographic insets show the mode resonating inside the OMC, pictured in transmission of the OMC mirror with a transmission of 0.01 % (see fig. 5.3). The numbers indicate the order of the optical modes.

normal operation of the OMC, is there a combination of these errors that leads to more OMC transmitted power than perfect alignment and mode-matching would? After the exchange of the signal-recycling mirror this was the case. An illustration of this effect is shown in fig. 5.36 showing that maximizing the OMC transmitted power is leading to a sub-optimal strain sensitivity of GEO 600. Since the OMC alignment control system essentially tries to maximize power transmitted by the OMC, this effect contaminated the alignment error signals. This contamination was so strong that GEO 600’s sensitivity was severely compromised on a minute time-scale by misalignment of the OMC as presented in fig. 5.37. Since the DFO of the interferometer is locked to the OMC transmitted power, this effect also compromised the interferometer’s stability, prohibiting locks beyond a few hours. To alleviate this problem we switched in March 2011 to the beacon alignment control system described in the following subsection.

Keeping the limitations described above in mind we calculated the M^2 parameter of the interferometer’s output beam using the OMC as a beam analyzer. The result presented in table 5.5 should give the reader an impression of when mode-conversion effects can become significant.



(a) OMC transmitted power for different alignment states. Filtered by a second order low-pass filter at 0.1 Hz.



(b) Corresponding strain sensitivities of GEO 600.

Figure 5.36: Illustration of the difference between maximizing the OMC transmitted power and optimizing GEO 600’s strain sensitivity. The OMC was locked onto the carrier. The alignment onto the OMC that maximizes the OMC transmitted power results in a sub-optimal sensitivity. For the comparison of the OMC transmitted powers the interferometer was locked onto the quadrant photodiode in transmission of BDO1 that was described in subsections 5.4.4.

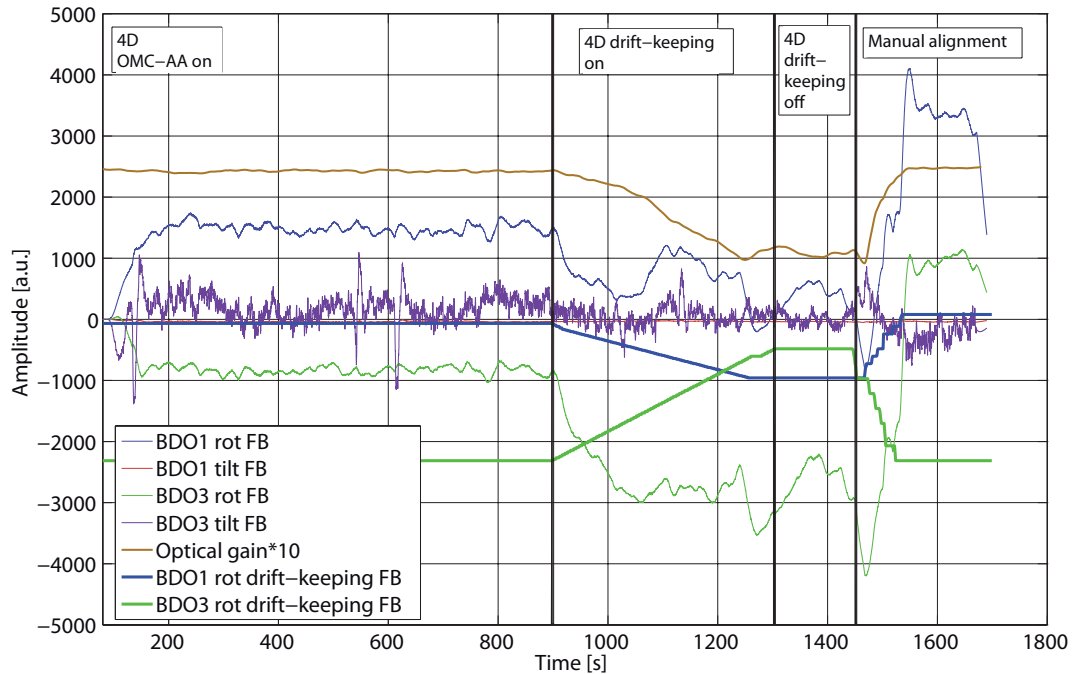


Figure 5.37: Detrimental effect of the original alignment control after the signal-recycling mirror change. Points in time at which the configuration is changed are marked by the black vertical lines. Immediately after the control loop gain at very low frequencies is increased, by activation of the drift-keeping FBs, the optical gain decreases. Manual alignment was done by adjusting the drift-keeping FBs. The other FBs were not applied during the manual realignment.

5.5.1 Beacon alignment control

In March 2011 we switched to the beacon alignment control scheme, in which we marked the GW-carrying beam component of the interferometer's output beam and have the alignment control system maximize the transmission of that component. We reduced the alignment control to only act on BDO1 leaving the BDO3 DOFs uncontrolled for simplicity. When we limit our discussion to audio band frequencies, the interferometer's output beam consists of components at the carrier frequency i.e. at DC, and SBs created by fluctuations in the difference of the interferometer's arm lengths. These audio-band SBs are in the same optical mode as the GW signal, since differential arm length fluctuations are exactly the effect GWs cause. By artificially raising the level of these SBs we created a so-called beacon which allows the alignment control system to maximize the transmission

Table 5.10: Mode content of the interferometer’s output beam as measured using the OMC as a beam analyzer. Mind that this measurement is only an approximation due to mode-conversion effects described in section 3.5. M^2 calculation according to eq. 3.3.

Mode order N	MSR $R = 98\%$	MSR $R = 90\%$
	Power in the mode [mW]	
0	6.81	6.32
1	0.14	7.71
2	0.65	10.59
3	0.24	1.17
4	0.31	0.61
5	0.16	1.67
6		3.56
7		3.70
8		3.63
9		1.08
10		0.81
11		0.47
Sum [mW]	8.3	41.3
M^2	1.5	4.5

of the GW-carrying optical mode. Following the argumentation in [SLBE⁺11] the power in transmission of the OMC in presence of a beacon is

$$E_{\text{Beacon}} = P(f_d + f_b) \propto 2sc\Theta_c + 2cs\Theta_s \quad (5.14)$$

with

- E = Alignment error signal
- $P(f)$ = Power in transmission of the OMC at frequency f
- f_b = Beacon frequency
- f_d = BDO dither frequency
- s = Amplitude of the beacon SBs
- c = Amplitude of the carrier light
- Θ_c = Misalignment of the carrier
- Θ_s = Misalignment of the beacon

A dither alignment control system that demodulates the OMC transmitted power twice, first at f_b , then at f_d will act to maximize $P(f_d + f_b)$.

When we compare the beacon alignment control (eq. 5.14) to the original alignment control without beacon (eq. 5.15), we see that the beacon alignment technique is 50 % less susceptible to the alignment of light at the carrier frequency. The beacon alignment control system's error signal is therefore composed to 50 % of the correct error signal and to 50 % of an error signal that might be contaminated by mode-conversion effects.

$$E_{\text{Original}} = P(f_d) \propto 2c^2\theta_c + 4s^2\theta_s \stackrel{s \approx 0}{\approx} 2c^2\theta_c \quad (5.15)$$

We decided on a frequency of 3170 Hz for the beacon modulation which is well in the shot noise limited frequency region, far off of multiples of the mains frequency of 50 Hz, and far off the OMC mechanical modes' frequencies presented in table 6.2. This provided us with a signal against a white noise background. The modulation was applied using the *electrostatic drive* (ESD) actuators directly attached to the MCE and MCN mirrors and their reaction masses. The resulting signal in the calibrated strain measurement was then calculated, following eq. 1.6, to a displacement amplitude of $194 \cdot 10^{-18}$ m. The BDO mirrors' dither parameters are presented in table 5.11. Their dither frequencies were reduced to allow for bigger dither amplitudes. The alignment error signals were then generated by demodulating the OMC transmitted power first at 3170 Hz and then the resulting signal was demodulated at the respective BDO dither frequencies. The demodulation phases were tuned by hand.

The error signal validity was checked by comparing the error signal to the intrinsic noise of the system. The intrinsic noise level is present in the system even when there is no valid error signal.¹ The signals are valid up to frequencies where the error signals converge with the intrinsic noise (see fig. 5.38 and table 5.12). This measurement depends on the alignment state of the OMC, since a bigger misalignment results in a bigger error signal. The measurement was done with a manually well aligned OMC, and is therefore representative of the nominal alignment state. The OLGs of the alignment control loops

Table 5.11: Beacon alignment BDO dither parameters.

Degree of freedom	Dither freq. [Hz]	Dither ampl. [μ rad]
BDO1 rotation	17	7.3
BDO1 tilt	11	11.5

¹ Intrinsic noise is often referred to as dark noise since a common occurrence of intrinsic noise is the readout of a photodiode with no light impinging on it. We prefer the less used but more general term intrinsic noise here.

are depicted in fig. 5.39 and respective properties are presented in table 5.12. The high UGFs of the control loops allow for fast responses of the control loops in case of strong misalignments. The OLGs were measured as step responses by introducing a static misalignment to the respective DOFs and measuring the time it took the alignment system to reach 63.2% its steady-state FB signal. For the used OLG shape this time span equals $1/\text{UGF}$.¹ The known loop shape was then fitted to this value. We limited the alignment control to the BDO1 DOFs leaving the BDO3 DOFs uncontrolled to simplify the system.

The beacon alignment system allowed for a stable operation of GEO 600, with its longest lock exceeding 35 hours. Switching, with GEO 600 in lock, from the original alignment control system to the beacon alignment control system immediately improved GEO 600's sensitivity as measured in the optical gain (see fig. 5.40).

The optical gain is one of two parameters describing the coupling between differential arm length fluctuations and signal on the photodiode used to detect GWs. This coupling has the form of a first order low-pass due to the non-negligible light storage time of the PRC. The optical gain is the DC gain of this low-pass and the second parameter describing the coupling is the frequency at which the low-pass filter reaches an attenuation of 3 dB.

The beacon alignment scheme alleviates the problem of error signal contamination by 50%, but does not completely eliminate it. To further improve the alignment onto the OMC we implemented the so-called optimal beacon alignment control system, described in the next subsection, in June 2011. This system should theoretically completely eliminate the error signal contamination [SLBE⁺11].

5.5.2 Optimal beacon alignment control

In June 2011 we switched to the so-called optimal beacon alignment control. This alignment control acts on BDO1 and BDO3 and so controls all 4 DOFs. The optimal beacon alignment technique combines different measurements to produce an alignment error signal that is not contaminated by mode-conversion effects at the carrier light frequency, as presented

Table 5.12: Beacon alignment loop characteristics.

Degree of freedom	UGF [mHz]	DC-gain [dB]	Error signal valid to freq. [mHz]
BDO1 rotation	15	24	3.5
BDO1 tilt	300	60	3

¹ The evaluation of a step response depends on the shape of the OLG. The described evaluation is valid for an OLG created by an integrator with feedback, which is a good approximation of the alignment control loops OLGs' shapes.

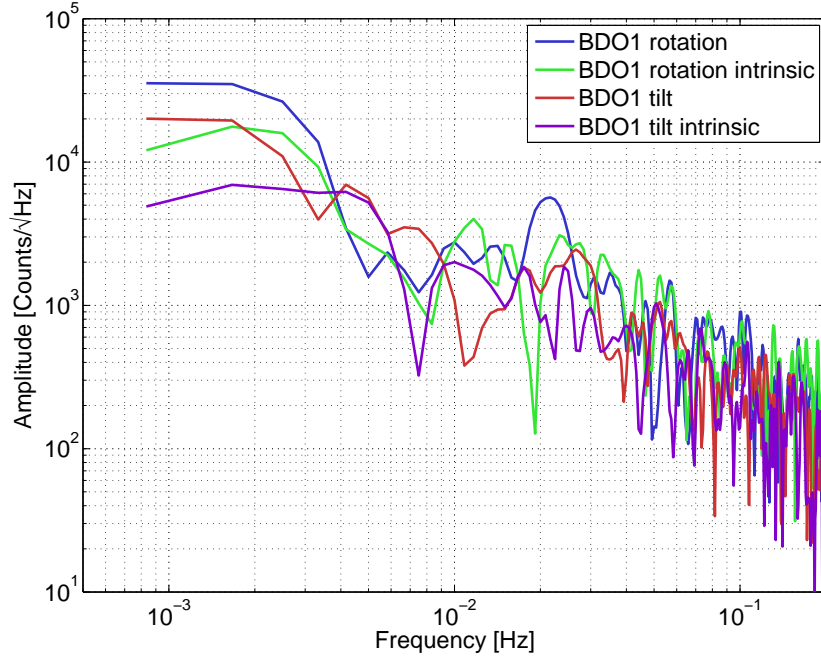


Figure 5.38: Spectral density of the beacon alignment's error signals for good alignment of the OMC. A DOF's error signal is valid up to the frequency where it converges with the alignment system's intrinsic noise in that DOF.

in eq. 5.16.

$$E_{\text{Optimal}} = E_{\text{Beacon}} - \frac{P(f_b)}{2P(\text{DC})} E_{\text{Original}} \quad (5.16a)$$

$$= 2cs\theta_s + 2sc\theta_c - \frac{2cs}{2c^2} \propto 2cs\theta_s \quad (5.16b)$$

The parameters of the optimal beacon alignment control loops are presented in tables 5.13,5.14. A gain hierarchy was implemented by only creating LV control loops for the BDO1 DOFs. This provides infinite gain for the BDO1 DOFs at very low frequencies. As with the beacon alignment we checked the frequencies up to which the error signals are valid (see fig. 5.41).

When we compare the optical gain with the beacon alignment control and the optimal beacon alignment control there is no appreciable difference as presented in fig. 5.43. To evaluate the effectiveness of the optimal beacon technique we decided to intentionally increase the HOM content in the interferometer's output beam by changing the ROC of the MFE mirror. In nominal operation a heating element behind MFE emits 90 W of heat that deform MFE to the desired ROC of approximately 660 m. We reduced the heating power to 65 W which results in a ROC of MFE of approximately 650 m according to simulations carried out with the ANSYS [ANS12] *finite element method* (FEM) simulation

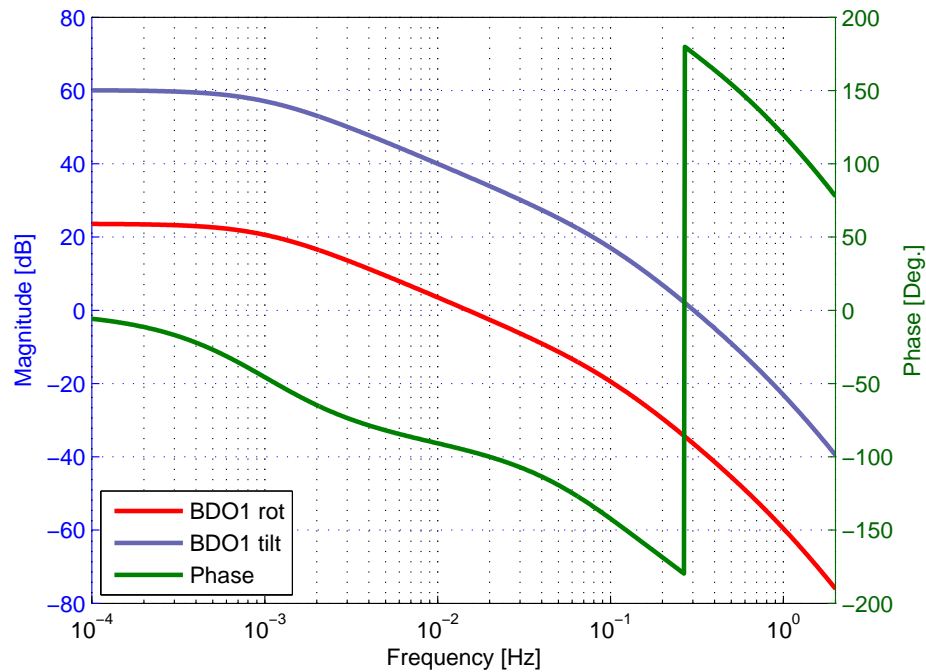


Figure 5.39: OLG of the beacon alignment control. The known loop shape was fitted to the measured UGFs.

Table 5.13: Optimal beacon alignment BDO dither parameters.

Degree of freedom	Dither freq. [Hz]	Dither ampl. [μ rad]
BDO1 rotation	17	7.3
BDO1 tilt	11	11.5
BDO3 rotation	3.5	114.0
BDO3 tilt	14	7.1

Table 5.14: Optimal beacon alignment loop characteristics. The shape of the OLG is identical to that of the beacon alignment control depicted in fig. 5.39.

Degree of freedom	UGF [mHz]	DC-gain [dB]	Error signal valid to freq. [mHz]
BDO1 rotation	3	10	7
BDO1 tilt	17	25	4
BDO3 rotation	3.5	11	10
BDO3 tilt	1.5	5	2

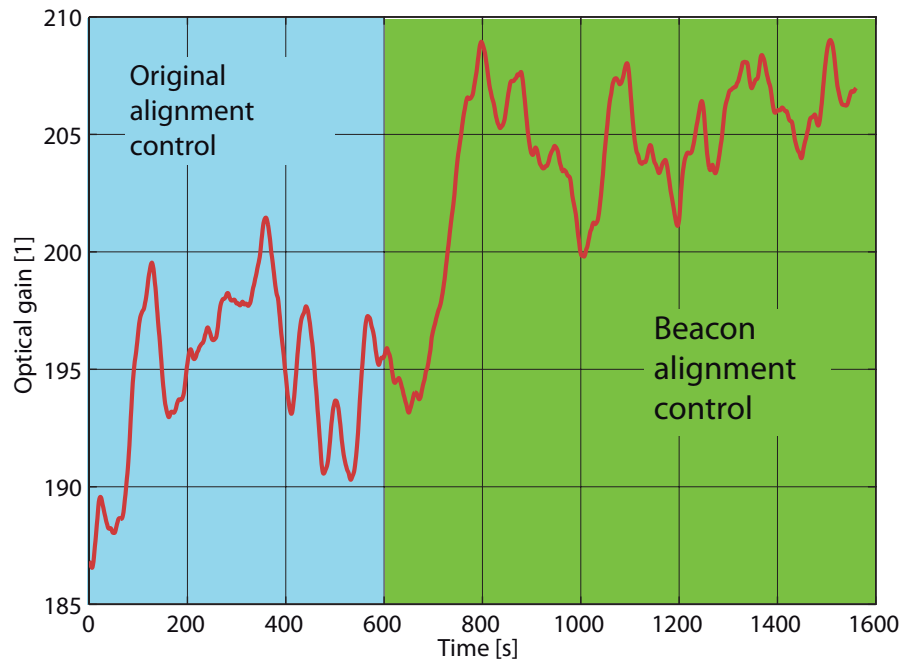
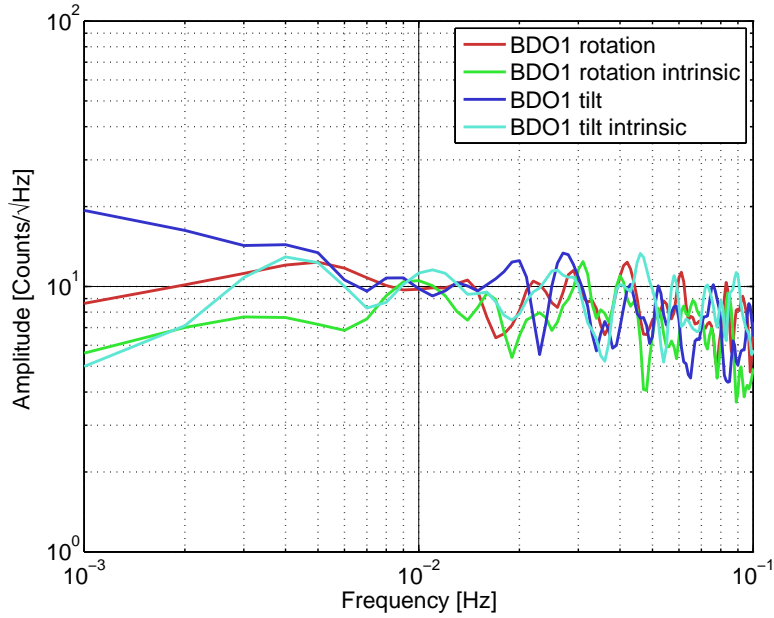


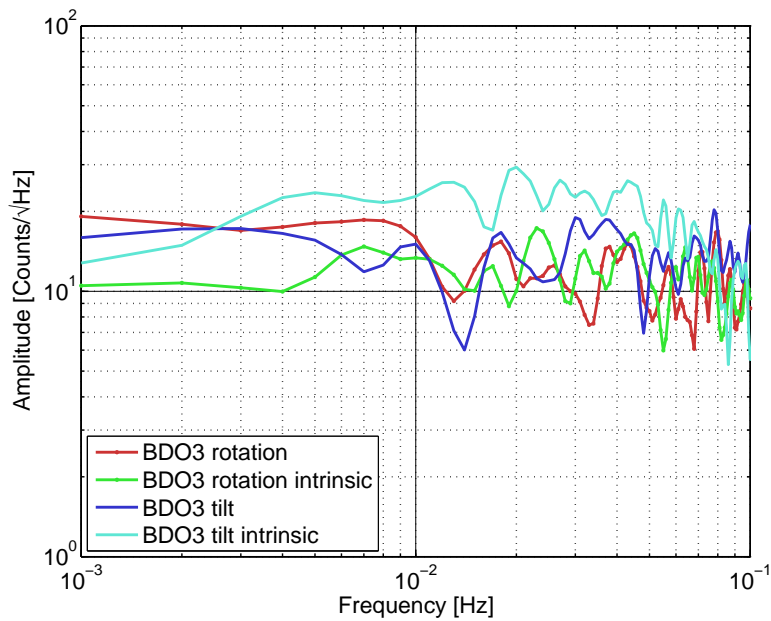
Figure 5.40: Optical gain improvement by the switch from the original alignment control system to the beacon alignment control system.

package [Wit12]. This creates an imbalance in the ROCs of MFE and MFN and increases the content of second order HOMs as depicted in fig. 5.42. Even with this no benefit of the optimal beacon is apparent, as shown in fig. 5.44. Further investigations might reveal benefits of the optimal beacon for high power in other HOMs. The change in optical gain between fig. 5.40 and figs. 5.43,5.44 is due to changes in the configuration of GEO 600, not due to changes in the OMC alignment system.

As eqs. 5.14 and 5.16 show the beacon and optimal beacon error signals scales linearly with the power of the beacon sidebands in transmission of the OMC. This power in turn depends quadratically on the displacement amplitude. Increasing the beacon's displacement amplitude therefore increases the error signal's amplitude quadratically. A way to increase the beacon's dither amplitude beyond the current level is to excite the internal 'drum' modes of GEO 600's main mirrors at approximately 15 kHz. The shape of these modes is depicted in fig. 5.45. Excitations at these frequencies have not yet been employed. Firstly, because frequencies above 8192 Hz are not accessible to GEO 600's pre-existing data acquisition system which reduces the amount of diagnostic tools for such frequencies greatly. Secondly, the frequencies of the internal modes are not static and change due to e.g. changes in temperature. An excitation of the internal modes would therefore have to follow the internal modes' frequencies.



(a) Error signal for the BDO1 mirror.



(b) Error signal for the BDO3 mirror.

Figure 5.41: Spectral density of the optimal beacon alignment's error signals. An DOF's error signal is valid up to the frequency where it converges with the alignment system's intrinsic noise in that DOF.

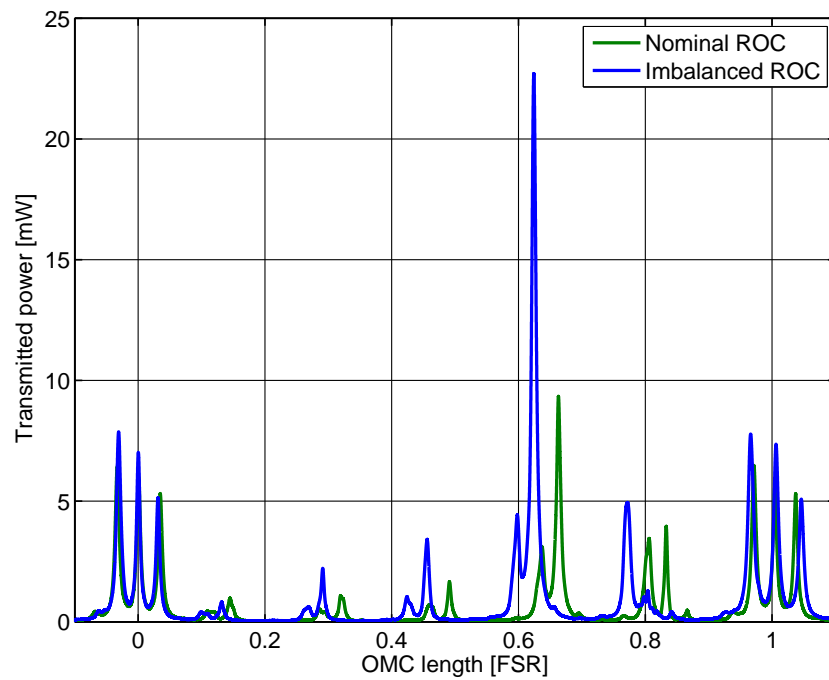


Figure 5.42: Interferometer's output beam components as measured via a scan of the OMC length. The ROC of the mirrors in the interferometer's arms was intentionally imbalanced. The offset in the position of the modes is due to nonlinearities of the PZT used to scan the OMC. As in fig. 5.35 the main peak is due to second order HOMs.

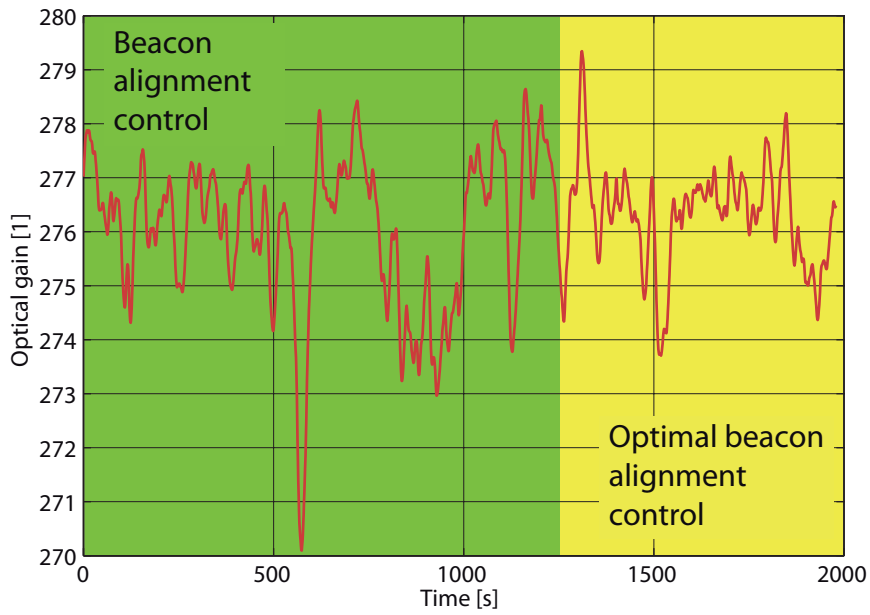


Figure 5.43: No appreciable change in the optical gain was detectable at the switch between the optimal beacon and ‘ordinary’ beacon alignment method.

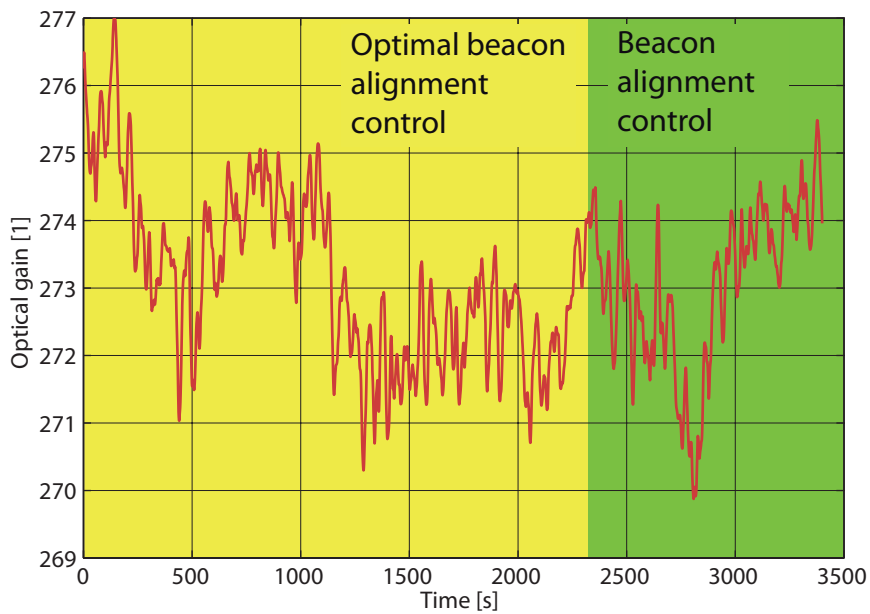
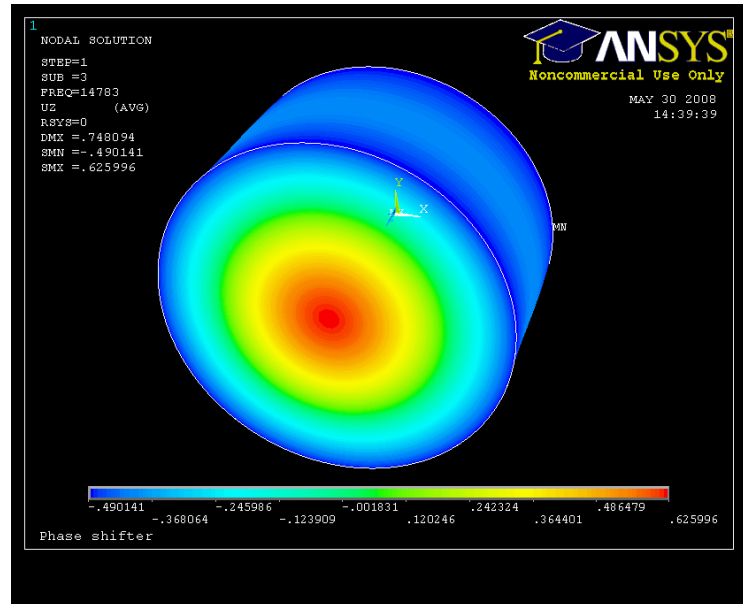
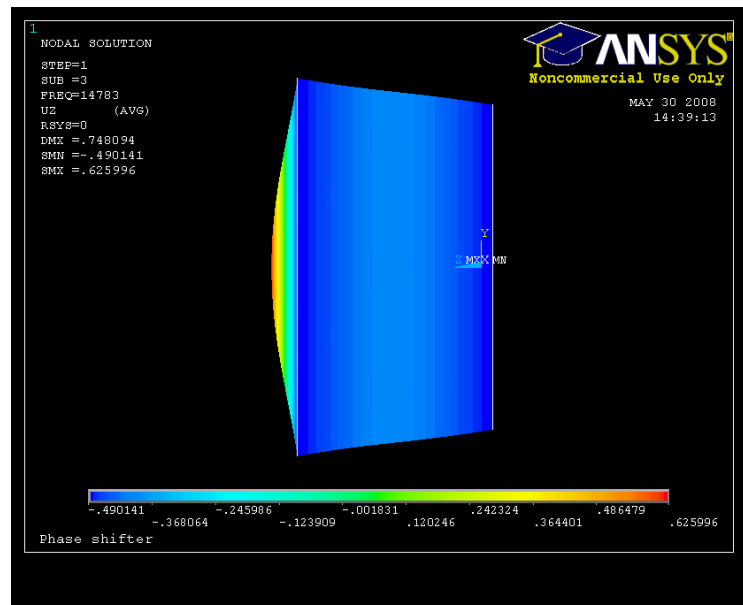


Figure 5.44: No appreciable change in the optical gain was detectable at the switch between the optimal beacon and ‘ordinary’ beacon alignment method even with intentionally increased HOM content in the interferometer’s output beam.



(a) Isometric view.



(b) Side view.

Figure 5.45: Drum mode of GEO 600's main mirrors as simulated with ANSYS.

6 Experiences with the output mode cleaner

A GW detector such as GEO 600 is more complex than most physics experiments. This is mainly due to the fact that a multitude of different properties are coupled mechanically, optically, or via control systems. The addition of a subsystem, such as the OMC, therefore requires careful evaluation of its performance. In the following sections we present noise projections that allow us to evaluate some of the noise introduced to the GW measurement by the OMC. We also present the results of our investigations into the optical properties of the OMC itself. Furthermore we present an example of GEO 600's use for measurements not related to GW detection in which we estimate an upper limit to the internal displacement noise performance of a PZT actuator.

6.1 Noise projections

Noise projections offer a way to estimate the contributions of different noise sources to a compound noise floor. Noise sources can either be external sources or detector subsystems. Noise projections are a two stage process. The *first* stage is the noise injection. The noise in the noise source of interest, e.g. laser amplitude noise, is elevated so that it dominates the noise floor of the measurement of interest, e.g. the strain measurement in a GW detector. Evidence for this is an elevation of the noise floor in coincidence with the noise injection. In this stage a transfer function, the noise coupling, can be estimated between the noise source and the measurement of interest. In the *second* stage the noise is no longer artificially elevated. In the nominal operation state the noise in the source of interest (e.g. the level of laser amplitude noise) is measured and the previously estimated transfer function is applied to estimate this noise source's contribution to the noise in the measurement of interest. This procedure assumes a linear behavior of the noise coupling in both frequency and amplitude. For example it assumes that noise injected at one frequency appears in the measurement of interest at the same frequency, and it assumes that the transfer function stays constant for different levels of noise. A thorough discussion of noise projections can be found in [Smi06].

A special case is the projection of the OMC resonance coupling. In this we look at GEO 600's sensitivity with the OMC intentionally slightly offset off of the optimal length for resonance of the fundamental mode of the carrier. This introduces sharp noise peaks into GEO 600's sensitivity. We attribute these to peaks in OMC length fluctuations. Their coupling to strain depends on the offset of the OMC to the resonance of the fundamental mode of the carrier light. A measure for this offset is the height of the 6 kHz OMC length dither line. Details of this dither line are presented in subsection 5.3.2. So in the projection

of the OMC resonance coupling we use a varying transfer function for an assumed static noise source, whereas it is the other way around for the other noise projections.

In GEO 600 we update the noise coupling transfer functions every few months, or whenever a considerable change to the detector's configuration was made. Knowledge of the noise couplings allows for the subtraction of technical noises from the strain measurement, a procedure currently not used at GEO 600.

In fig. 6.1 we present the noise projection to GEO 600's strain measurement. The noise contributions related to the OMC are *OMC long. FB* and *OMC resonances*. OMC long. FB projects the feedback noise due to the OMC longitudinal control loop. The coherence between the injected noise and the strain measurement is low for this noise, indicating an impaired quality of the noise projection. This is consistent with expectations since, as was discussed in subsection 5.3.2, a well controlled OMC length leads to a frequency doubling between fluctuations in the OMC length and the resulting fluctuations in the OMC transmitted power. Such nonlinear behavior is not accessible for noise projections. A measurement of the cross-bicoherence during noise injection however shows no apparent frequency doubling effect. The fact that a noise injection into OMC longitudinal FB degrades GEO 600's strain sensitivity only when the noise level is raised by approximately a factor of 50 above the nominal level indicates that OMC longitudinal FB is not limiting GEO 600's sensitivity (see fig. 6.2).

OMC resonance coupling projects the noise due to resonances in the OMC length fluctuations. We simulated the OMC mechanical modes using the ANSYS simulation package. The frequencies of the first 15 modes are presented in table 6.2. The shapes of these modes are presented in appendix A. A comparison of the simulated resonance frequencies in table 6.2 and the measured resonance frequencies in fig. 6.3 indicates that resonances exist in the frequency region predicted by the simulation. The resonance frequencies however do not exactly match and the structure in the projection is more complex than in the simulation, indication that the full complexity of the situation was not captured in the simulation.

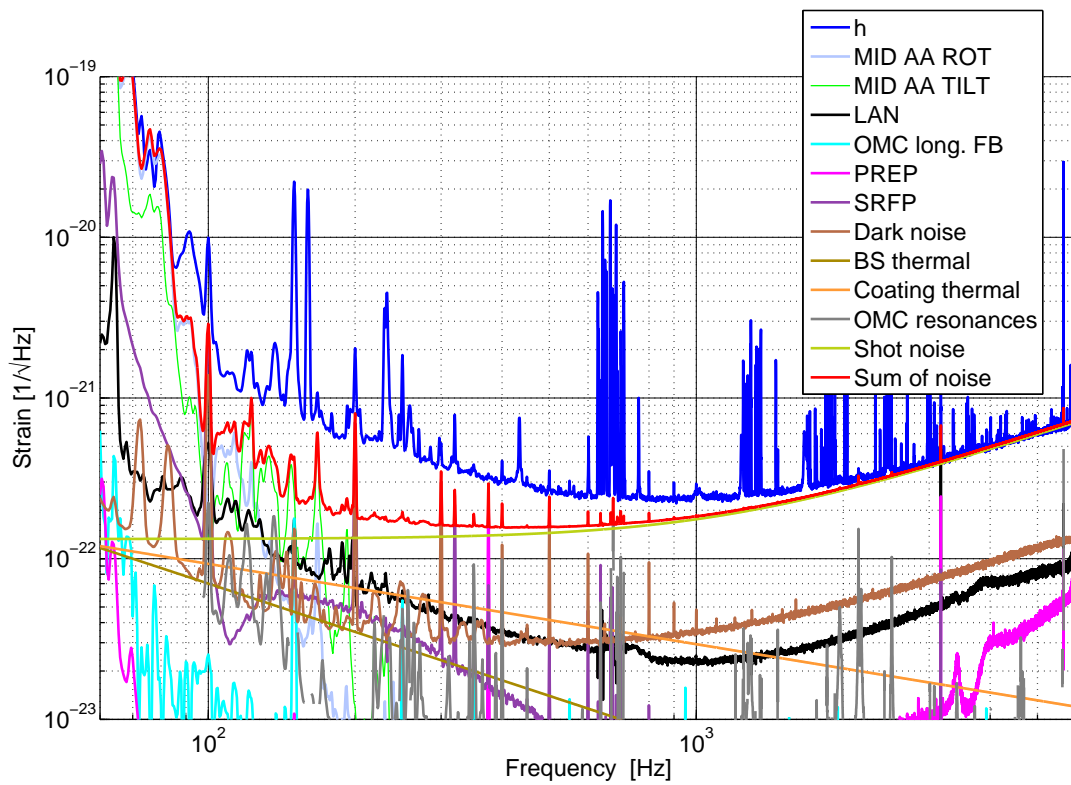


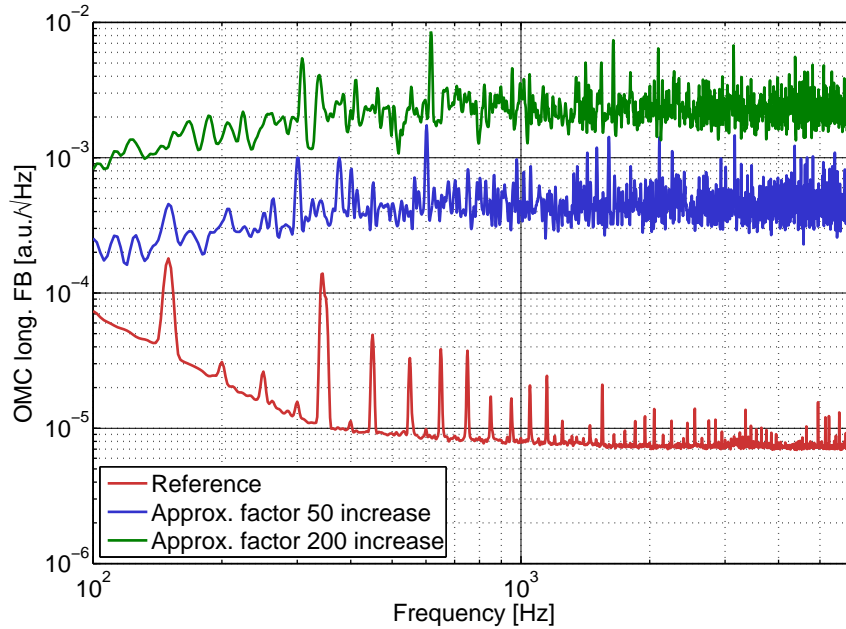
Figure 6.1: Noise projection to GEO 600's strain measurement. The noise contributions are detailed in table 6.1. The gap between the 'Sum of noise' and 'h' traces between 100 Hz and 1 kHz indicates a yet unidentified noise source.

Table 6.1: Noise contributions in fig. 6.1.

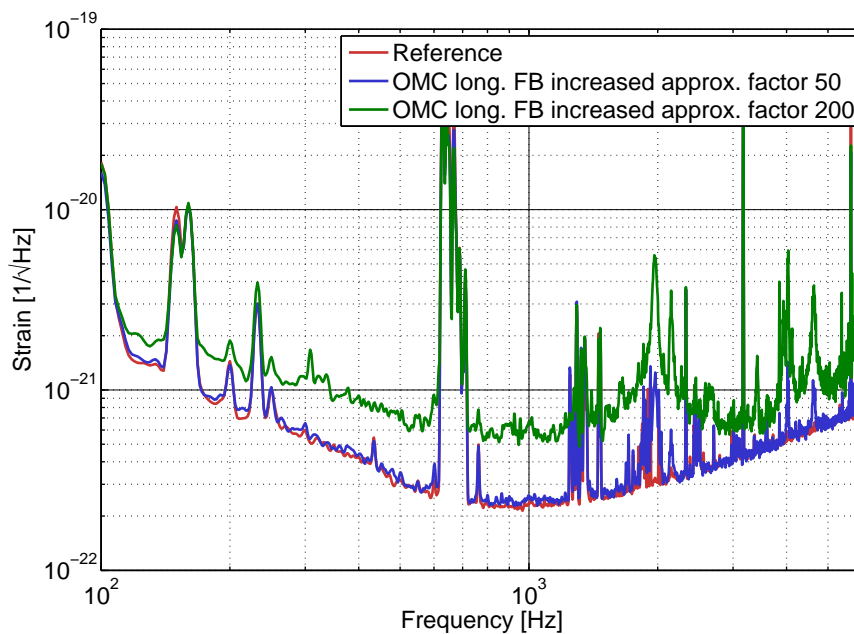
Label	Noise contribution
MID AA ROT	FB of the AA system in rotation
MID AA TILT	FB of the AA system in tilt
LAN	Laser amplitude
OMC long. FB	OMC longitudinal control FB
PREP	PRC length
SREP	SRC length
Dark noise	Electronic dark noise
BS thermal	Calculated thermal noise in the BS
Coating thermal	Calculated thermal noise in the optical coatings
OMC resonances	Resonances in the OMC
Shot noise	Shot noise, fitted to the high frequency strain sensitivity
Sum of noise	Uncorrelated sum of the noises above

Table 6.2: Simulated resonance frequencies of the first 15 mechanical modes of the OMC. For their shapes see appendix A.

Mode	Frequency [Hz]
1	1260
2	1906
3	2274
4	2327
5	2353
6	2785
7	3558
8	3767
9	4170
10	4733
11	5516
12	5832
13	6154
14	6277
15	6824



(a) Different levels of OMC longitudinal FB noise. Nominal operation state as reference.



(b) Corresponding strain sensitivity.

Figure 6.2: Effects of different levels of OMC longitudinal FB noise on GEO 600's strain sensitivity. The FB noise was artificially raised by injecting white noise at frequencies above 100 Hz. A degradation of GEO 600's strain sensitivity starts to become apparent when we increase the OMC longitudinal FB noise by a factor of 50 over the nominal operation state used as reference.

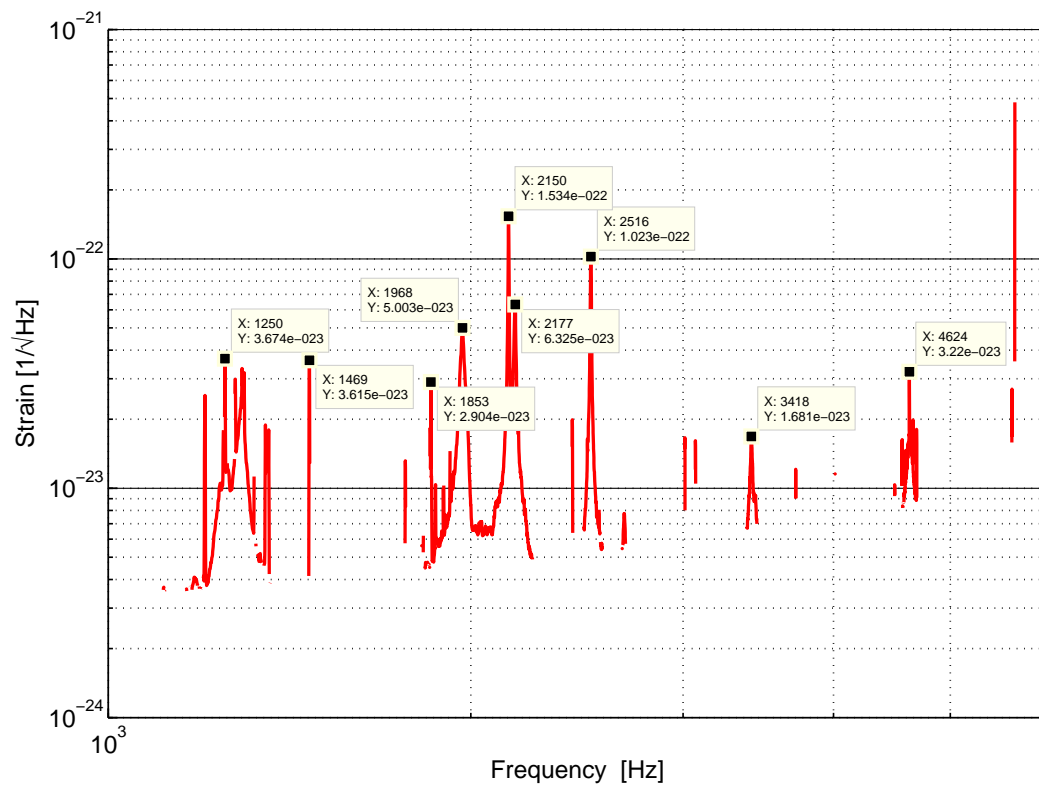


Figure 6.3: Projection of the noise due to OMC resonances to GEO 600's strain measurement. The frequencies of some prominent resonances are marked. Note that the resonance frequencies do not agree well with the simulated resonances in table 6.2.

6.2 Imperfections of the output mode cleaner optics

The OMC showed an unexpectedly high optical loss level when introduced into GEO 600. Simulations predicted a transmission of 97.6 % of the fundamental mode carrier light given optimal alignment and using spherical lenses to mode-match the interferometer's aspheric output beam onto the OMC. Measurements at GEO 600 showed a transmission of only 86 %. An investigation of spare OMC parts showed a flawed *Anti-reflective* (AR) coating of the input / output mirrors of the OMC was partially responsible for the reduced transmission. Under the nominal angle of incidence the AR coating features a reflectivity of 2 % rather than the expected 0.1 %. We attribute the remaining losses to excess intra-cavity losses of $L \approx 0.24\%$ per round-trip in eq. 6.1. This results in a calculated OMC finesse of 146.4, as presented in eq. 6.2. This result is in good agreement with the measured finesse of the OMC of 147.3 as presented in fig. 6.4. Mind that the OMC design finesse is 155 as described in section 5.1.

$$\frac{P_{\text{transmitted}}}{P_{\text{input}}} = \frac{4\delta_1\delta_2}{\delta_c^2} \stackrel{!}{=} 88\% \quad (6.1)$$

$$F = \frac{\pi\sqrt{g_{\text{rt}}}}{1 - g_{\text{rt}}} = 146.4 \quad (6.2)$$

with

P = Power

δ_i = Description of the reflectivity R_i of mirror i . $R_i = e^{-\delta_i}$

$\delta_c = \ln(|g_{\text{rt}}|^2)$ Description of the round-trip gain g_{rt}

$g_{\text{rt}} = \frac{1}{R_3 R_4 (1 - L)}$ = Round-trip gain

L = Excess loss

F = Finesse

R_1 and R_2 are defined by the reflectivities of the input and output mirrors. R_3 and R_4 are defined by the reflectivities of the two other OMC mirrors.

These losses are problematic since they, in conjunction with expected losses, limit the observable squeezing to 3.5 dB. Since we envisioned an observable squeezing of 6 dB we decided to have the spare OMC mirrors re-polished and re-coated and will implement the second iteration of the OMC within the next few months.

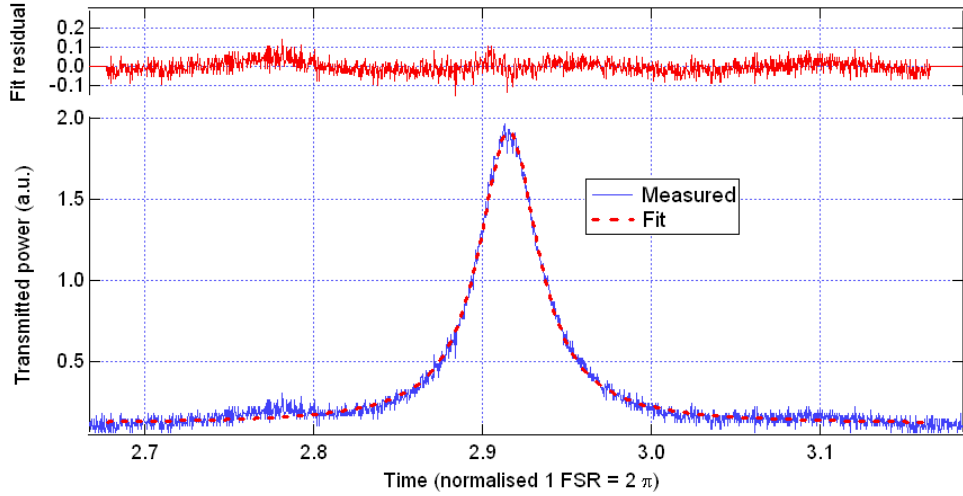


Figure 6.4: Measurement of the OMC finesse as 147.3 by fitting an airy peak to the transmitted power.

6.3 Measured upper limit for the internal noise of a piezo-electric actuator

Looking at the interferometer’s output beam as an ultra-stable light source gives us the opportunity to measure an upper limit of the internal displacement noise of the Physik Instrumente S-303 PZT OMC length actuator [PDG⁺12]. One possible noise source is the fact that the polarization of the ferroelectric PZT material responds discontinuously to changes in an external electric field. This Barkhausen effect is due to the fact that entire regions or domains of the material change their polarization in response to the external electric field [BD30].

We locked the OMC to a transmitted power of 90 % of the maximum achieved fundamental carrier light transmission. At this setting, off of peak transmission, fluctuations in OMC length couple directly to fluctuations in transmitted power. This increased the power noise in the transmitted beam (see fig. 6.5). We calculated the coupling coefficient from length fluctuations ($\text{m}/\sqrt{\text{Hz}}$) to fluctuations in light power ($\text{W}/\sqrt{\text{Hz}}$) for 6 mW transmitted power using FINESSE simulations to $1.78 \cdot 10^6 \text{ W/m}$. We arrive at an upper limit for OMC length fluctuations if we attribute all noise in the OMC transmitted power to OMC length fluctuations. As noise projections show, some of this noise can be attributed to sources other than PZT internal displacement noise. Such noise sources are OMC length fluctuations due to electric noise of the PZT HV amplifier output, fluctuations of the laser amplitude, fluctuations of the interferometer’s output frequency due to length fluctuations of the power-recycling cavity [WAA⁺02], and shot-noise. The peak at 6 kHz is due to the OMC length dither. It was beyond the scope of this thesis to investigate the origin of the other remaining noise peaks. We achieve an upper limit of approximately $2 \cdot 10^{-14} \text{ m}/\sqrt{\text{Hz}}$

(see fig. 6.6) for broadband PZT internal displacement noise after subtracting the incoherent sum of the known noise sources [PDG⁺12]. Earlier measurements either reached worse sensitivities in the 10^{-11} m/ $\sqrt{\text{Hz}}$ range [BCC⁺97, AM07], or were limited by their nature as in-loop measurements [GMB⁺99]. A similar sensitivity was reached in [Pis09].

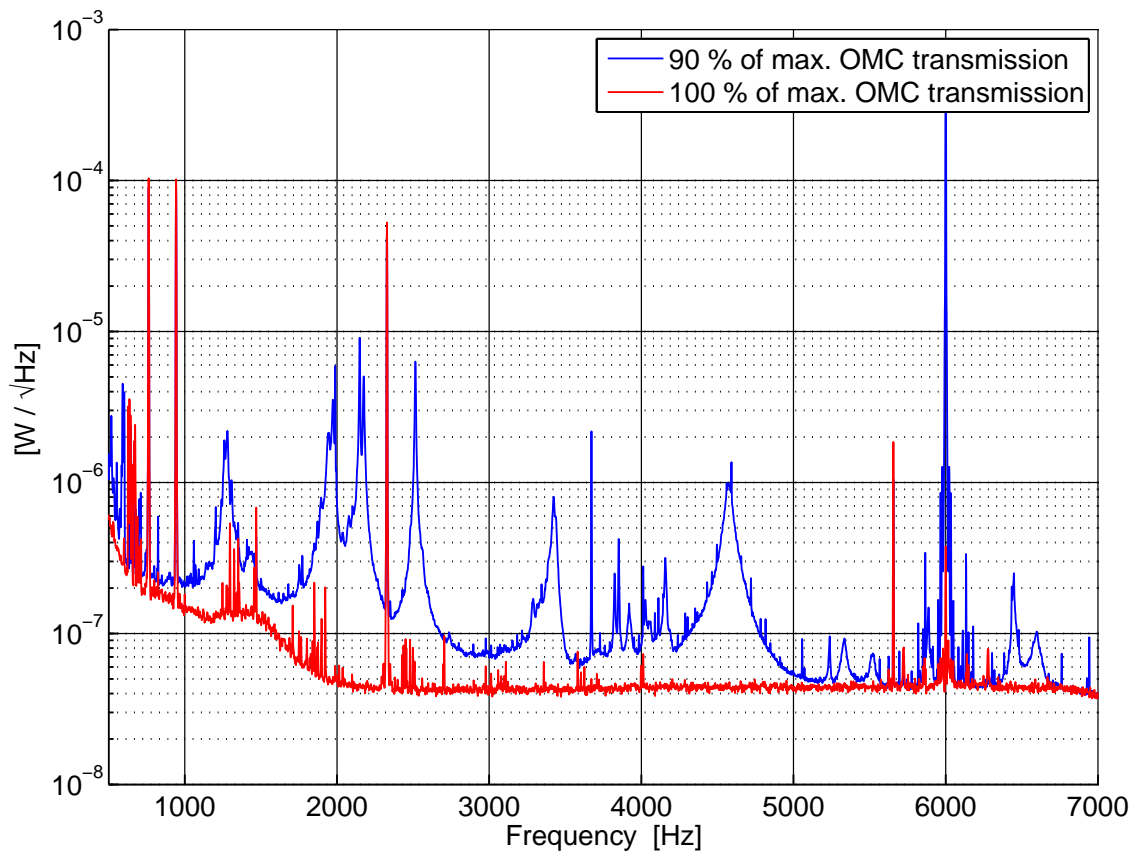


Figure 6.5: Power fluctuations in the OMC transmitted beam for different transmissions.

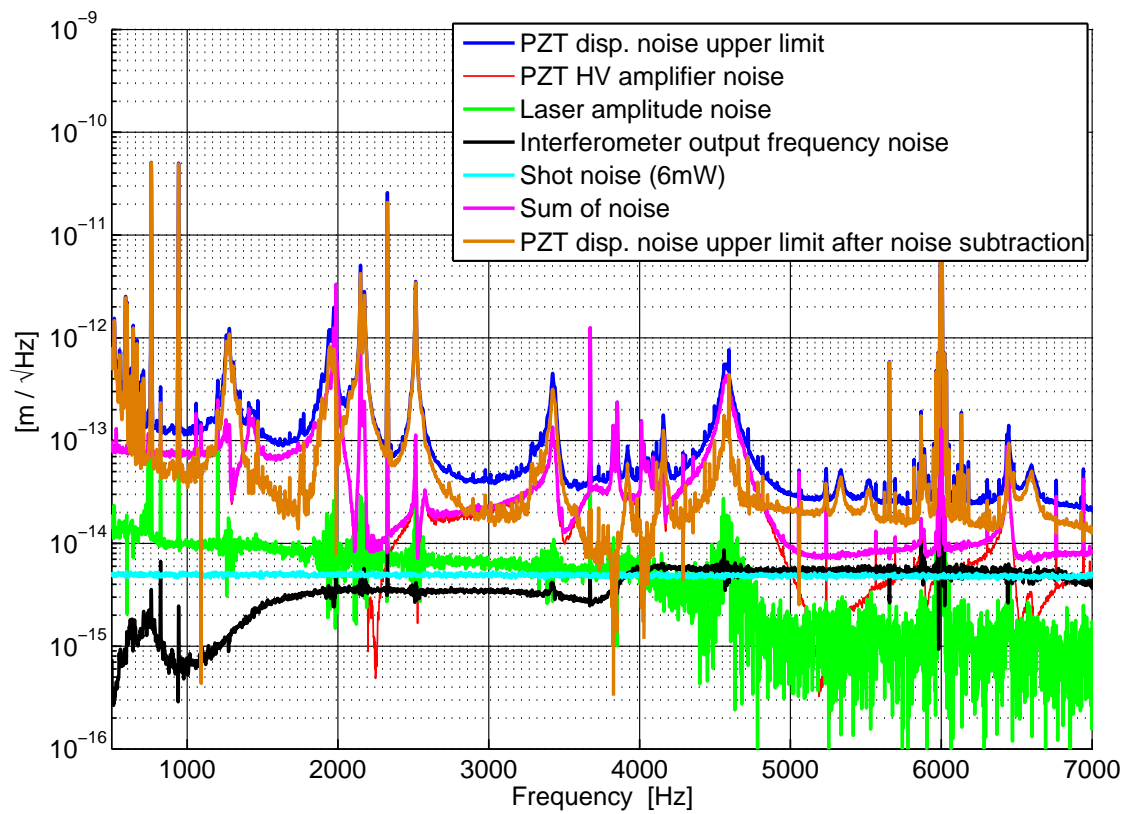


Figure 6.6: Projection of obvious sources contributing to noise in OMC transmitted power, and upper limit for PZT internal displacement noise before and after noise subtraction.

7 Summary and Outlook

The optical design of the *output mode cleaner* (OMC) proved to be effective. The OMC control systems perform their duties autonomously and reliably and keep the noise couplings due to the OMC well below GEO 600's sensitivity. We successfully evaluated different methods for alignment of beams with dominating higher order optical mode content. The vibration isolation of the OMC based mainly on commercial isolators proved to be adequate. The OMC subsystem has proven to be a stable, well performing addition to GEO 600.

A second version of the OMC is currently being assembled. Preliminary measurements indicate a much reduced optical loss in this new OMC of approximately 2%. This, with some other improvements, should allow for an observed squeezing level in GEO 600's strain measurement of approximately the originally envisioned 6 dB. The new OMC will have a round-trip length increased by 18 mm to resolve the degeneracy between 6th order HOMs and 14.9 MHz sidebands.

The GEO-HF upgrade program of GEO 600 has made great progress. The improvement in sensitivity of GEO 600 over the course of the upgrade is displayed in fig. 7.1. The upgrade program was successful in keeping GEO 600's sensitivity comparable to the sensitivities of the interim detector stages Enhanced LIGO and VIRGO+ as presented in fig. 1.5.

Improvements of GEO 600 are ongoing. An increase in utilized laser power to 35 W and the implementation of a TCS are planned for 2012-2013 as remaining parts of the GEO-HF upgrade program. We are currently investigating the possibility to improve the sensitivity at frequencies below 100 Hz by reducing the *feedback* (FB) of the interferometer's automatic alignment system (see fig. 6.1 and table 6.1). In this, a feed-forward system would use the data from multiple seismometers to reduce the motion of the interferometer's mirrors, allowing for a more lenient FB system. Identification of the limiting factor of GEO 600's sensitivity at frequencies between 100 Hz and 1 kHz remains a high priority. Glitches¹ are especially detrimental to the detection of burst-like gravitational waves, for which GEO 600 is especially suited. The work to reduce the number of glitches in GEO 600 has intensified over the past year and is ongoing.

While gravitational-wave detectors function best in a network, GEO 600 might even be able to provide some astrophysically relevant data during the downtime of the other gravitational-wave detectors. This is made possible by the combination of GEO 600's data with that collected using other observation methods, such as optical observations, neutrino

¹ Glitches are non-stationary noise contributions to the strain signal that are typically short-lived.

detection or X-ray detection. Possible GW sources to be detected by this approach might be burst events at magnetars, which would be coincident with short X-ray bursts [PBG⁺05] or certain types of supernovae [YMM⁺10].

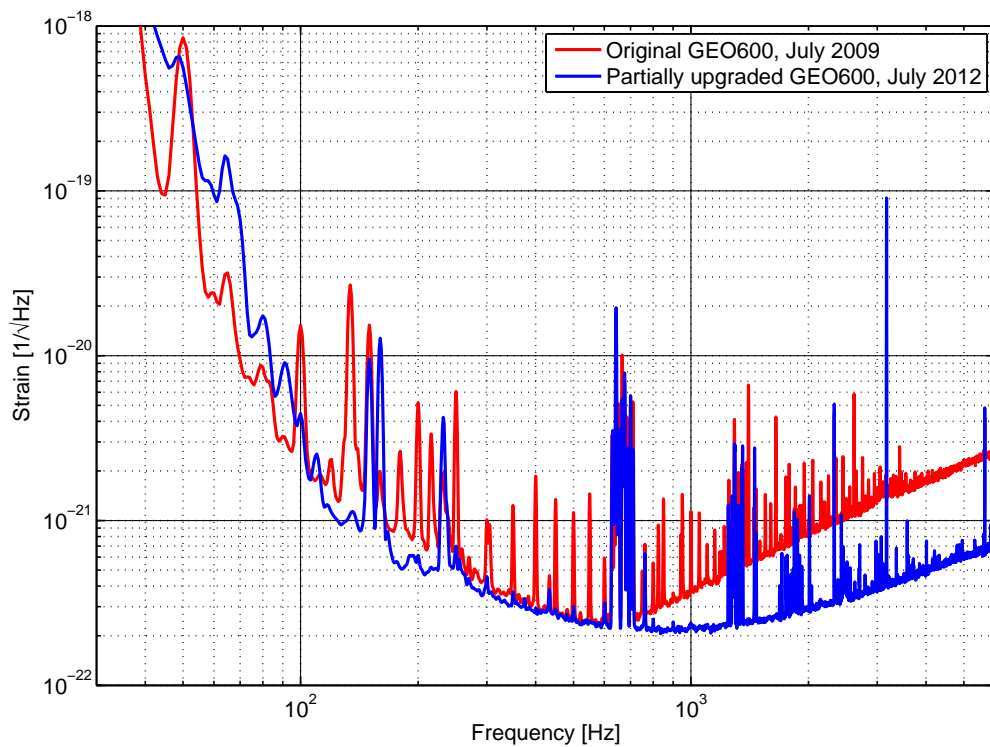
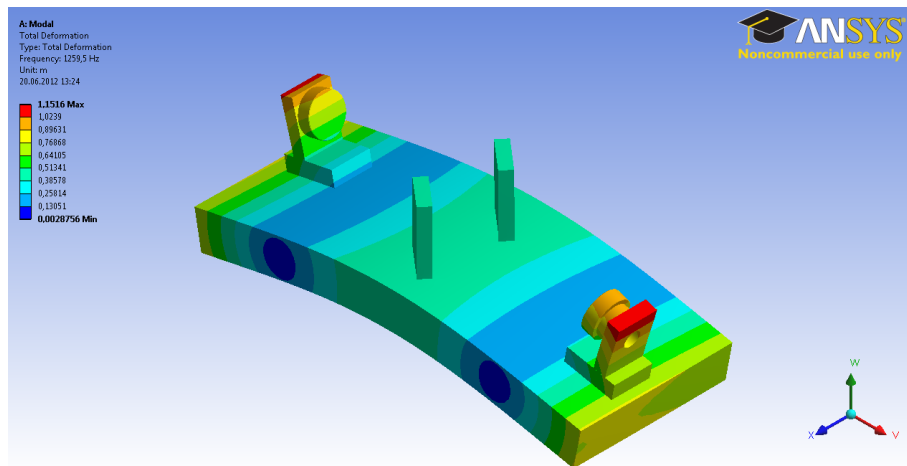


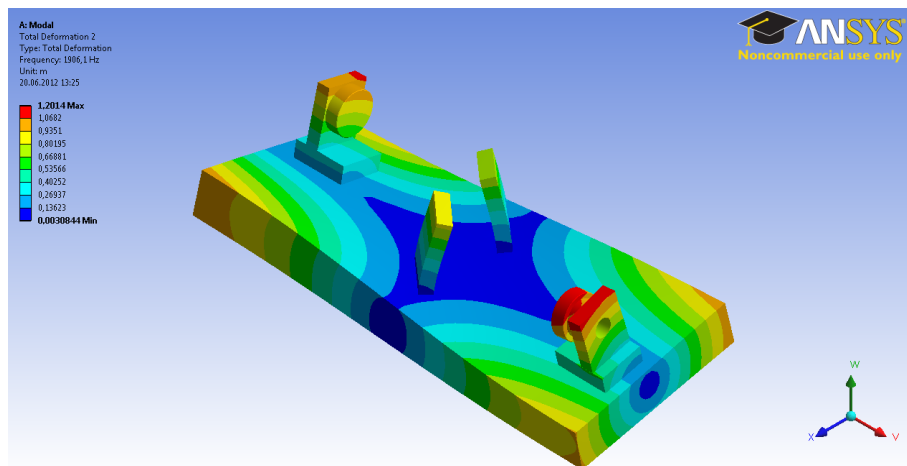
Figure 7.1: Improvement of the sensitivity of GEO 600 during the GEO-HF upgrade program so far. The improvement is in part due to the implementation of an OMC described in this thesis.

A Shapes of the mechanical modes of the output mode cleaner

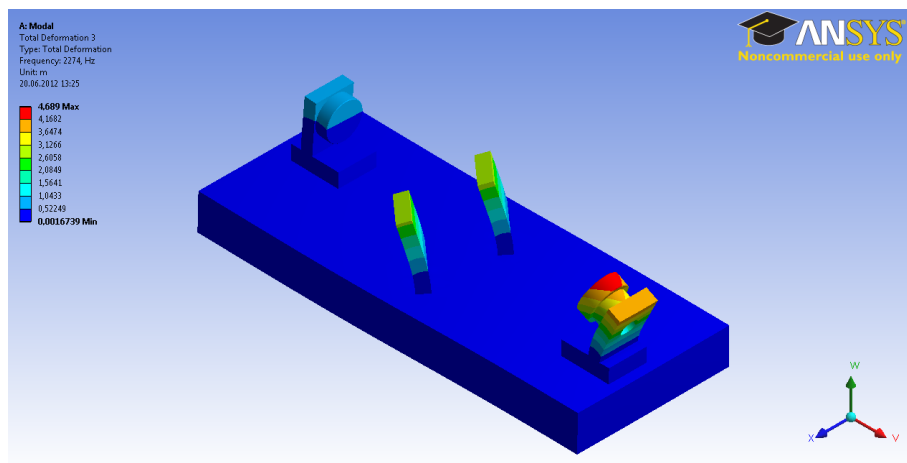
We simulated the mechanical modes of the OMC using the ANSYS FEM simulation package as described in section 6.1. Here we present the shapes of the first 15 modes. The resonance frequency of the lowest mode is at 1260 Hz and that of the highest simulated mode is at 6824 Hz.



(a) 1. mechanical mode at 1260 Hz.

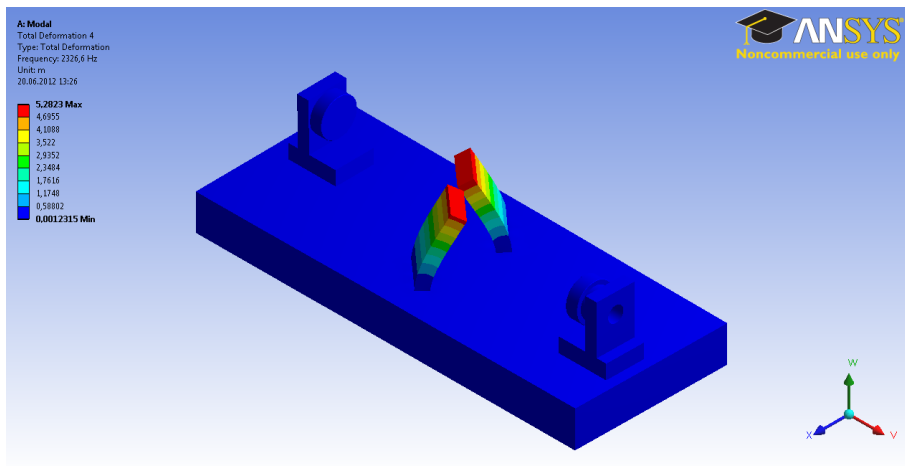


(b) 2. mechanical mode at 1906 Hz.

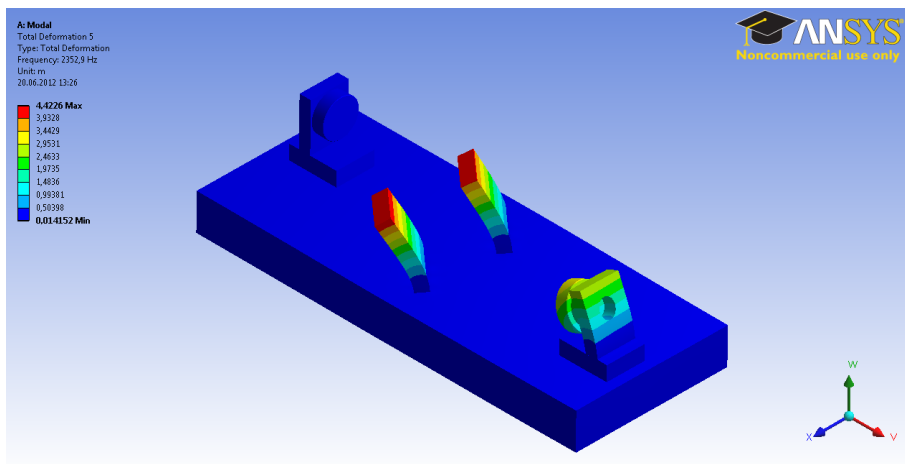


(c) 3. mechanical mode at 2274 Hz.

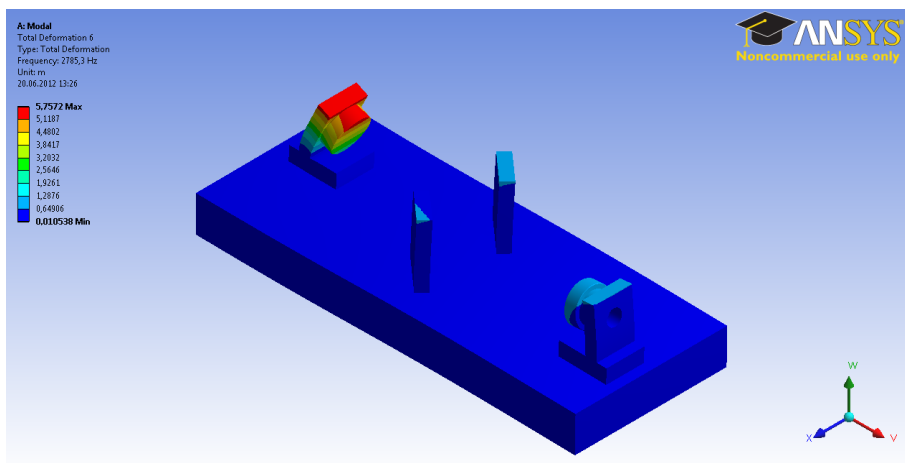
Figure A.1: OMC mechanical modes as simulated with the ANSYS software package. Not to scale. Disregard the relative and absolute amplitudes.



(d) 4. mechanical mode at 2327 Hz.

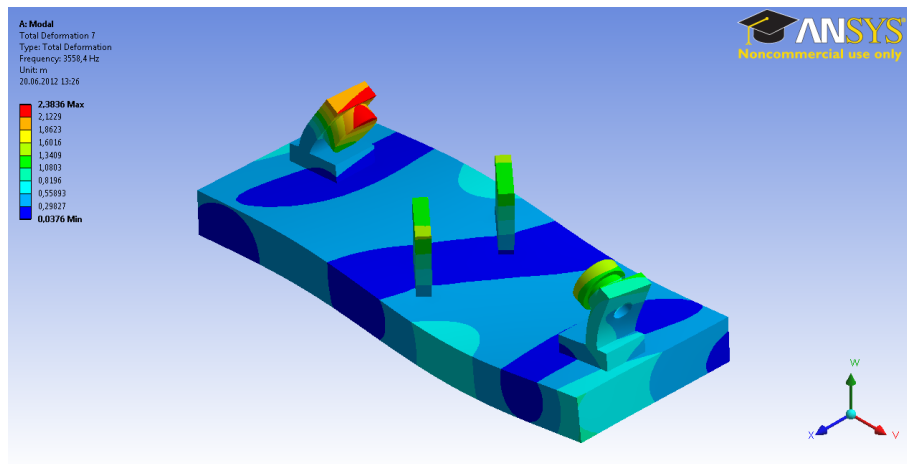


(e) 5. mechanical mode at 2353 Hz.

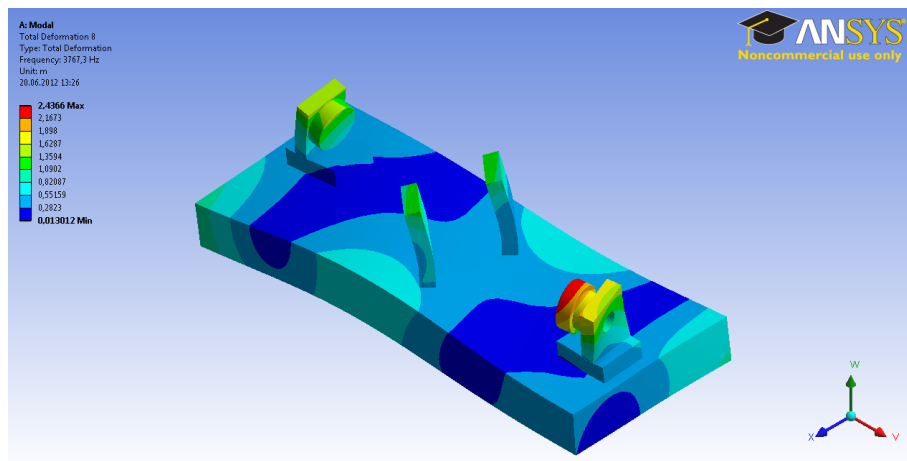


(f) 6. mechanical mode at 2785 Hz.

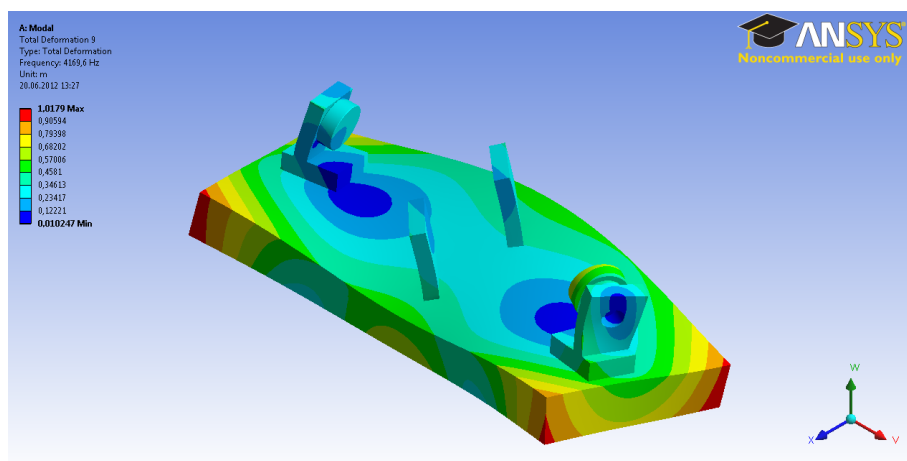
Figure A.1



(g) 7. mechanical mode at 3558 Hz.



(h) 8. mechanical mode at 3767 Hz.



(i) 9. mechanical mode at 4170 Hz.

Figure A.1

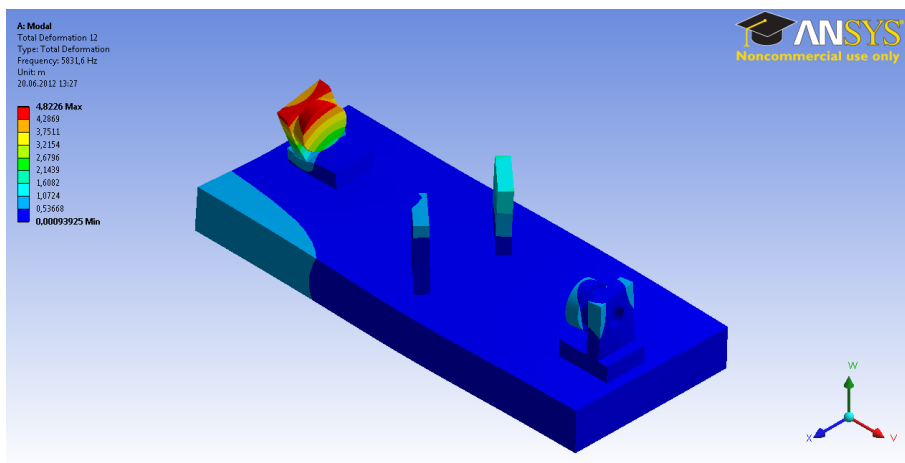
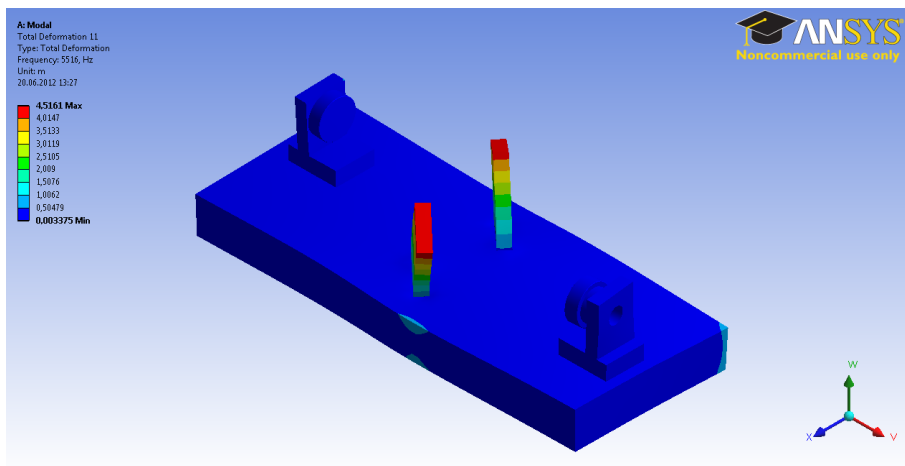
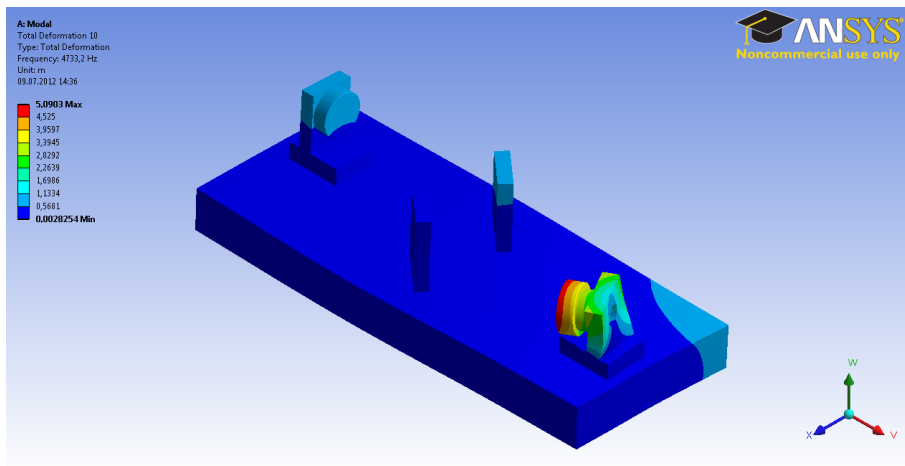
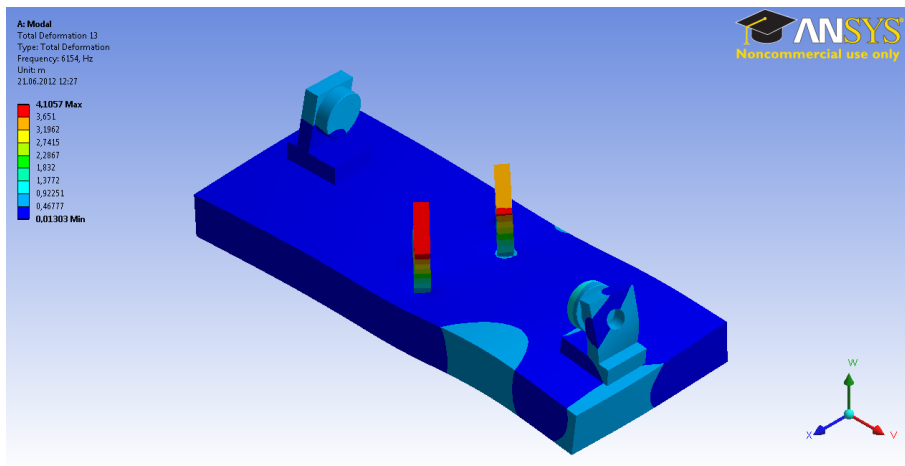
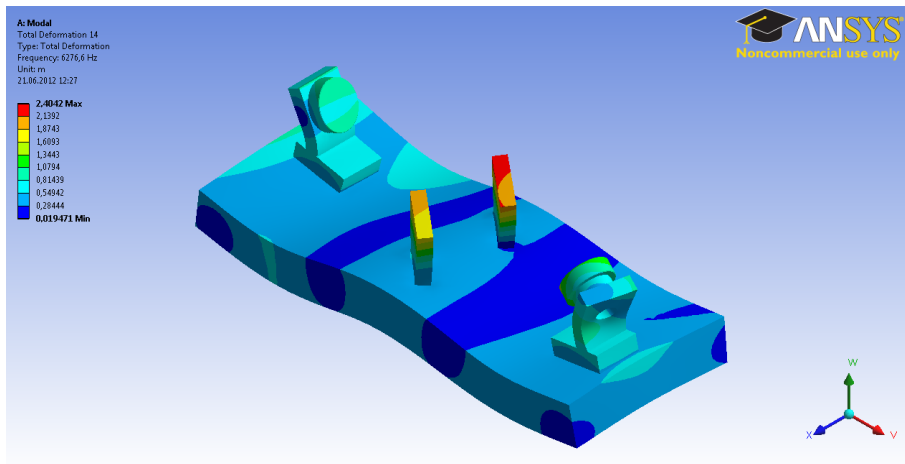


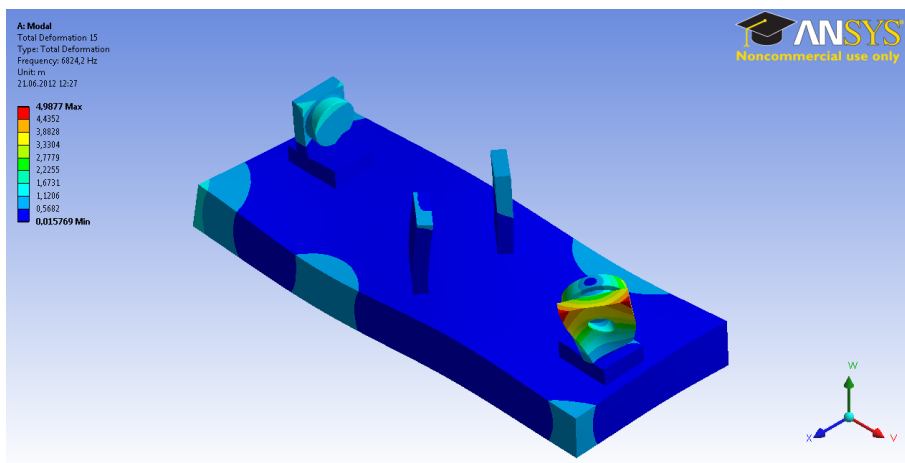
Figure A.1



(m) 13. mechanical mode at 6154 Hz.



(n) 14. mechanical mode at 6277 Hz.



(o) 15. mechanical mode at 6824 Hz.

Figure A.1

B Performance evaluation of the Control and Data System

The OMC was the first subsystem in GEO 600 to employ the CDS system. This required us to examine the CDS's performance.

Data acquisition noise performance

One of the most fundamental duties of a control system is to acquire data. The data acquisition performance of a digital system is determined by its *analog to digital converters* (ADCs) and its *anti-aliasing* (AA) filters.

A digital system like the CDS uses ADCs to convert analog values (typically voltages) to digital values. Due to possible aliasing problems, signals should not be connected to ADCs directly. The Nyquist theorem [Nyg28] states that to accurately measure a signal at a frequency f_{signal} there need to be at least two measurement points per period, i.e.

$$f_{\text{measurement}} \stackrel{!}{\geq} 2f_{\text{signal}} \quad (\text{B.1})$$

Since the CDS system is able to run at a maximum rate of 65536 Hz, the maximum frequency it can accurately measure is

$$f_{\text{Nyquist}} = 32768 \text{ Hz} \quad (\text{B.2})$$

Without AA filters signals at frequencies $f_{\text{signal}} > f_{\text{Nyquist}}$ will be acquired at the incorrect frequencies f'_{signal}

$$f'_{\text{signal}} = f_{\text{Nyquist}} - (f_{\text{signal}} \bmod f_{\text{Nyquist}}) \quad (\text{B.3})$$

While this effect can be used to measure signals that would ordinarily be out of reach of the ADCs, generally this effect is undesirable. To avoid it, appropriate (low-pass) AA filters need to be placed in front of the ADCs. The CDS uses custom-made high order low-pass AA filters with a cut-off frequency of approximately 10 kHz (see fig. B.1).

Intrinsic Noise

We evaluated the data acquisition performance of the CDS by evaluating its intrinsic noise, or dark noise, to $3.5 \cdot 10^{-6} \text{ V}/\sqrt{\text{Hz}}$ at an acquisition rate of 65536 Hz, as depicted

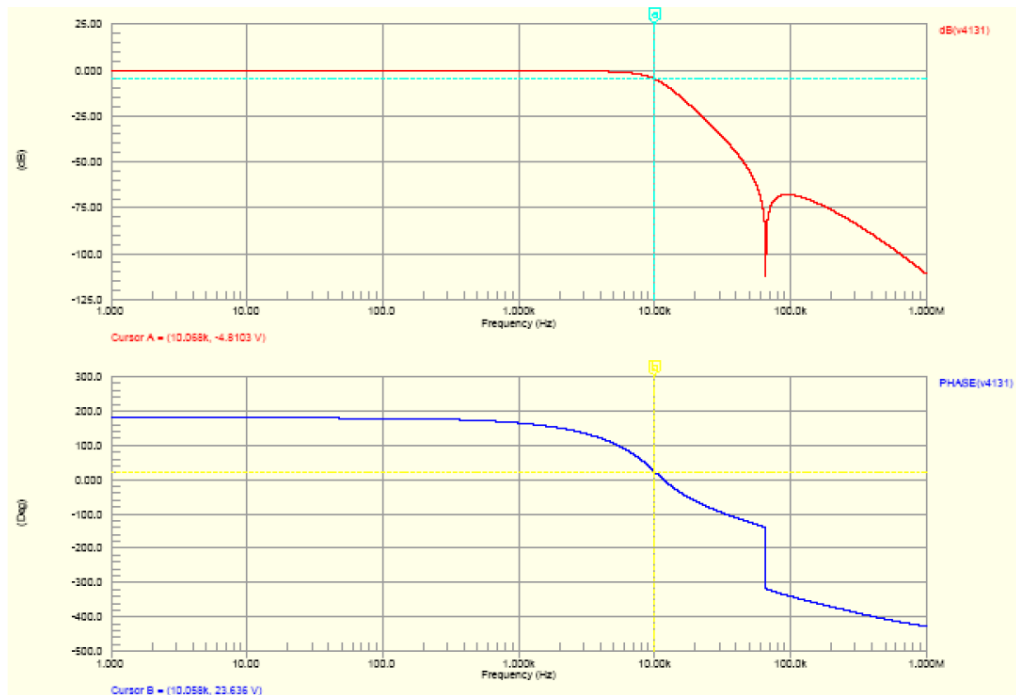


Figure B.1: Measured transfer function of the AA / AI filters of the CDS [Hee07].

in fig. B.2. This value agrees well with manufacturer claims for the performance of the ADCs of $3.9 \cdot 10^{-6} \text{ V}/\sqrt{\text{Hz}}$ [Cor b] and is reasonably close to the value measured at LIGO of $5 \cdot 10^{-6} \text{ V}/\sqrt{\text{Hz}}$ [Hee06].

The theoretical quantization noise limit for a 16 bit ADC with a 65536 Hz acquisition rate is $6.8 \cdot 10^{-7} \text{ V}/\sqrt{\text{Hz}}$.

Channel Cross-talk

We evaluated the cross-talk between neighboring channels in the CDS by injecting a swept-sine signal to one CDS channel and then measuring the cross-talk to a neighboring channel. The resulting cross talk of approximately -90 dB is negligible for almost all applications of the CDS system.

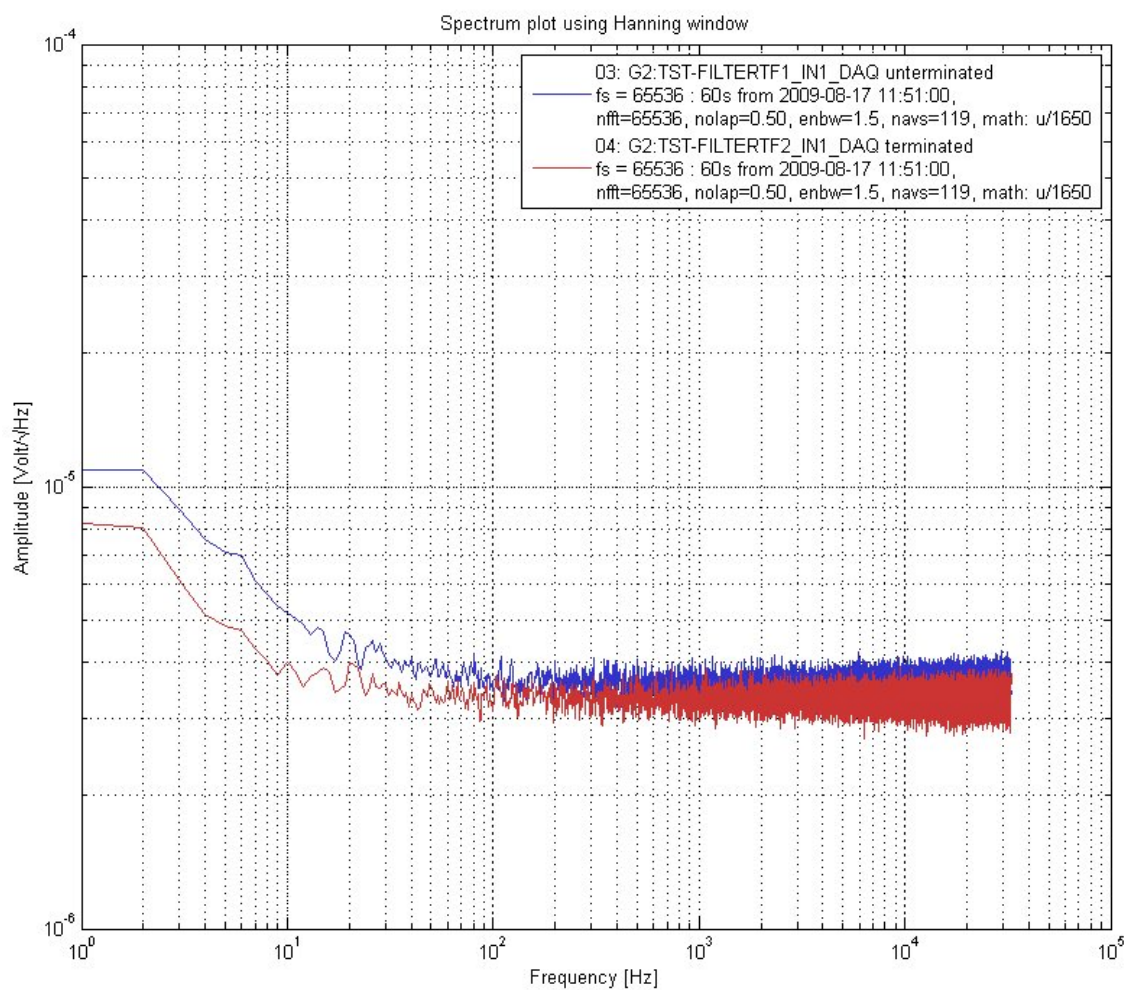
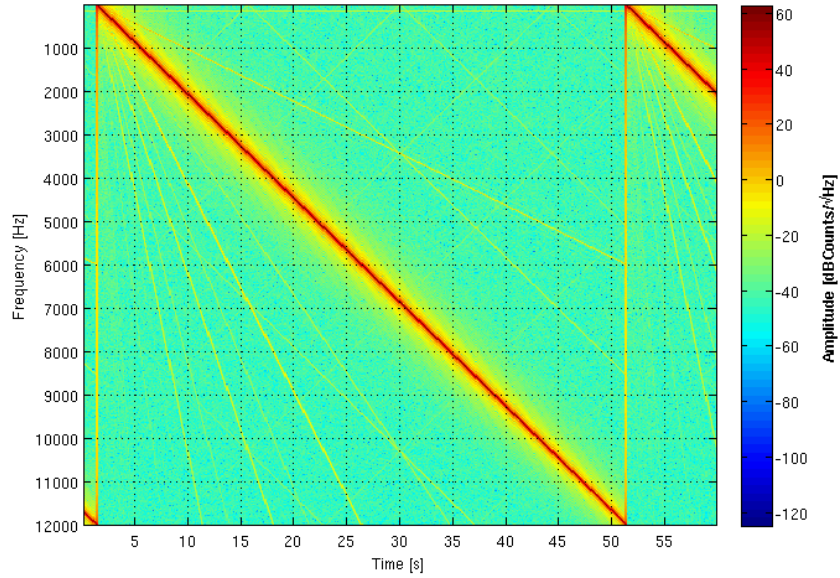
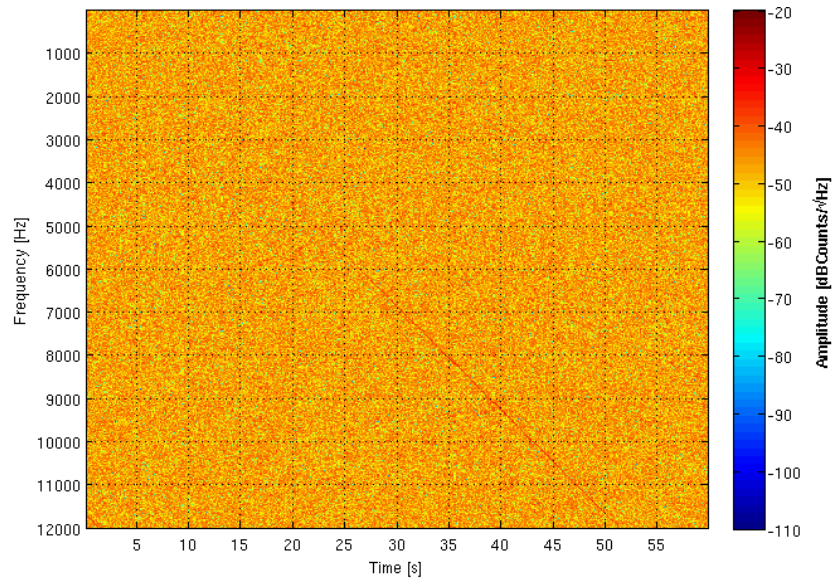


Figure B.2: Intrinsic noise, or dark noise, of the CDS at an acquisition rate of 65536 Hz.



(a) Injected signal.



(b) Cross-talk in neighboring channel.

Figure B.3: Spectrograms depicting the cross-talk between physically neighboring channels for an injected signal of 2.5 V amplitude.

Data generation performance

A control system does not only need to acquire data, of course also needs to be a source of data. We therefore also checked the performance of the *digital to analog converters* (DACs). The noise floor of the DACs was measured to be below $1 \cdot 10^{-6} \text{ V}/\sqrt{\text{Hz}}$ as depicted in fig. B.4.

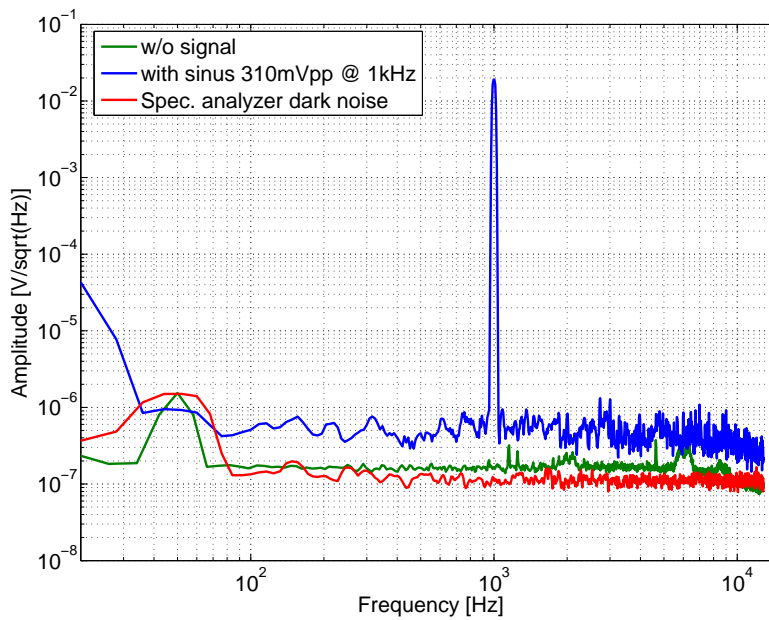


Figure B.4: Performance of the CDS's DACs, as measured by a spectrum analyzer.

CDS's performance as a lock-in

A great number of measurements at GEO 600 require demodulations of input signals. We therefore created a software lock-in in CDS and compared its performance to a EG&G Princeton Applied Research model 5302 hardware lock-in. The logic of the software lock-in, in its Simulink form, is depicted in fig. B.5. This Simulink model is then parsed by the *real-time code generator* (RCG) that generates C-code that is actually executed by the CDS. The 'FreqGen' block generates the sinusoidal signal used to modulate the measurement and also generates the signal to demodulate the measurement. The 'Filterdelay' block provides adjustment of the demodulation phase. The actual demodulation happens at the product block, that multiplies the frequency generator's signal with the measured value. The 'Filterinput' and 'Filteroutput' blocks provide filtering before and after the demodulation. The subsystem block is a technical necessity that does not apply any changes to the signals. The 'ADC' blocks correspond to ADC, or input, channels and provide signal sources in the model. The 'DAC' block corresponds to DAC, or output, channels.

The measurement setup is depicted in fig. B.6. The correct signal is, after demodulation, at DC. Signals at frequencies above DC are noise. A lower spectral density therefore corresponds to a better performance of the respective lock-in. We used the CDS frequency generator to generate a sinusoidal signal with an amplitude of 78 mV at 3 kHz for the

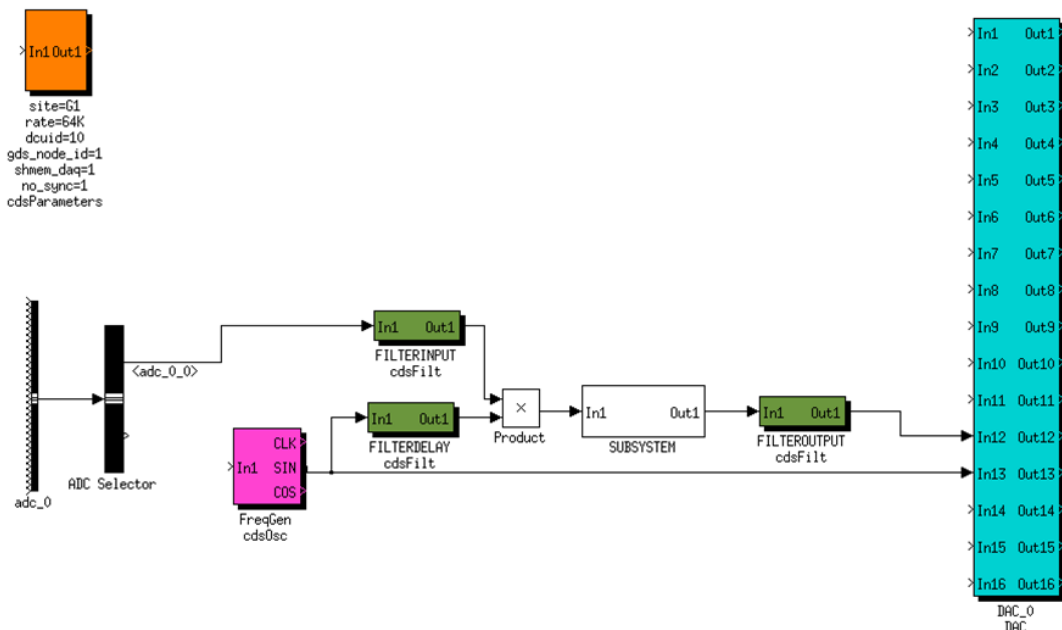


Figure B.5: Software lock-in realized in CDS, described in a Simulink model that can be parsed by the code generator to generate real-time code.

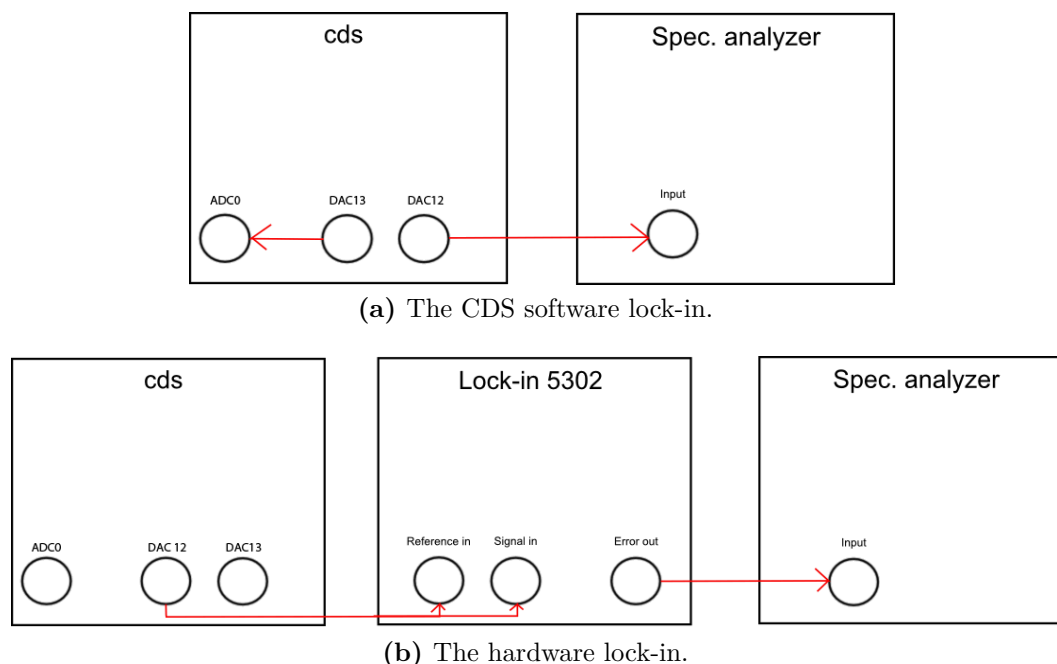


Figure B.6: Setup for the performance evaluations of different lock-ins. The red arrows show the signal pathways.

lock-ins to demodulate. It is important to have similar DC values and similar filtering in both lock-ins to allow for a fair comparison. The filtering in the hardware lock-in is restricted by the technical limitations of analog circuitry. In fig. B.7 we depict the magnitude of the transfer function of the band-pass in the hardware lock-in before the demodulation point. There is an additional filter behind the demodulation point which is user-adjustable to either a first or second order low-pass with user-adjustable frequency. The corresponding filters in CDS are:

- **Band-pass filter before demodulation point:** Resonant gain, $Q=2$, gain=50 dB
- **Low-pass filter after demodulation point:** First order low-pass with corner frequency of 160 Hz

The bandwidths were compared by switching the signal generation inside CDS on and measuring the step response.

As presented in fig. B.8 the performance of CDS for this filter configuration was better than that of the hardware lock-in.

Sinusoidal vs. square-wave demodulation

Hardware lock-ins usually do not use sinusoidal voltage wave-forms to demodulate the incoming signals they are locking on. Due to the difficulty of generating a high-precision

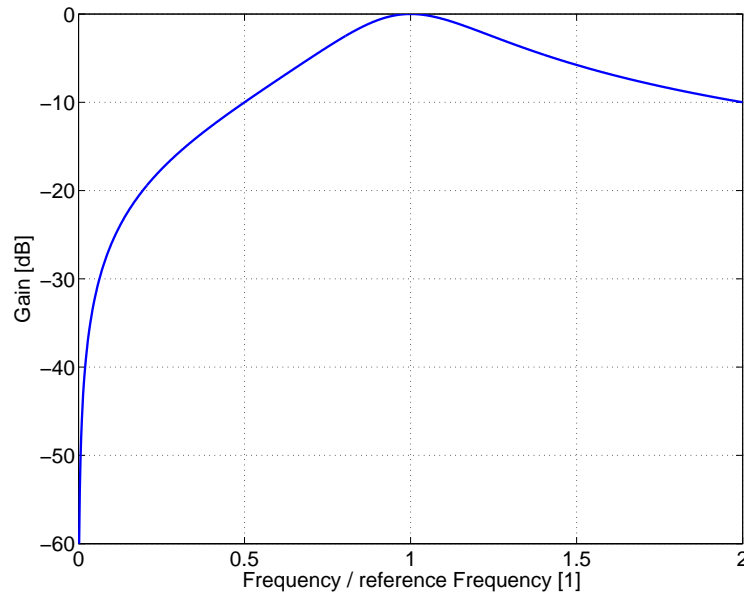


Figure B.7: Input filter of the EG&G Princeton Applied Research model 5302 hardware lock-in, as described in [Cor a].

sinusoidal voltage reference wave-form, lock-ins usually utilize square-waves of the appropriate frequency to demodulate the incoming signals. There are two criteria to judge which technique works better.

1. **How clean is the DC value of the lock-in's output:** In fig. B.9 we simulated the contributions from different frequency components in the lock-in's input signal to its output signal. Ideally the values should be zero for all frequencies except the reference frequency. It is clearly evident in fig. B.9 that the sinusoidal demodulation has fewer contributions from higher harmonics than the square-wave demodulation. Sinusoidal demodulation is more susceptible to imperfections in the sinusoidal reference frequency than square-wave demodulation. The imperfections have to be on the order of several tens of percent to make sinusoidal demodulation less accurate than square-wave demodulation. The quality of the CDS's sinusoidal wave generator is much better than that.
2. **How low is the noise in the lock-in's output at frequencies above DC:** We implemented a square-wave demodulation in CDS and checked the output of this demodulation. As presented in fig. B.10 the sinusoidal demodulation is clearly superior.

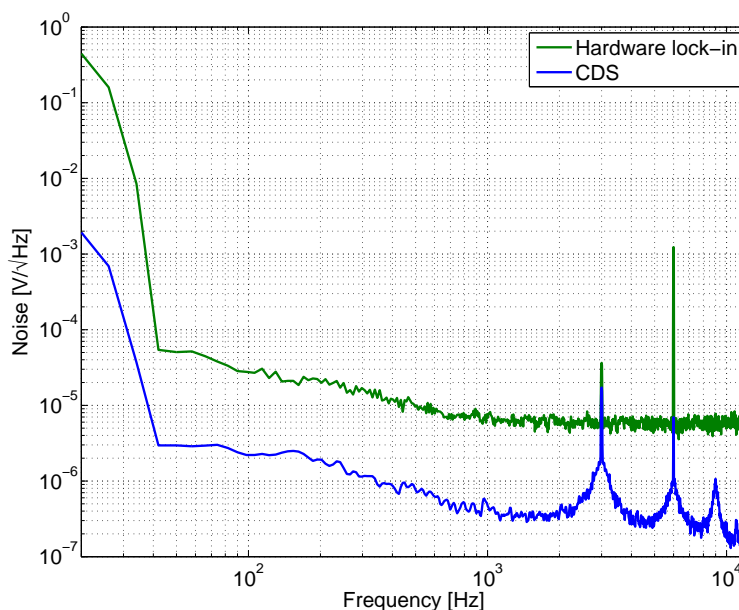
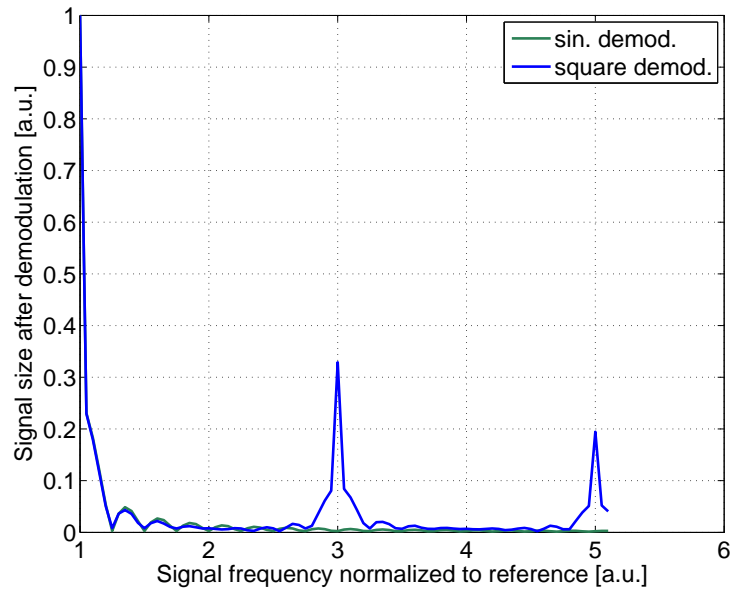


Figure B.8: Comparison of the noise performance of CDS and a hardware lock-in.
DC values: CDS: 4.70 V hardware lock-in: 4.78 V **Bandwidths:** CDS: 151 Hz, HW-LI: 149 Hz.

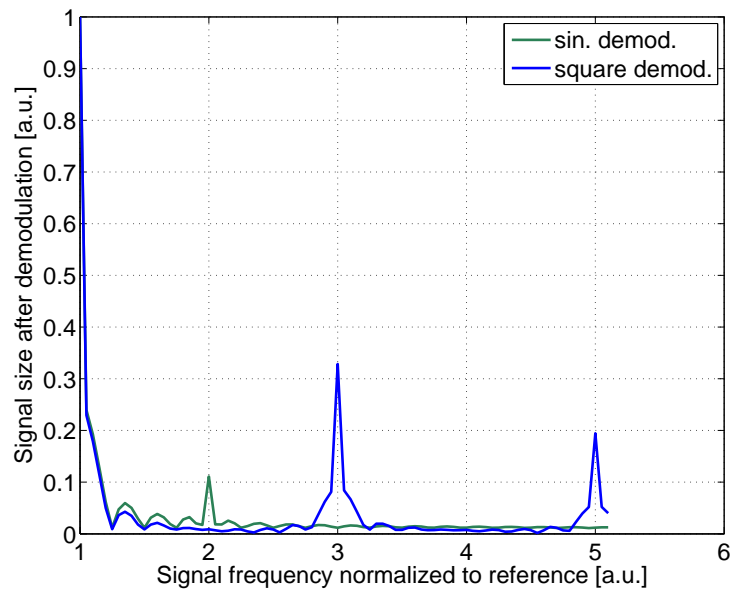
We established that the sinusoidal demodulation is the clearly superior demodulation technique to use in a CDS software lock-in.

Round-trip delay

The amount of delay that signals acquire during one round-trip (being generated by CDS and being read back into CDS) defines CDS's usable frequency range. We measured this round-trip delay by measuring the transfer function in CDS between a signal generated in CDS staying purely in the software domain, and another signal that was converted to a voltage by a DAC and then read back by an ADC. Converting the frequency dependent phase delay to a time delay, we measured a frequency independent time delay of approximately 115 μ s (see fig. B.11).



(a) Perfect sinusoidal reference signal.



(b) Imperfect sinusoidal reference signal. Contributions of 0.1·reference at twice the reference frequency.

Figure B.9: Simulated contributions to the demodulated signal at DC for different demodulation techniques and different purities of the reference signal used for demodulation.

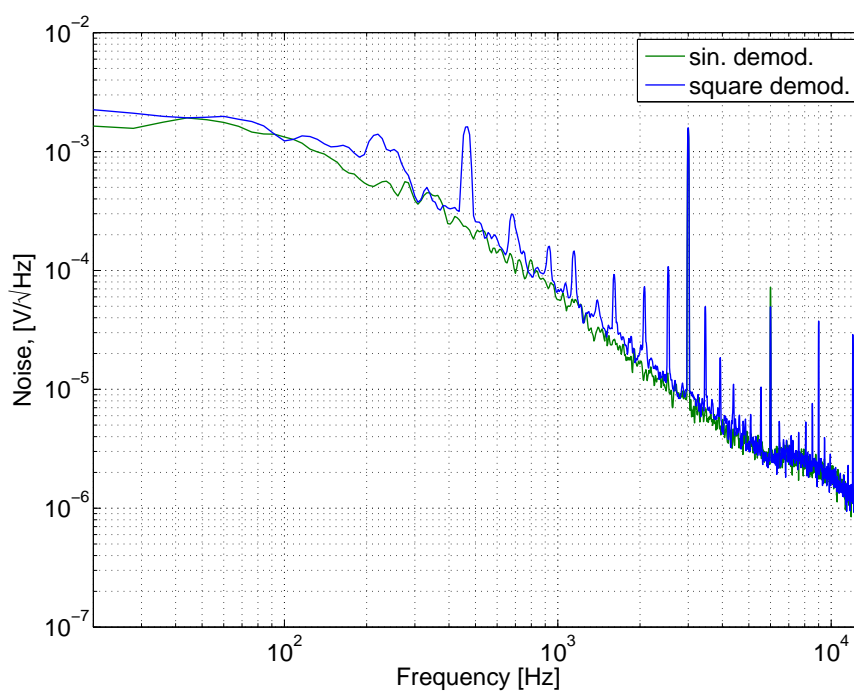


Figure B.10: Comparison of demodulation with square and sinusoidal reference signals. DC signals after demodulation were identical. The signals were filtered with two low-pass filters after the demodulation point with corner frequencies of 80 Hz and 400 Hz respectively.

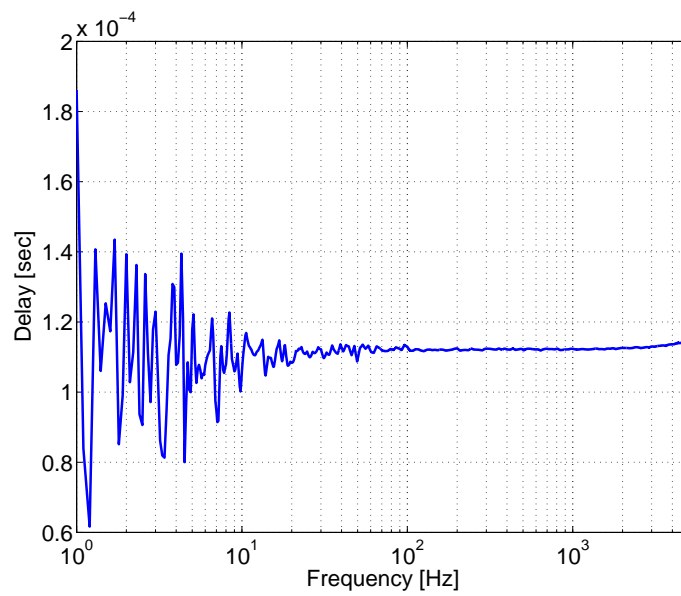


Figure B.11: Round-trip delay of the CDS.

C The control model of the output mode cleaner in the Control and Data System

In this chapter we present the logic in the CDS system that controls the OMC. The logic is presented in Simulink form that is parsed by the RCG to generate C-code that the CDS then executes. The lock acquisition logic for the OMC is a block of C-code visible as the ‘LockAcqGEO’ cdsFunctionCall block in fig. C.1. Details on the OMC lock acquisition can be found in appendix D.

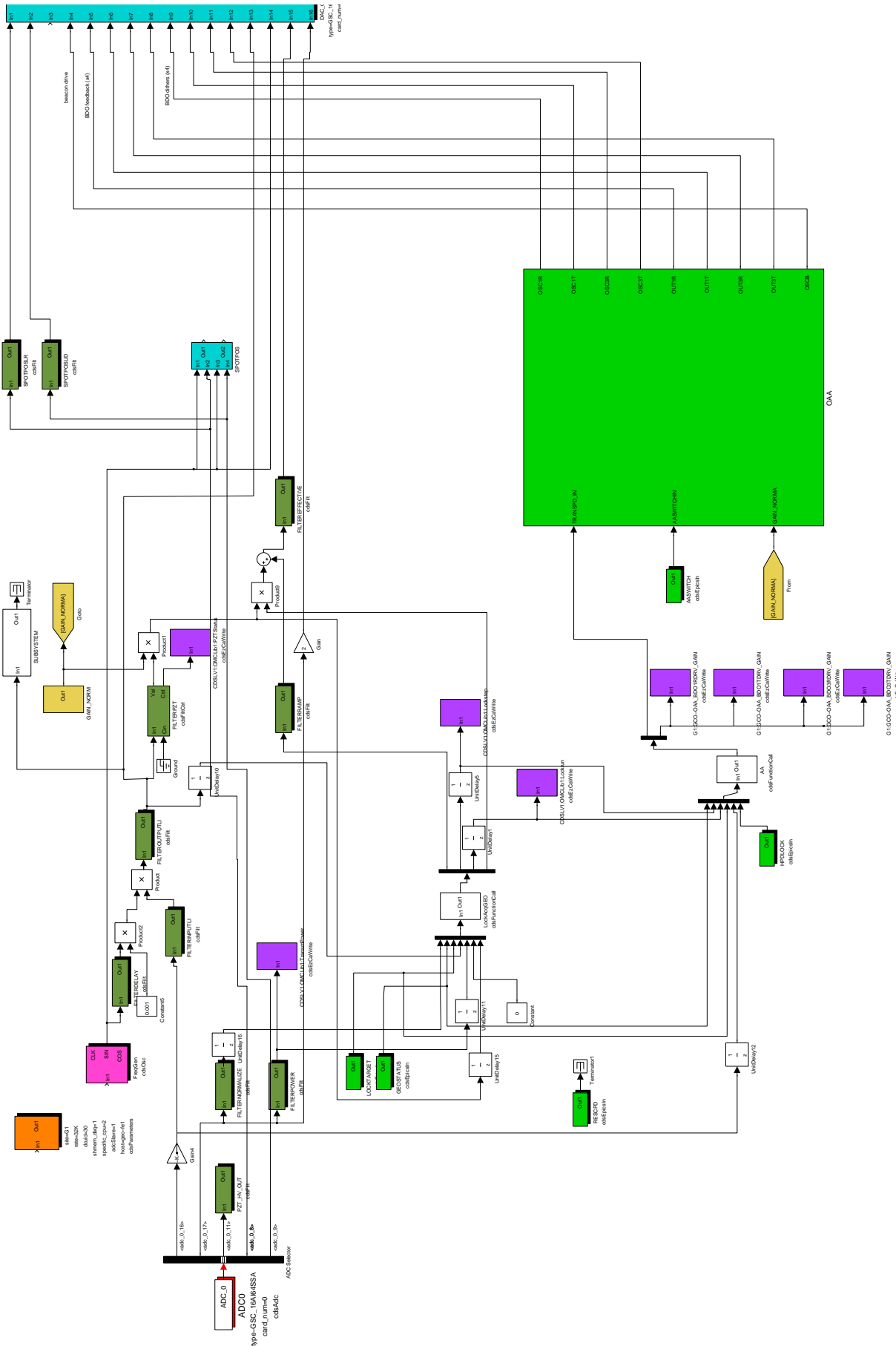


Figure C.1: The OMC control logic represented in Simulink.

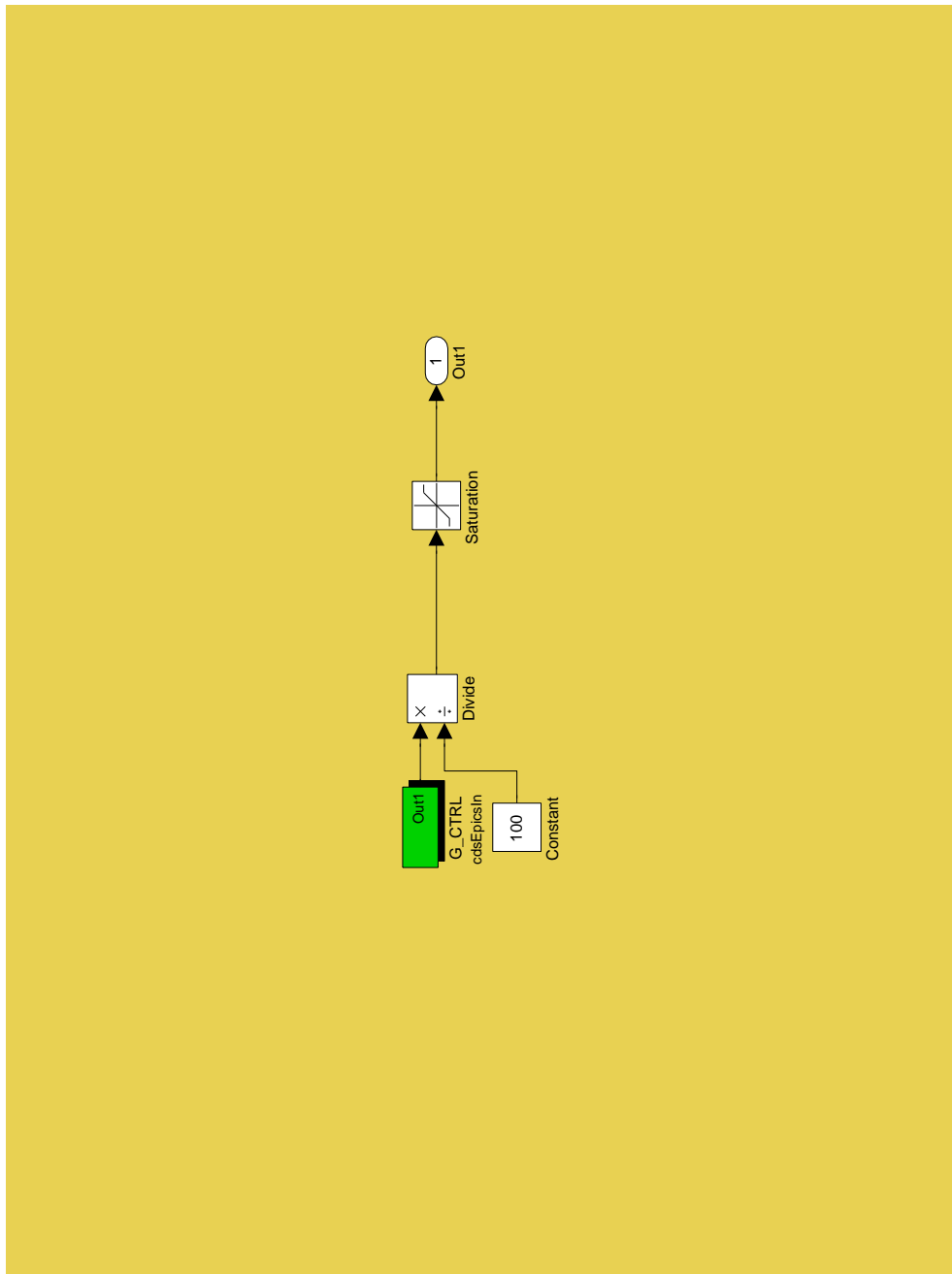


Figure C.2: The GAIN_Norm subsystem. This subsystem receives information about the laser system's power output and normalizes the OMC control loops with regard to that laser power.

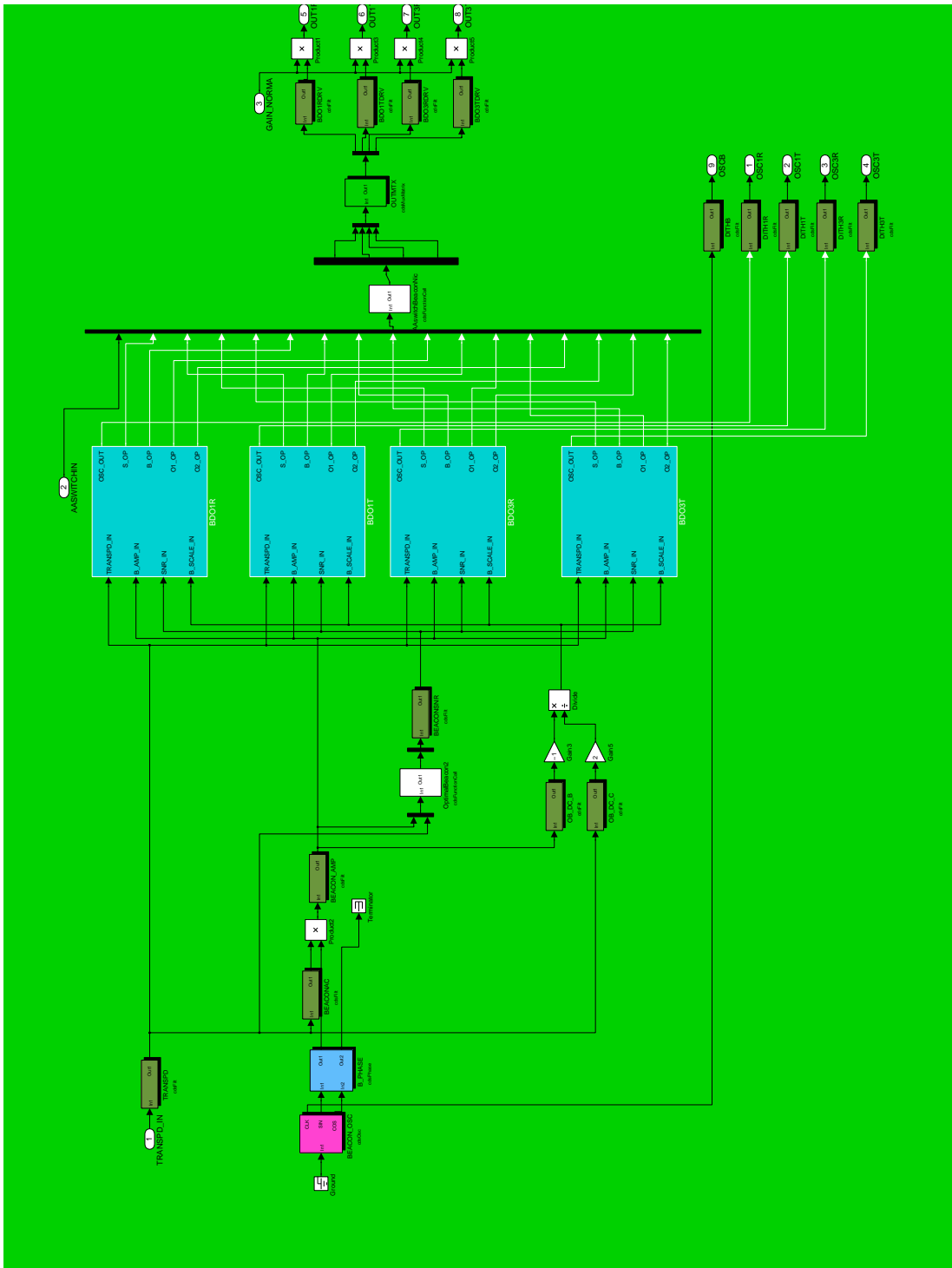


Figure C.3: The OAA subsystem, containing the alignment control elements.

D Output mode cleaner lock acquisition logic

The lock acquisition algorithm of the OMC needed to be able to lock onto different user-selectable components of the output beam. In its current iteration it can lock onto the fundamental mode carrier light, as is needed for GW measurements, or the either of the SBs at 14.9 MHz. A special challenge for the lock acquisition algorithm was that after the exchange of MSR, as described in chapter 4, the fundamental mode carrier light was no longer the strongest component of the beam. The OMC lock acquisition algorithm exploits the fact that the fundamental mode carrier light and the SBs at 14.9 MHz form a characteristic triplet structure. On the following pages we present a simplified flow chart of the lock acquisition logic and its implementation in C-code. Further details on the lock acquisition process are presented in subsection 5.4.4

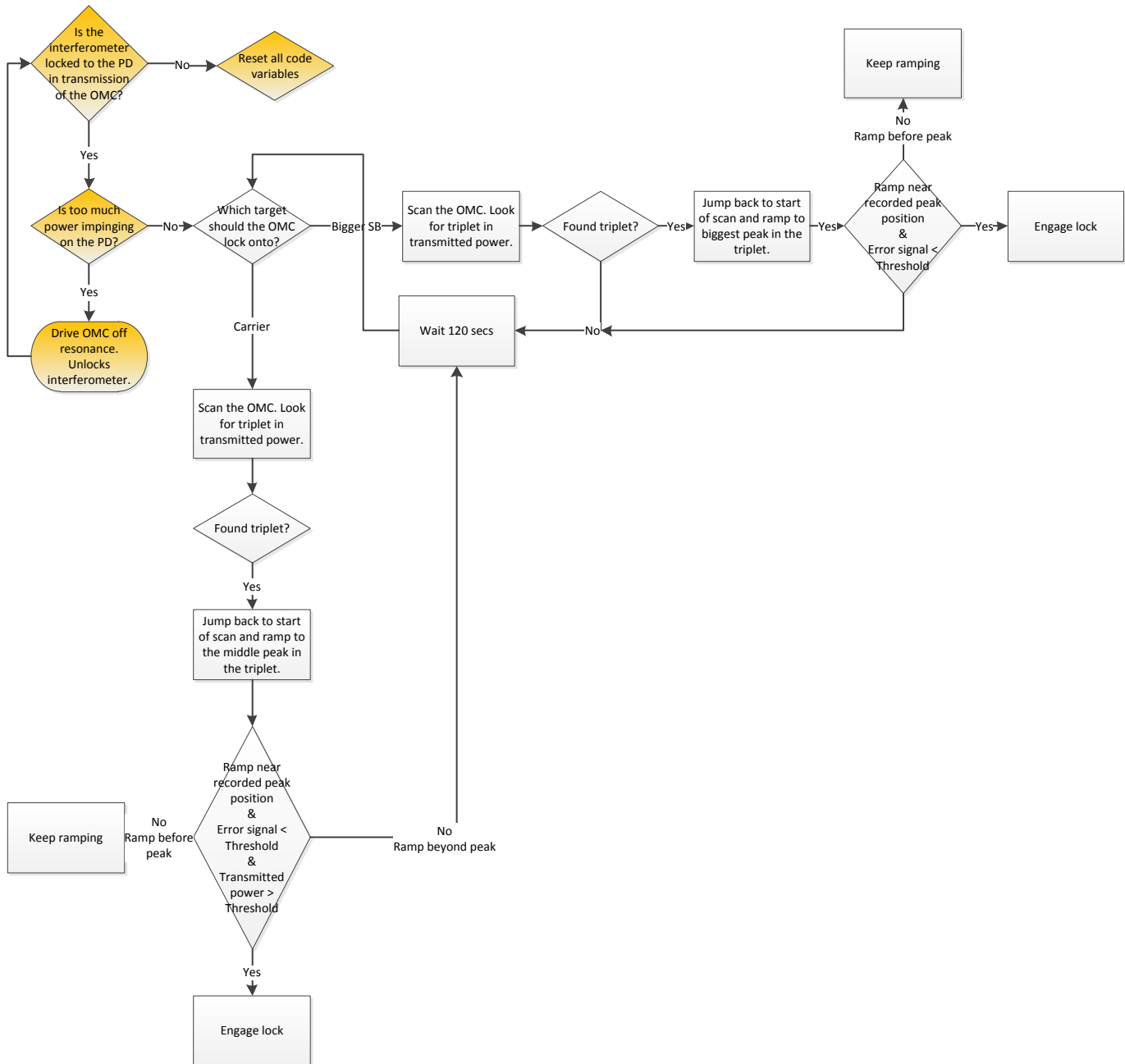


Figure D.1: Simplified flow chart of the OMC lock acquisition algorithm. Mind that the whole code is executed at every cycle of the real-time CDS system (i.e. at 32768 Hz). The conditions marked in yellow are evaluated every iteration of the code, independent of the program state. The state of the program is kept in static variables that are transferred from one code iteration to the next.

```

1 // LockAcqGEO.c -- 10-07-07 by M. Prijatelj
  // Last updated 12-06-13 by M. Prijatelj
3 // Lock acquisition for the OMC in GEO

5 void LockAcqGEO(double *in, int inSize, double *out, int outSize) {
  double GEOstatus; //Status of GEO's main interferometer
7 double power; //Power in transmission of the OMC
  double LPpower; //Lowpassed power, used to decide if OMC is in
    ill state
9 double locktarget; //What do you want to lock onto? 0:Carrier,
    1:Bigger SB, 2:Smaller SB
  static double offset; //Voltage ramp applied to the PZT
11 double limithigh; //Upper limit allowed for offset
  double limitlow; //Lower limit allowed for offset
13 static double pwrSB1; //Power of bigger sideband
  static double pwrSB2; //Power of smaller sideband
15 static double posSB1; //Position of bigger sideband
  static double posSB2; //Position of smaller sideband
17 static double step; //Step of the Lockacq process
  static double run; //Fine tracker of program execution
19 static double timer; //Parameter used to wait a certain time. Used
    to allow the PZT time to respond
  static int reset; //If locking target found in 120secs this
    becomes == 1 and resets the code
21 static double carrierpwr;
  static double carrierpos;
23
  //Parameters used to identify and remember the positions of the
    carrier and SBs
25 static double tpos1;
  static double tpos2;
27 static double tpos3;
  static double pos1;
29 static double pos2;
  static double pos3;
31 static double thresh;
  static double nomaxyet;
33 static double tpwr2;
  static double tpwr3;
35 double Errsignal; //Error signal

37 //Parameters used to drive the OMC off resonance when the main
    interferometer loses lock
  static double rescuepd;
39 static double rescuedirection; //Remember which direction to go,
    up or down
  static double rescpd; // Just for testing purposes

```

```

41 double maxpower;           //Maximum power allowed to pass through
    the OMC
42 double lockpower;         //Minimum power to consider the OMC to be
    in lock
43 double PZTcontrol;         //PD-rescue:Use this to switch off the
    PZT length control feedback
44 double PZTfeedback;       //PR-rescue:Remember the last PZT length
    control feedback before switching it off in the PD-rescue
    procedure
45
    limithigh=12000;           //Limits to the PZT ramp, was 30k for > 1
    FSR
47 limitlow=-12000;          //Limits to the PZT ramp, was 30k for > 1
    FSR
    maxpower=15000;           //Maximum allowed power before a lock-
    loss of the interferometer is recognized
49 lockpower=300;
    thresh=1600;
51
53 //Read the input variables
    power=in[0];
55 GEOstatus=in[1];
    locktarget=in[2];
57 Errsignal=in[3];
    LPpower=in[4];
59 rescpd=in[5];
    PZTfeedback=in[6];
61
    power=abs(power);
63 LPpower=abs(LPpower);
    PZTcontrol=1;
65
    // Reset everything in this file if GEO or OMC fall out of lock
67 if(GEOstatus == 0 || reset == 1)
    {
69     rescuedirection=0;
        rescuepd=0;
71     carrierpwr=0;
        carrierpos=0;
73     timer=0;
        pwrSB1=0;
75     pwrSB2=0;
        posSB1=0;
77     posSB2=0;
        offset=0;
79     step=0;

```

```

      run=0;
81   tpos1=-50000;
      tpos2=-50000;
83   tpos3=-50000;
      pos1=-50000;
85   pos2=-50000;
      pos3=-50000;
87   tpwr2=0;
      tpwr3=0;
89   nomaxyet=1;
      reset=0;
91 }

93
if(rescuepd >= 1 && timer < 30001) goto rescuephoto;
95
if(GEOstatus == 2 && step < 11)           //Lock on carrier
97   {
      if(run==0)
99     {
          offset = (limitlow - 3000);
101    carrierpwr=0;
          run=1;
103    timer=0;
      goto finish;
105    }

107    if(run == 1)
      {
109      offset=offset+0.015;
      if(LPpower > thresh && nomaxyet == 1) //Always find the
          first maximum
111    {
          tpos3=offset;
113      nomaxyet=0;
      }
115    if(LPpower > thresh && nomaxyet == 0 && offset-tpos3 > 250) //
        Find the second max separate from the first
      {
117      tpos1=tpos2;
          tpos2=tpos3;
119      tpos3=offset;
      }
121    if((tpos2 - tpos1) < 900 && (tpos2 - tpos1) > 400 && (tpos3 -
        tpos2) < 900 && (tpos3 - tpos2) > 400)
      {
123      pos3=tpos3;

```

```

    pos2=tpos2;
125    pos1=tpos1;
    carrierpos=pos2;
127    run=1.1;
}
    if(timer > 60*65536) reset=1; //If it didn't find
    something to lock on retry to lock again.
}
131    if(run == 1.1)
    {
133    timer=0;
    offset= (limitlow-3000);
135    run=1.2;
    goto finish;
137    }
//Lock either on the carrier of one of the SBs
139    if(run == 1.2 && locktarget == 0)
    {
141    offset=offset+0.015;
    if((offset > carrierpos+20) && abs(carrierpos-offset) < 200
    && Errsignal < 12 ) run=2;
143    if(timer > 60*65536) reset=1; //If it didn't find something
    to lock on retry to lock again.
    }
145    if(run == 1.2 && locktarget == 2)
    {
147    offset=offset+0.015;
    if((offset > pos1+20) && abs(pos1-offset) < 200 && Errsignal
    < 12 ) run=2;
149    if(timer > 60*65536) reset=1; //If it didn't find something
    to lock on retry to lock again.
    }
151    if(run == 1.2 && locktarget == 1)
    {
153    offset=offset+0.015;
    if((offset > pos3+20) && abs(pos3-offset) < 200 && Errsignal
    < 12 ) run=2;
155    if(timer > 60*65536) reset=1; //If it didn't find something
    to lock on retry to lock again.
    }
157    }

159 if( timer > 120*65536 && GEOstatus < 3 ) reset=1;
    if( run == 2)
161 {
    run=4;
163    step=10;

```

```

}
165 finish: if(GEOstatus == 4) PZTcontrol=1;
167 rescuephoto: if((rescpd > maxpower && offset <= 0 && rescuepd == 0
    ) || (rescuepd >= 1 && rescuedirection == 1) ) //Move the OMC
    off of carrier transmission to a dark position. Account for 2Hz
    Hardware-LP.
169     {
        PZTcontrol=0;           //Switch off the PZT control
171     rescuedirection=1;
        if(rescuepd == 0)
173     {
        offset=offset+PZTfeedback; //Transfer the dynamic PZT feedback
            to a static offset
175     timer=0;
        step=11;
177     run=1;
        offset=offset+31164; //Apply a huge offset for max. speed
179     rescuepd=1; //Rescueing the PD is now the only thing for
            the next 3000 cycles
        }
181     if( timer >= 1000 && rescuepd == 1)
        {
183     offset=offset-29938; //Apply the right offset for a dark pos.
            when the PZT actually arrives there
        rescuepd=2;
185     }
    }
187
    if((rescpd > maxpower && offset > 0 && rescuepd == 0 ) || (
        rescuepd >= 1 && rescuedirection == 2) ) //The same as at
        rescuephoto tag. Execute either one depending on offset
        value.
189     {
        PZTcontrol=0;           //Switch off the PZT control
191     rescuedirection=2;
        if(rescuepd == 0)
193     {
        offset=offset+PZTfeedback; //Transfer the dynamic PZT feedback
            to a static offset
195     timer=0;
        step=11;
197     run=1;
        offset=offset-23940; //Apply a huge offset for max. speed
199     rescuepd=1; //Rescueing the PD is now the only thing
            for the next 3000 cycles
    }

```

```
    }
201   if( timer >= 1000 && rescuepd == 1)
    {
203   offset=offset+22230;    //Apply the right offset for a dark pos
    . when the PZT actually arrives there
    rescuepd=2;
205   }
    }
207

209 if( PZTcontrol == 1)
    {
211   PZTfeedback=0;
    }
213
    if( timer < 300*65536) timer++;
215
    out[0]=offset;
217 out[1]=step;
    out[2]=run;
219 out[3]=PZTcontrol;
    };
```


E The LabView component of the output mode cleaner's control system

The LV component of the OMC control system is responsible for high-level non-real-time duties and provides a GUI for the OMC. Most pre-existing GEO 600 control systems are analog electronics, supervised by LV 6.1. A LV 2009 PC interfaces the OMC's control system with these pre-existing LV 6.1 systems. LV 2009 communicates with CDS via the channel access protocol component of the EPICS over Ethernet, and with LV 6.1 via a direct UDP link at 10 Hz also over Ethernet. LV also checks the state of the CDS filters and automatically switches them to the appropriate states. The type of alignment control for the OMC is selectable here. An override switch is provided to allow for user interaction without interference by the automation. For convenience, this LV program was also used for communication between the source of squeezed vacuum and the pre-existing LV 6.1 systems.

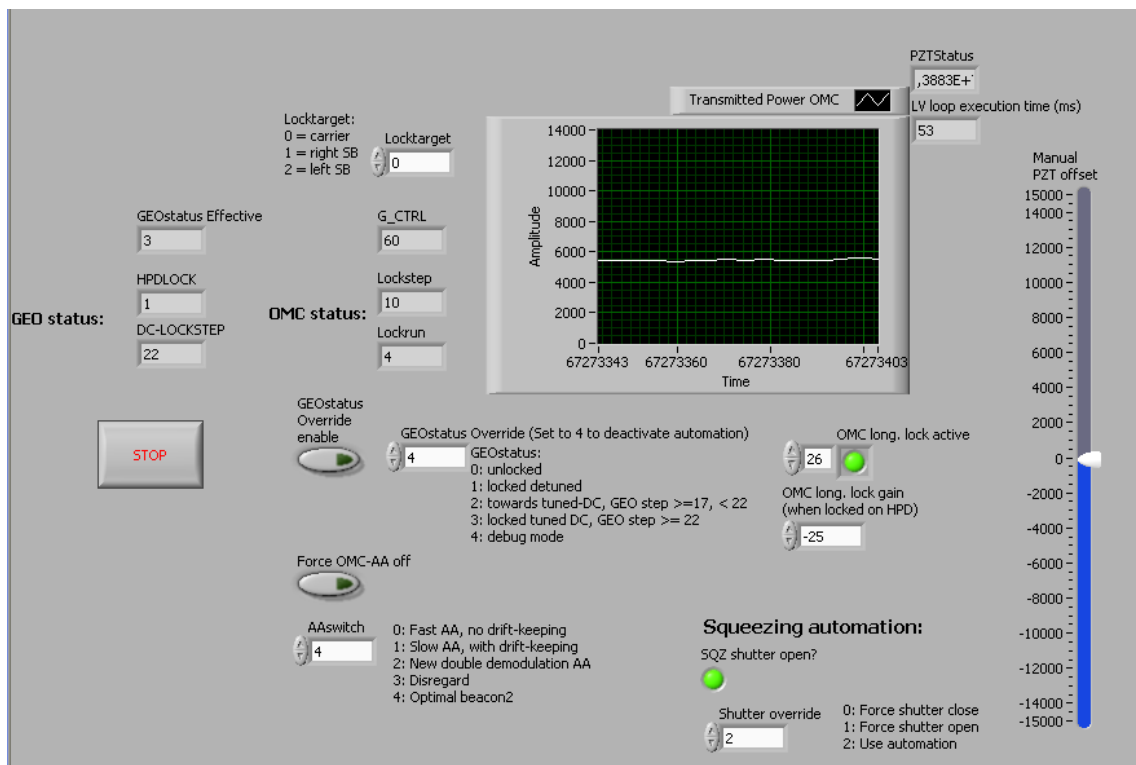


Figure E.1: LabView GUI of the OMC control.

Acknowledgments

I would like to thank Karsten Danzmann for the opportunity to work at the Albert-Einstein-Institute and GEO 600 which is an amazing place to do science.

I owe all my colleagues at GEO 600 my gratitude for the scientific input they provided and the great work atmosphere.

I am deeply indebted to my supervisor Hartmut Grote for his constant support and his inexhaustible patience.

Special thanks to Gerrit Kühn for his constant help wrestling with the CDS.

I am very happy to have worked with Jonathan Leong and thank him for all his support and his infectious enthusiasm.

I would like to thank Jérôme Degallaix helping me get up to speed at the beginning of this thesis and for his invaluable help beyond all expectations.

I had the joy of sharing an office with Christoph Affeldt and would like to thank him for the nice atmosphere and many fruitful discussions.

I would like to thank Christoph Affeldt, Kate Dooley, Hartmut Grote, Jonathan Leong, Harald Lück, and Holger Wittel for proofreading this thesis. Any remaining errors remain entirely under my responsibility.

I would like to thank Rana Adhikari for the opportunity to collect experience at the Caltech 40 meter interferometer and Stefan Goßler for initiating this visit.

Allow me to switch to german for the final acknowledgement: Ich danke meiner Mutter Charlotta Prijatelj für ihren Glauben an mich und für ihre konstante Unterstützung.

Bibliography

- [AAA⁺08] F Acernese, P Amico, M A Alshourbagy, et al.
The Virgo 3 km interferometer for gravitational wave detection.
J. Opt. A: Pure Appl. Opt., 10:064009, 2008.
- [AAA⁺11a] T Accadia, F Acernese, F Antonucci, et al.
Status of the Virgo project.
Class. Quantum Grav., 28:114002, 2011.
- [AAA⁺11b] F Antonucci, M Armano, H Audley, et al.
LISA Pathfinder: mission and status.
Class. Quantum Grav., 28:094001, 2011.
- [ABB⁺08] P Astone, R Ballantini, D Babusci, et al.
EXPLORER and NAUTILUS gravitational wave detectors: a status report.
Class. Quantum Grav., 25:114048, 2008.
- [AG⁺10] R S Amin, J A Giaime, et al.
Gravitational-wave detector-derived error signals for the LIGO thermal compensation system.
Class. Quantum Grav., 27:215002, 2010.
- [Agu11] O D Aguiar.
Gravitational wave detection: What is new?
RevMexAA: Serie de Conferencias, 40:299–304, 2011.
- [AIY⁺10] M Ando, K Ishidoshiro, K Yamamoto, et al.
Torsion-bar antenna for low-frequency gravitational-wave-observations.
Phys. Rev. Lett., 105:161101, 2010.
- [AKS⁺09] M Ando, S Kawamura, S Sato, et al.
DECIGO pathfinder.
Class. Quantum Grav., 26:094019, 2009.
- [AM07] K L Aplin and K F Middleton.
A Michelson interferometer system for testing the stability of a piezo-electric actuator intended for use in space.
J. Phys.: Conf. Ser., 85:012013, 2007.
- [And84] D Z Anderson.
Alignment of resonant optical cavities.
Appl. Opt., 23:2944–2949, 1984.

- [ANS12] ANSYS, Inc.
www.ansys.com, June 2012.
- [Arm06] J W Armstron.
Low-frequency gravitational wave searches using spacecraft doppler tracking.
Living Rev. Relativity, 9:1, 2006.
- [ASM⁺12] Y Aso, K Somiya, O Miyakawa, et al.
Length sensing and control strategies for the LCGT interferometer.
<http://arxiv.org/pdf/1111.7147v2.pdf>, January 2012.
- [ATT⁺09] K Arai, R Takahashi, D Tatsumi, et al.
Status of japanese gravitational wave detectors.
Class. Quantum Grav., 26:204020, 2009.
- [BBB⁺01] G Ballardin, L Bracci, S Braccini, et al.
Measurement of the VIRGO superattenuator performance for seismic noise suppression.
Rev. Sci. Instrum., 72:3643, 2001.
- [BBB⁺12] B Barr, A Bell, C Bell, et al.
LIGO 3 strawman design, team red.
<https://dcc.ligo.org/cgi-bin/DocDB/ShowDocument?docid=86550>, January 2012.
LIGO technical note T1200046.
- [BBC⁺05] M Bignotto, M Bonaldi, M Cerdonio, et al.
New suspension system for the gravitational wave bar detector AURIGA.
Rev. Sci. Inst., 76:084502, 2005.
- [BCC⁺97] A Bergamin, G Cavagnero, L Cordiali, et al.
Scanning X-ray interferometry over a millimeter baseline.
IEEE T. Instrum. Meas., 46:576–579, 1997.
- [BCD⁺11] M G Beker, G Cella, R DeSalvo, et al.
Improving the sensitivity of future GW observatories in the 1-10Hz band: Newtonian and seismic noise.
Gen. Relativ. Gravit., 43:623–656, 2011.
- [BD30] R M Bozorth and J F Dillinger.
Barkhausen effect II. Determination of the average size of the discontinuities in magnetization.
Phys. Rev., 35:733–752, 1930.
- [BH84] F Bayer-Helms.
Coupling coefficients of an incident wave and the modes of a spherical

- optical resonator in the case of mismatching and misalignment.
Appl. Opt., 23:1369–1379, 1984.
- [BHJZ12] D G Blair, E J Howell, L Ju, and C Zhao, editors.
Advanced gravitational wave detectors.
Cambridge University Press, 2012.
ISBN 978-0-521-87429-8.
- [BM02] N T Bishop and S D Maharaj, editors.
*Proceedings of the 16th International Conference on General Relativity
& Gravitation*.
World Scientific Publishing Co Pte. Ltd., 2002.
- [Boa11] LISA Review Board.
LISA mission technical & programmatic review report.
[http://sci.esa.int/science-e/www/object/index.cfm?
fobjectid=48370](http://sci.esa.int/science-e/www/object/index.cfm?fobjectid=48370), January 2011.
- [Bor10] R Bork.
AdvLigo CDS design overview.
[https://dcc.ligo.org/cgi-bin/DocDB/ShowDocument?.submit=
Number&docid=T0900612&version=](https://dcc.ligo.org/cgi-bin/DocDB/ShowDocument?.submit=Number&docid=T0900612&version=), 2010.
LIGO technical note T0900612.
- [CBB⁺12] A V Cumming, A S Bell, L Barsotti, et al.
Design and development of the Advanced LIGO monolithic fused silica
suspension.
Class. Quantum Grav., 29:035003, 2012.
- [Che07] S Chelkowski.
Squeezed light and laser interferometric gravitational wave detectors.
PhD thesis, Leibniz Universität Hannover, 2007.
- [CM10] I Ciufolini and R A Matzner, editors.
General relativity and John Archibald Wheeler.
Springer Science+Business Media B.V., 2010.
- [Cor a] EG&G Instruments Corporation.
Model 5302 lock-in amplifier instruction manual.
<http://www.signalrecovery.com/literature/manuals.aspx>, .
- [Cor b] General Standards Corporation.
PMC66-16AI64SSA/C.
[http://www.generalstandards.com/specs/pmc66_16ai64ssa_c_
spec_092307.pdf](http://www.generalstandards.com/specs/pmc66_16ai64ssa_c_spec_092307.pdf), .
- [Dan05] K Danzmann.
Proposal for upgrading the gravitational wave detector GEO 600.
June 2005.

- [Deg10] J Degallaix.
OSCAR a Matlab based optical FFT code.
J. Phys.: Conf. Ser., 228:012021, 2010.
- [Deg12] J Degallaix.
OSCAR.
<http://www.mathworks.com/matlabcentral/fileexchange/20607>,
July 2012.
- [DGP⁺10] J Degallaix, H Grote, M Prijatelj, et al.
Commissioning of the tuned DC readout at GEO 600.
J. Phys.: Conf. Ser., 228:012013, 2010.
- [DMF⁺12] K L Dooley, A A Muzammil, D Feldbaum, et al.
Thermal effects in the Input Optics of the Enhanced Laser Interferometer
Gravitational-wave Observatory interferometers.
Rev. Sci. Inst., 83:033109, 2012.
- [dWGvH⁺03] A de Waard, L Gottardi, J van Houwelingen, et al.
MiniGRAIL, the first spherical detector.
Class. Quantum Grav., 20:143–151, 2003.
- [Ein05] A Einstein.
Zur Elektrodynamik bewegter Körper.
Ann. Phys., 322:891–921, 1905.
- [Ein16] A Einstein.
Die Grundlagen der allgemeinen Relativitätstheorie.
Ann. Phys., 49:769–822, 1916.
- [Ein18] A Einstein.
Über Gravitationswellen.
Sitzungsberichte der Königlich Preussischen Akademie der Wissenschaften, VIII:154–167, 1918.
- [eLI12] Gravitational Wave Astronomy in Space eLISA/NGO.
<http://elisa-ngo.org/>, June 2012.
- [ESB⁺10] T Eberle, S Steinlechner, J Bauchrowitz, et al.
Quantum enhancement of the zero-area sagnac interferometer topology
for gravitational wave detection.
Phys. Rev. Lett., 104:251102, 2010.
- [Faf10] V Fafone.
Advanced Virgo thermal compensation system.
<https://tds.ego-gw.it/q1/?c=7219>, February 2010.
VIRGO document VIR-0095A-10.

- [FHL⁺04] A Freise, G Heinzl, H Lück, et al.
Frequency-domain interferometer simulation with higher-order spatial modes.
Class. Quantum Grav., 21:1067–1074, 2004.
- [FR10] V Fafone and A Rocchi.
TCS noise: general concepts and applications to the Virgo / Virgo+ case.
<https://tds.ego-gw.it/itf/tds/index.php?callContent=2&callCode=7539&title=TCS%20noise&author=fafone&startPage=>,
April 2010.
VIRGO document VIR-0615B-09.
- [Fre] A Freise.
<http://www.rzg.mpg.de/adf/>, .
- [FS10] A Freise and K A Strain.
Interferometer techniques for gravitation-wave detection.
Living Rev. Relativity, 13:1–81, 2010.
- [FSLA⁺12] T Fricke, N Smith-Lefebvre, R Abbott, et al.
DC readout experiment in Enhanced LIGO.
Class. Quantum Grav., 29:065005, 2012.
- [G⁺10] H Grote et al.
The GEO 600 status.
Class. Quantum Grav., 27:084003, 2010.
- [GCG⁺04] N Gehrels, G Chincarini, P Giommi, et al.
The SWIFT gamma-ray burst mission.
The Astrophys. J., 611:1005–1020, 2004.
- [GMB⁺99] M B Gray, D E McClelland, M Barton, et al.
A simple high-sensitivity interferometric position sensor for test mass control on an advanced LIGO interferometer.
Opt. Quant. Electron., 31:571–582, 1999.
- [Goß04] S Goßler.
The suspension systems of the interferometric gravitational-wave detector GEO 600.
PhD thesis, Universität Hannover, 2004.
- [GR83] P F Gascoyne and H N Rutt.
An opto-acoustic frequency lock system for pulsed lasers.
J. Phys. E: Sci. Instrum., 16:31, 1983.
- [Gra12] Gravitational Wave International Committee.
Roadmap: The future of gravitational wave astronomy.
<https://gwic.ligo.org/roadmap/>, 2012.

- [Gro03] H Grote.
Making it work: Second generation interferometry in GEO 600!
PhD thesis, Universität Hannover, 2003.
- [H⁺10] G M Harry et al.
Advanced LIGO: the next generation of gravitational wave detectors.
Class. Quantum Grav., 27:084006, 2010.
- [HAA⁺10] G Hobbs, A Archibald, Z Arzoumanian, et al.
The International Pulsar Timing Array project: using pulsars as a
gravitational wave detector.
Class. Quantum Grav., 27:084013, 2010.
- [HDP66] W R Hook, R H Dishington, and Hilberg R P.
Laser cavity dumping using time variable reflection.
Appl. Phys. Lett., 9:125, 1966.
- [Hee06] J Heefner.
Preliminary noise measurements of the General Standards PCI66-
16AI64SSa-64-50M ADCs.
[https://dcc.ligo.org/cgi-bin/DocDB/ShowDocument?.submit=
Number&docid=T060158&version=](https://dcc.ligo.org/cgi-bin/DocDB/ShowDocument?.submit=Number&docid=T060158&version=), June 2006.
LIGO technical note T060158.
- [Hee07] J Heefner.
AdL AA/AI filter (65536 sample rate) board test plan, June 2007.
LIGO technical note T0700146.
- [HGD⁺09] S Hild, H Grote, J Degallaix, et al.
DC-readout of a signal-recycled gravitational wave detector.
Class. Quantum Grav., 26:055012, 2009.
- [HJD⁺11] J M Hogan, D M S Johnson, S Dickerson, et al.
An atomic gravitational wave interferometric sensor in low earth orbit
(AGIS-LEO).
Gen. Relativ. Gravit., 43:1953–2009, 2011.
- [HSM⁺98] G Heinzl, K A Strain, J Mizuno, et al.
Experimental Demonstration of a Suspended Dual Recycling Interfer-
ometer for Gravitational Wave Detection.
Phys. Rev. Lett., 81:5493–5496, 1998.
- [HT75] R A Hulse and J H Taylor.
Discovery of a pulsar in a binary system.
Astrophys. Journal, 195:51–53, 1975.
- [HW12] S Hild and H Wittel.
Personal communications.
2012.

- [IAT⁺11] K Ishidoshiro, M Ando, A Takamori, et al.
Upper limit on gravitational wave backgrounds at 0.2 Hz with a torsion-bar antenna.
Phys. Rev. Lett., 106:161101, 2011.
- [JBC⁺11] O Jennrich, P Binetruy, M Colpi, et al.
NGO Revealing a hidden universe: opening a new chapter of discovery, assessment study report.
http://sci2.esa.int/cosmic-vision/NGO_YB.pdf, December 2011.
- [K⁺10] K Kuroda et al.
Status of LCGT.
Class. Quantum Grav., 27:084004, 2010.
- [KAB⁺02] K Kötter, C Aulbert, S Babak, et al.
Data acquisition and detector characterization of GEO 600.
Class. Quantum Grav., 19:1399–1407, 2002.
- [KAS⁺11] S Kawamura, M Ando, N Seto, et al.
The japanese space gravitational wave antenna: DECIGO.
Class. Quantum Grav., 28:094011, 2011.
- [Kha10] F Ya Khalili.
Optimal configurations of filter cavity in future gravitational-wave detectors.
Phys. Rev. D, 81:122002, 2010.
- [Kha11] A Khalaidovski.
Beyond the quantum limit - A squeezed-light laser in GEO.
PhD thesis, Gottfried Wilhelm Leibniz Universität Hannover, 2011.
- [KL66] H Kogelnik and T Li.
Laser beams and resonators.
Appl. Opt., 5:1550–1567, 1966.
- [KSW⁺07] P Kwee, F Seifert, B Wilke, et al.
Laser beam quality and pointing measurements with an optical resonator.
Rev. Sci. Inst., 78:073103, 2007.
- [L⁺10] M Lorenzini et al.
The monolithic suspension for the Virgo interferometer.
Class., 27:084021, 2010.
- [LAD⁺10] H Lück, C Affeldt, J Degallaix, et al.
The upgrade of GEO 600.
J. Phys.: Conf. Ser., 228:012012, 2010.

- [Lüc09] H Lück.
The Transition to GEO-HF.
<https://dcc.ligo.org/cgi-bin/DocDB/ShowDocument?.submit=Number&docid=G0900523&version=>, June 2009.
LIGO document G0900523.
- [LZY⁺10] J Luo, Z Zhou, H Yeh, et al., editors.
Gravitation and astrophysics.
World Scientific Publishing Co Pte. Ltd., 2010.
ISBN 978-981-4307-66-6.
- [Mag00] M Maggiore.
Gravitational Wave experiments and early universe cosmology.
Phys. Reports, 331:283–367, 2000.
- [Min10] H Minkowski.
Die Grundgleichungen für die elektromechanischen Vorgänge in bewegten Körpern.
Mathematische Annalen, 68:472–525, 1910.
- [MJH⁺05] M P McHugh, W W Johnson, W O Hamilton, et al.
Calibration of the ALLEGRO resonant detector.
Class. Quantum Grav., 22:965–973, 2005.
- [MLB⁺09] C Meegan, G Lichti, P N Bhat, et al.
The FERMI gamma-ray burst monitor.
The Astrophys. J., 702:791–804, 2009.
- [MMC⁺11] D E McClelland, N Mavalvala, Y Chen, et al.
Advanced interferometry, quantum optics and optomechanics in gravitational wave detectors.
Laser Photonics Rev., 5:677–696, 2011.
- [MMR⁺94] E Morrison, B J Meers, D I Robertson, et al.
Automatic alignment of optical interferometers.
Appl. Opt., 33:5041–5049, 1994.
- [MSN⁺93] J Mizuno, K A Strain, P G Nelson, et al.
Resonant sideband extraction: a new configuration for interferometric gravitational wave detectors.
Phys. Lett. A, 175:273–276, 1993.
- [Nyq28] H Nyquist.
Certain topics in telegraph transmission theory.
Transactions of the American Inst. of Electrical Engineers, 47:617–644, 1928.

- [OC00] A T O’Neil and J Courtial.
Mode transformations in terms of the constituent Hermite-Gaussian or Laguerre-Gaussian modes and the variable-phase mode converter.
Opt. Commun., 181:35–45, 2000.
- [Oka] K Okada.
Magnetic coupling noise in a torsion-bar antenna for gravitational-wave observation.
<http://www.gravity.phys.uwm.edu/conferences/gwpaw/talks/okada.pdf>, .
- [Oug82] K E Oughstun.
On the completeness of the stationary transverse modes in an optical cavity.
Opt. Commun., 42:72, 1982.
- [PAA+10] M Punturo, M Abernathy, F Acernese, et al.
The Einstein Telescope: a third-generation gravitational wave observatory.
Class. Quantum Grav., 27:194002, 2010.
- [PBG+05] D M Palmer, S Barthelmy, N Gehrels, et al.
A giant γ -ray flare from the magnetar SGR 1806-20.
Nature, 434:1107–1109, 2005.
- [PCC+10] J Predoi, J Clark, T Creighton, et al.
Prospects for joint radio telescope and gravitational-wave searches for astrophysical transients.
Class. Quantum Grav., 27:084018, 2010.
- [PDG+12] M Prijatelj, J Degallaix, H Grote, et al.
The output mode cleaner of GEO 600.
Class. Quantum Grav., 29:055009, 2012.
- [PGD+10] M Prijatelj, H Grote, J Degallaix, et al.
Control and automatic alignment of the output mode cleaner of GEO 600.
J. Phys.: Conf. Ser., 228:012014, 2010.
- [Pis09] M Pisani.
A homodyne Michelson interferometer with sub-picometer resolution.
Meas. Sci. Technol., 20:084008, 2009.
- [R+12] G Racca et al.
NGO - New gravitational wave observer technical & programmatic review report.
http://sci2.esa.int/cosmic-vision/NGO_technical_and_programmatic_review_report.pdf, February 2012.

- [RCG⁺10] D S Rabeling, J H Chow, M B Gray, et al.
Experimental demonstration of impedance match locking and control for coupled resonators.
Opt. Express, 18:9314–9323, 2010.
- [RM10] G D Racca and P W McNamara.
The LISA Pathfinder mission.
Space Sci. Rev., 151:159–181, 2010.
- [S⁺09] J R Smith et al.
The path to the Enhanced and Advanced LIGO gravitational-wave detectors.
Class. Quantum Grav., 26:114013, 2009.
- [Sau94] Peter R. Saulson.
Interferometric gravitational wave detectors.
World Scientific Publishing Co Pte. Ltd., 1994.
- [Saw12] A Sawadsky.
Das Michelson-Sagnac-Interferometer mit SiN-Membran und Signal-Recycling.
Master’s thesis, Gottfried Wilhelm Leibniz Universität Hannover, 2012.
- [Sch09] B Schutz.
A first course in general relativity.
Cambridge University Press, 2009.
- [Sha11] P Shawhan.
(Some additional) multi-messenger astronomy opportunities for LIGO and VIRGO.
<https://dcc.ligo.org/cgi-bin/DocDB/ShowDocument?.submit=Number&docid=G080438&version=>, February 2011.
LIGO document G080438.
- [Sie86] Anthony E. Siegmann.
Lasers.
University Science Books, 1986.
- [Sie90] A. E Siegmann.
New developements in laser resonators.
Proc. SPIE 1224, 2, 1990.
- [SKM⁺09] S Sato, S Kawamura, A Masaki, et al.
DECIGO: The japanese space gravitational wave antenna.
J. Phys.: Conf. Ser., 154:012040, 2009.
- [SLBE⁺11] N Smith-Lefebvre, S Ballmer, M Evans, et al.
Optimal alignment sensing of a readout mode cleaner cavity.
Optics Letters, 36:4365–4367, 2011.

- [SM91] K A Strain and B J Meers.
Experimental Demonstration of Dual Recycling for Interferometric Gravitational-Wave Detectors.
Phys. Rev. Lett., 66:1391–1394, 1991.
- [Smi06] J R Smith.
Formulation of Instrument Noise Analysis Techniques and Their Use in the Commissioning of the Gravitational Wave Observatory, GEO 600.
PhD thesis, Gottfried Wilhelm Leibniz Universität Hannover, 2006.
- [The09] The VIRGO Collaboration.
Advanced Virgo baseline design.
<https://tds.ego-gw.it/itf/tds/index.php?callContent=2&callCode=6616&title=Advanced%20Virgo%20baseline%20design&startPage=>, 2009.
VIRGO document VIR-0027A-09.
- [The11] The LIGO Scientific Collaboration.
A gravitational wave observatory operating beyond the quantum shot-noise limit.
Nature physics, 7:962–965, 2011.
- [TLSH⁺00] M E Tobar, C R Locke, I Siong Heng, et al.
Niobe: Improved noise temperature and back ground noise suppression.
AIP Conf. Proc., 523:283, 2000.
- [TT08] The AURIGA Collaboration and The LIGO Scientific Collaboration.
A joint search for gravitational wave bursts with AURIGA and LIGO.
Class. Quantum Grav., 25:095004, 2008.
- [V⁺11] C Vigorito et al.
SNEWS - The Supernova Early Warning System.
J. Phys.: Conf. Ser., 309:012026, 2011.
- [VT06] A Vinante and The AURIGA Collaboration.
Present performance and future upgrades of the AURIGA capacitive readout.
Class. Quantum Grav., 23:103–110, 2006.
- [WAA⁺02] B Willke, P Aufmuth, C Aulbert, et al.
The GEO 600 gravitational wave detector.
Class. Quantum Grav., 19:1377–1387, 2002.
- [WAA⁺06] B Wilke, P Ajith, B Allen, et al.
The GEO-HF project.
Class. Quantum Grav., 24:207–214, 2006.

- [Web60] J Weber.
Detection and generation of gravitational waves.
Phys. Rev., 117:306–313, 1960.
- [Web68] J Weber.
Gravitations-wave-detector events.
Phys. Rev. Lett., 20:1307–1308, 1968.
- [Wil10] P Willems.
Thermal compensation system TCS technical presentation.
<https://dcc.ligo.org/cgi-bin/DocDB/ShowDocument?docid=58845>, April 2010.
LIGO document G1100460.
- [Wit11] H Wittel.
Thermal compensation in GEO 600.
<https://tds.ego-gw.it/q1/?c=8536>, September 2011.
VIRGO document VIR-0481A-11.
- [Wit12] H Wittel.
Personal communications.
July 2012.
- [WSW⁺08] S Wagner, B Schulz, R Wachter, et al.
Enhanced LIGO laser system.
<https://dcc.ligo.org/cgi-bin/DocDB/ShowDocument?docid=37155>, April 2008.
LIGO document G080229.
- [WT05] J M Weisberg and J H Taylor.
Relativistic binary pulsar B1913+16: Thirty years of observations and analysis.
ASP Conf. Series, 328:25, 2005.
- [YMM⁺10] K N Yakaunin, P Marronetti, A Maezzacappa, et al.
Gravitational waves from core collapse supernovae.
Class. Quantum Grav., 27:194005, 2010.
- [ZBD⁺02] I Zawischa, M Brendel, K Danzmann, et al.
The GEO 600 laser system.
Class. Quantum Grav., 19:1775–1781, 2002.

Mirko Prijatelj

Curriculum vitae

Marienstraße 47
30171 Hannover, Germany
✉ mirko.prijatelj@aei.mpg.de

Personal details

Date of birth: 3rd of December 1980
Place of birth: Hannover, Germany
Marital status: Single

Education and research experience

- 03.2010–present Member of the LIGO Scientific Collaboration
- 03.2008–present Member of the International Max Planck Research School (IMPRS) on Gravitational Wave Astronomy
- 03.2008–present Doctoral studies at Albert-Einstein-Institute, Max-Planck-Institute for Gravitational Physics, Cluster of Excellence QUEST, and Gottfried Wilhelm Leibniz Universität, Hannover
- 09.2011–11.2011 Visiting Student Researcher, California Institute of Technology
- 02.2008 Diploma in Physics
- 11.2006–12.2007 Diploma thesis at the Institute for Quantum Optics, Gottfried Wilhelm Leibniz Universität Hannover
'XUV-Strahlungsquellen in Gasen: Der Inneschalen-Röntgenlaser in Natrium und die Erzeugung Hoher Harmonischer in Edelgasen'
(translates to 'XUV radiation sources in gases: The inner-shell X-ray laser in sodium and the generation of high harmonics in noble gases')
- 2002–2008 Physics studies, Gottfried Wilhelm Leibniz Universität Hannover
- 06.2001 Abitur (Graduation), Gymnasium Tellkampfschule, Hannover

Publications with immediate relation to this thesis

- 1 **M. Prijatelj**, J. Degallaix, H. Grote, J. Leong, C. Affeldt, S. Hild, H. Lück, J. Slutsky, H. Wittel, K. Strain and K. Danzmann
The output mode cleaner of GEO 600
Class. Quantum Grav., 29:055009, 2012
- 2 J. Abadie, . . . , L. R. Price, **M. Prijatelj**, M. Principe, . . . , J. Zweizig
A gravitational wave observatory operating beyond the quantum shot-noise limit
Nature Phys., 7:962-965, 2011
- 3 **M. Prijatelj**, H. Grote, J. Degallaix, M. Hewitson, S. Hild, C. Affeldt, A. Freise, J. Leong, H. Lück, K. A. Strain, H. Wittel, B. Wilke and K. Danzmann
Control and automatic alignment of the output mode cleaner of GEO 600
J. Phys.: Conf. Ser., 228:012014, 2010
- 4 J. Degallaix, H. Grote, **M. Prijatelj**, M. Hewitson, S. Hild, C. Affeldt, A. Freise, J. Leong, H. Lück, K. A. Strain, H. Wittel, B. Willke and K. Danzmann
Commissioning of the tuned DC readout at GEO 600
J. Phys.: Conf. Ser., 228:012013, 2010
- 5 S. Hild, H. Grote, S. Chelkowski, K. Danzmann, A. Freise, M. Hewitson, J. Hough, H. Lück, **M. Prijatelj**, K. A. Strain, J. R. Smith and B. Willke
DC-readout of a signal-recycled gravitational wave detector
Class. Quantum Grav., 26:055012, 2009

Further publications

- 1 J. Aasi, . . . , L. R. Price, **M. Prijatelj**, M. Principe, . . . , J. Zweizig
The characterization of Virgo data and its impact on gravitational-wave searches
Class. Quantum Grav., 29:155002, 2012
- 2 J. Abadie, . . . , L. R. Price, **M. Prijatelj**, M. Principe, . . . , J. Zweizig
Search for gravitational waves associated with gamma-ray bursts during LIGO science run 6 and Virgo science runs 2 and 3
arXiv,1205.2216, 2012
- 3 J. Abadie, . . . , L. R. Price, **M. Prijatelj**, M. Principe, . . . , J. Zweizig
A First Search for coincident Gravitational Waves and High Energy Neutrinos using LIGO, Virgo and ANTARES data from 2007
arXiv,1205.3018, 2012
- 4 M. Evans, . . . , L. R. Price, **M. Prijatelj**, M. Principe, . . . , J. Zweizig
Swift follow-up observations of candidate gravitational-wave transient events
arXiv,1205.1124, 2012
- 5 J. Abadie, . . . , L. R. Price, **M. Prijatelj**, M. Principe, . . . , J. Zweizig
Search for Gravitational Waves from Intermediate Mass Binary Black Holes
arXiv,1201.5999, 2012
- 6 J. Abadie, . . . , L. R. Price, **M. Prijatelj**, M. Principe, . . . , J. Zweizig
All-sky search for gravitational-wave bursts in the second joint LIGO-Virgo run
arXiv,1202.2788, 2012

- 7 J. Abadie, . . . , L. R. Price, **M. Prijatelj**, M. Principe, . . . , J. Zweizig
Search for gravitational waves from low mass compact binary coalescence in LIGO's sixth science run and Virgo's science runs 2 and 3
Phys. Rev. D,83:082002, 2012
- 8 J. Abadie, . . . , L. R. Price, **M. Prijatelj**, M. Principe, . . . , J. Zweizig
Implications For The Origin Of GRB 051103 From LIGO Observations
arXiv,1201.4413, 2012
- 9 J. Abadie, . . . , L. R. Price, **M. Prijatelj**, M. Principe, . . . , J. Zweizig
Upper limits on a stochastic gravitational-wave background using LIGO and Virgo interferometers at 600-1000 Hz
arXiv,1112.5004, 2012
- 10 J. R. Leong, M. Hewitson, H. Lück, H. Grote, S. Hild, C. Affeldt, J. Degallaix, A. Freise, **M. Prijatelj**, K. Strain, H. Wittel, B. Willke and K. Danzmann
A new method for the absolute amplitude calibration of GEO 600,
Class. Quantum Grav., 29:065001, 2012
- 11 J. Abadie, . . . , L. R. Price, **M. Prijatelj**, M. Principe, . . . , J. Zweizig
First Low-Latency LIGO+Virgo Search for Binary Inspirals and their Electromagnetic Counterparts
arXiv,1112.6005, 2012
- 12 J. Abadie, . . . , L. R. Price, **M. Prijatelj**, M. Principe, . . . , J. Zweizig
Implementation and testing of the first prompt search for gravitational wave transients with electromagnetic counterparts to gravitational wave transients
arXiv,1109.3498, 2012
- 13 J. Abadie, . . . , L. R. Price, **M. Prijatelj**, M. Principe, . . . , J. Zweizig
All-sky Search for Periodic Gravitational Waves in the Full S5 LIGO Data
Phys. Rev. D 85, 022001, 2012
- 14 J. Abadie, . . . , L. R. Price, **M. Prijatelj**, M. Principe, . . . , J. Zweizig
Directional limits on persistent gravitational waves using LIGO S5 science data
arXiv,1109.1809, 2011
- 15 J. Abadie, . . . , L. R. Price, **M. Prijatelj**, M. Principe, . . . , J. Zweizig
Beating the spin-down limit on gravitational wave emission from the Vela pulsar
The Astrophys. J.,737:93, 2011
- 16 J. Abadie, . . . , L. R. Price, **M. Prijatelj**, M. Principe, . . . , J. Zweizig
Search for gravitational wave bursts from six magnetars
The Astrophys. J.,734:L35, 2011
- 17 J. Abadie, . . . , L. R. Price, **M. Prijatelj**, M. Principe, . . . , J. Zweizig
Search for gravitational waves from binary black hole inspiral, merger, and ringdown
Phys. Rev. D,83:122005, 2011
- 18 J. Abadie, . . . , L. R. Price, **M. Prijatelj**, M. Principe, . . . , J. Zweizig
A search for gravitational waves associated with the August 2006 timing glitch of the Vela pulsar
arXiv,1011.1357, 2010

- 19 J. Abadie, . . . , L. R. Price, **M. Prijatelj**, M. Principe, . . . , J. Zweizig
Calibration of the LIGO gravitational wave detectors in the fifth science run
Nucl. Instrum. Meth. in Phys. Res. A, 624:223-240, 2010
- 20 J. Abadie, . . . , L. R. Price, **M. Prijatelj**, M. Principe, . . . , J. Zweizig
Search for gravitational waves from compact binary coalescence in LIGO and Virgo data from S5 and VSR1
Phys. Rev. D, 10:2001, 2010
- 21 J. Abadie, . . . , L. R. Price, **M. Prijatelj**, M. Principe, . . . , J. Zweizig
First search for gravitational waves from the youngest known neutron star
The Astrophys. J., 722:1504-1513, 2010
- 22 J. Abadie, . . . , L. R. Price, **M. Prijatelj**, M. Principe, . . . , J. Zweizig
Predictions for the rates of compact binary coalescences observable by ground-based gravitational-wave detectors
Class. Quantum Grav., 27:173001, 2010
- 23 J. Abadie, . . . , L. R. Price, **M. Prijatelj**, M. Principe, . . . , J. Zweizig
Sensitivity to Gravitational Waves from Compact Binary Coalescences Achieved during LIGO's Fifth and Virgo's First Science Run
arXiv,1003.2481, 2010